Spatial characterization of the BT-20 triple negative breast cancer spheroidal model

by

Keith Ntokozo Ncube

A dissertation submitted in fulfilment of the requirements for the degree

Magister Scientiae

in

Pharmacology

in the

Faculty of Health Sciences

at the

University of Pretoria

Supervisor: Dr. W Cordier[1]

Co-supervisors: Prof. V Steenkamp[1]

Prof. AD Cromarty[1]

Dr. I van den Bout[2]

[1]Department of Pharmacology, School of Medicine, Faculty of Health Sciences, University of Pretoria

[2]Department of Physiology, School of Medicine, Faculty of Health Sciences, University of Pretoria

2019

Declaration of originality

Department of Pharmacology

Faculty of Health Sciences

University of Pretoria

Full names of student: Keith Ntokozo Ncube

Student number: 13264606

Subject of work: Dissertation

Title: Spatial characterization of the BT-20 triple-negative breast cancer multicellular spheroidal model

Declaration

I understand what plagiarism is and am aware of the University's policy in this regard.

I declare that this dissertation is my own original work. Where other people's work has been used (either from a printed source, Internet or any other source), this has been properly acknowledged and referenced in accordance with departmental requirements.

I have not used work previously produced by another student or any other person to hand in as my own.

I have not allowed, and will not allow, anyone to copy my work with the intention of passing it off as his or her own work.

Signature of student 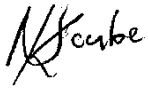

Date: 24/04/2019

Table of contents

Dedication

Dedicated to:

The late Senzeni Ncube (neé Ngwenya), a great mother and educator, may your soul forever rest in peace.

and

Vuyelwa Buque, we ran this race together, you unfortunately departed this world just as we were close to the finishing line, you'll be forever remembered, rest in peace friend.

Acknowledgements

Dear God: *It is not by my power, nor by my might, but only through your Spirit and might, that I have been graced with an opportunity to conduct and complete this project. Thank you for pulling me through.*

To my aunt: *Mrs. G Moyo*, m*y tertiary studies would not have been a possibility, had you not stepped in and played a role of a mother by taking me out of a hopeless 3-gap-year period after high school, and ensured that I obtain some University education. I appreciate you for all the support you have given to me from the start of my university studies up to this point. You are my hero.*

To my supervisor: *Dr. W Cordier*, *Thank you for the selfless mentorship and support. With your help, I have seen myself transition from a clueless undergraduate student into an emerging young researcher. All the advice and recommendations you have given to me have helped me reach places I could not (in my rational sense) dream of. Your consistent, non-judgmental, and positive compliments have always kept me going.*

To my co-supervisors: *Prof. V Steenkamp, thank you for rubbing your spirit of professionalism and academic etiquette off on me. Prof. AD Cromarty, I will carry the laboratory and science demeanour I have learnt from you to the next generation of scientists, your remarks consistently encourage me, thank you. Dr. I van Den Bout, the technical support and commitment you have provided to this project really go a long way, thank you.*

To my friends: *Andy, Bongi, Ewura, Jie, Shamiso, Wonder & Zelie, thank you for the social engagement and support. Shami, thank you for being the emotional punchbag during my mini breakdowns and all the spiritual upliftment. Andy, thank you for all your selfless advice and assistance in many aspects of the project, may God abundantly bless you in all your academic endeavours.*

To my family: *I appreciate you all for being my cheerleaders, the support you have given is honestly immeasurable.*

Technical assistance: *Dr. June Serem, thank you for accommodating us during the renovation of our lab, your kindness and warmth is much appreciated. Dr. Sandra Arbi, thank you for assistance with histology. Dr. Tracey Hurrell, your 'out of the box'*

interpretation of scientific data always helps me view my results from an informed perspective, thank you.

Funding

I would like to acknowledge the funding provided by the University of Pretoria's Research Development Programme grant (Department of Research and Innovation Support) of Dr. Werner Cordier, Masters research grant and the special internal research award. Funding from the National Research Foundation's innovation master's scholarship (grant number: 106572) is also much appreciated.

Ethics

The study was conducted in accordance with the set of ethical principles stipulated by the University of Pretoria's Health Sciences Research Ethics Committee.

The study used a commercially available BT-20 cell line, and no biological samples from human or animal subjects were harvested or used.

Ethical approval for conducting all experimentation in the project was granted by the University of Pretoria's Health Sciences Research Ethics Committee (reference number: 338/2017). The ethical approval certificate for the project is provided in Appendix I.

Study outputs

Conference presentations

Podium presentations

Ncube KN, Cromarty AD, van den Bout I, Cordier W. Comparative assessment of the *in vitro* efficacy of doxorubicin against BT-20 triple-negative breast carcinoma cells in a 2D and 3D cellular model. Health Sciences Faculty Day, University of Pretoria, South Africa, 23 August 2017.

Ncube KN, Steenkamp V, Cromarty AD, van den Bout I, Cordier W. Development and Characterisation of a triple-negative breast cancer multicellular spheroid model. Health Sciences Faculty Day, University of Pretoria, South Africa, 22 August 2018. **(3rd prize: oral presentation in the Basic Sciences category)**.

Ncube KN, Steenkamp V, Cromarty AD, van den Bout I, Cordier W. Development and Characterisation of a triple-negative breast cancer multicellular spheroid model. First Conference of Biomedical and Natural Sciences and Therapeutics, Stellenbosch, South Africa, 09 October 2018. **(2nd prize: South African Society for Basic and Clinical Pharmacology Young Scientist Oral Presentation Award in Basic Pharmacology)**.

Poster presentation

Ncube KN, Steenkamp V, Cromarty AD, van den Bout I, Cordier W. Development and Characterisation of a triple-negative breast cancer multicellular spheroidal model. 18th World Congress of Basic and Clinical Pharmacology, Kyoto, Japan, 04 July 2018.

Abstract

Breast cancer is a commonly diagnosed cancer in women, with increasing diagnosis and mortality rates. The triple-negative sub-type of the disease is characterised by lack of hormone-receptor overexpression, exhibition of poorly characterised molecular aberrations, and treatment failure. Chemotherapy is the current mainstay; however, it fails to slow tumor progression, and this is partially attributed to the lack of characterisation of biological features that drive treatment failure. There is, therefore, a need to characterise the biological features of triple-negative breast cancer, in order to develop effective therapies against the disease.

Researchers widely use monolayer cell culture in pre-clinical screening of anticancer drugs. However, the development of effective anti-cancer drugs is hampered by limitations inherent to these culture systems, as they insufficiently mimic the physiological characteristics of tumours *in vivo*. Spheroids have been suggested as a bridge to the gap between monolayers and animal models, as they combine the flexibility and cost-effectiveness of cell culture with the spatial and molecular attributes of tissue. This study aimed to grow and characterise a spheroid model of triple-negative breast cancer with regards to growth, morphology, and drug sensitivity.

The hanging drop and liquid overlay techniques were compared to select a method for growing spheroids. Spheroid growth was assessed using phase contrast microscopy and the bicinchoninic acid assay. Viability was assessed using the fluorescein diacetate (FDA)/propidium iodide (PI) assay. Haematoxylin and eosin staining were used for morphological evaluation. An iridium complex was used to investigate the induction of hypoxia. The sulphorodamine B and acid phosphatase assays, FDA/PI staining and phase contrast microscopy were used to assess the 72-h cytotoxicity effects of doxorubicin in monolayers and spheroids. Immunostaining and optical clearing were used to visualise the spatial distribution of the Ki-67 antigen and cadherins in spheroids.

Only cells cultured using the liquid overlay technique formed dense spheroids which were used for characterisation. Spheroid volume decreased from Day 4 (3.9×10^8 μm^3) to Day 10 (2.1×10^8 μm^3), while protein content increased slightly (7.0 to 8.5 µg/spheroid). The outer spheroid region had viable, well-nourished cells, while membrane-compromised cells were localized in the inner region. Spheroids developed hypoxic regions, which were not observed in monolayers. The IC_{25} (130 nM), IC_{50} (320 nM) and IC_{75} (1,580 nM) for doxorubicin exhibited a dose-dependent cytotoxicity of monolayer cell cultures with reduced acid phosphatase activity. These concentrations did not alter the spheroid size or acid phosphatase activity, and only concentrations as high as 6 µM were successful in altering spheroid integrity.

The attenuated response of doxorubicin in spheroids could be linked to the spatial heterogeneity of morphological and biochemical features of the spheroids. *In vivo* tumours are heterogeneous with respect to cellular morphology and chemical gradients. Spheroids, on the other hand, are considered as a robust platform for the *in vitro* recapitulation of the tumour microenvironment. Compared to monolayers, BT-20 spheroids could be adopted as a more relevant model for screening new drugs against triple-negative breast cancer. However, elucidation of mechanisms underlying chemoresistance, is required to further characterise the model.

List of abbreviations

γ-H2AX	H2A histone family member X
ADP	Adenosine diphosphate
ANOVA	Analysis of variance
APH	Acid phosphatase
ATM	Ataxia Telangiectasia Mutated
ATR	Ataxia Telangiectasia Mutated and Rad-3 related
BL	Basal-like
BRCA1	Breast cancer susceptibility gene 1
BRCA2	Breast cancer susceptibility gene 2
CAF	Cancer-associated fibroblasts
DAPI	4’,6-Diamidino-2-phenylindole
DDR	DNA-damage response
DMEM	Dulbecco’s modified essential medium
DNA	Deoxyribonucleic acid
DMSO	Dimethyl sulfoxide
DR5	Death receptor 5
ECM	Extracellular matrix
ER	Estrogen receptor
ERBB2	Erb-b2 receptor tyrosine kinase 2
F-12	Hams F-12 nutrient mixture
FBS	Foetal bovine serum
FDA	Fluorescein diacetate
G2	Gap 2

h	hour(s)
H_2O_2	Hydrogen peroxide
HCl	Hydrochloric acid
HER2	Human epidermal growth factor receptor 2
HIF	Hypoxia-inducible transcription factor
HIF 1α	Hypoxia-inducible factor 1 alpha
HRT	Hormone replacement therapy
IARC	International Agency for Research on Cancer
LMW	Low molecular weight
M	Mitosis
mAB	Monoclonal antibody
MALDI	Matrix-assisted laser desorption ionization
MCTS	Multicellular tumour spheroids
min	Minutes
MSI	Mass spectrometric imaging
NC	Negative control
NP	Nanoparticle
NS	Not significant
NSF	Non-spheroid forming
O_2	Oxygen
OCT	Optimal cutting temperature
OD	Optical density
P-gp	P-glycoprotein
PARP	Poly ADP ribose polymerase

PBS	Phosphate-buffered saline
PC	Positive control
pCR	Pathologic complete response
PEG	Polyethylene glycol
PI	Propidium iodide
PR	Progesterone receptor
R	Radius of the spheroid
ROUT	Robust regression and outlier removal (ROUT)
RB	Retinoblastoma-associated protein
RIPA	Radioimmunoprecipitation assay
RNA	Ribonucleic acid
S	Area of the spheroid (μm^2)
SEM	Standard error of the mean
SEER	Surveillance, Epidemiology, and End Results
SRB	Sulforhodamine B
TME	Tumour microenvironment
TNBC	Triple-negative breast cancer
TP53	Tumour protein p53
TRAIL	Tumour necrosis alfa apoptosis inducing ligand
Tris	Tris(hydroxymethyl)aminomethane
V	Volume of spheroid
VC	Vehicle control
VEGF	Vascular endothelial growth factor
WHO	World Health Organization

Units of measurement

%	Percentage
nM	Nanomolar
µM	Micromolar
µm	Micrometre
nm	Nanometres
M	Molar
g	Grams
µg	Micrograms
mg	Milligrams
Kg	Kilogram
µL	Microlitre
mL	Millilitres
v/v	Volume per volume
w/v	Weight per volume

Statistical significance indicators

*	$P \leq 0.05$
**	$P \leq 0.01$
***	$P \leq 0.001$
****	$P \leq 0.0001$

List of Figures

List of Tables

Chapter 1: Introduction

1.1 Cancer

The human genome is susceptible to aberrant alterations and damage; however, cell cycle regulatory mechanisms are present to protect or reverse such effects.[1] Failure in cell cycle regulation results in uncontrolled cellular proliferation and loss of normal cell behaviour, leading to cancer.[2-3] Cancerous cells in the body proliferate abnormally to an extent where they lose characteristics typical of their healthy counterparts. Ultimately, these hyper-proliferative cells may become malignant, reducing the quality of life of those afflicted by it, and potentially leading to mortality.[4]

While the cancer incidence rates are almost twice as high in developed countries compared to developing countries (Figure 1.1),[5] the mortality rates are only 8% to 15% higher in the former.[6] This discrepancy in the morbidity to mortality ratio can be attributed to limited diagnostic tools and therapeutic resources in developing countries.[7] Diagnosis and mortality rates of cancer are constantly on the rise. In the year 2012, 14.1 million new cases of cancer were identified, with 8.2 million associated fatalities.[6] In 2018, the incidence and mortality rates of cancer escalated to 18.1 million and 9.6 million, respectively.[5] The increase in cancer burden is attributed to the adoption of cancer-associated lifestyle choices including smoking,[8] physical inactivity,[9] and ‘‘Westernized’’ diets.[10-11] However, a betterment of lifestyle choices, early detection, and lowering of the currently high attrition rates of anti-cancer drugs can decrease the burden.[12]

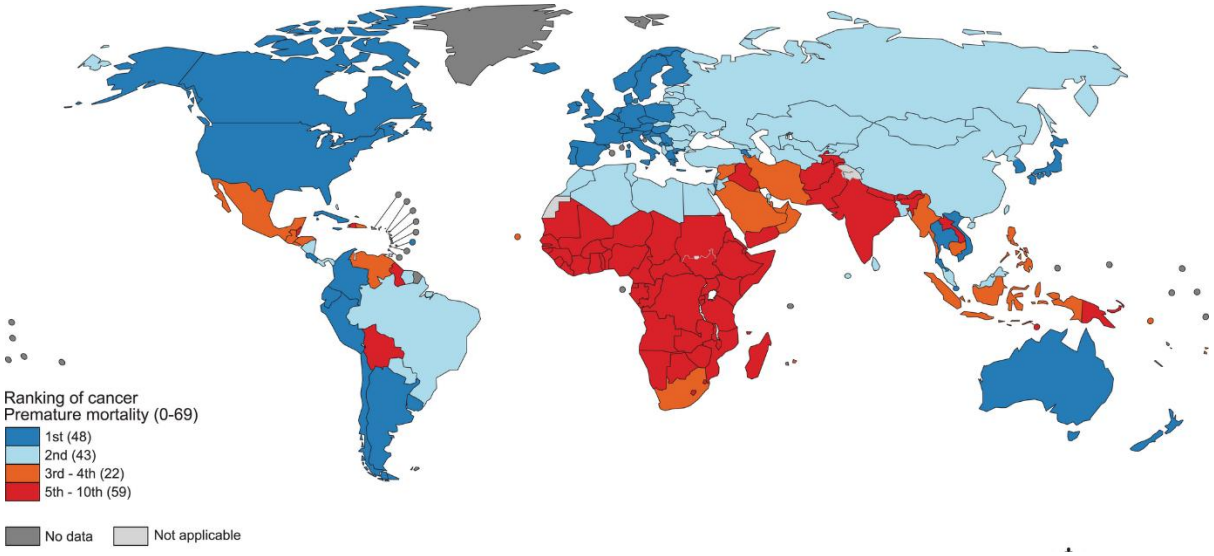

Figure 1.1: *A global map showing the national ranking of cancer as a cause of death in 2018.*[5] *Reproduced with permission from the International Agency for Research on Cancer (IARC).*

1.2 The hallmarks of cancer

Abnormal proliferation may lead to the formation of tumours (the physical manifestations of cancer). Tumourigenesis is a multi-step process where healthy cells transform into a cancerous state by acquiring biological capabilities that sustain tumour progression.[4] These capabilities coined the hallmarks of cancer (Figure 1.2),[13] include sustained proliferative signaling, evading growth suppressors, resisting cell death, enabling replicative immortality, inducing angiogenesis, and activating invasion and metastasis.[4] Compounding this, several new enabling factors have been identified that contribute to tumourigenesis.[13]

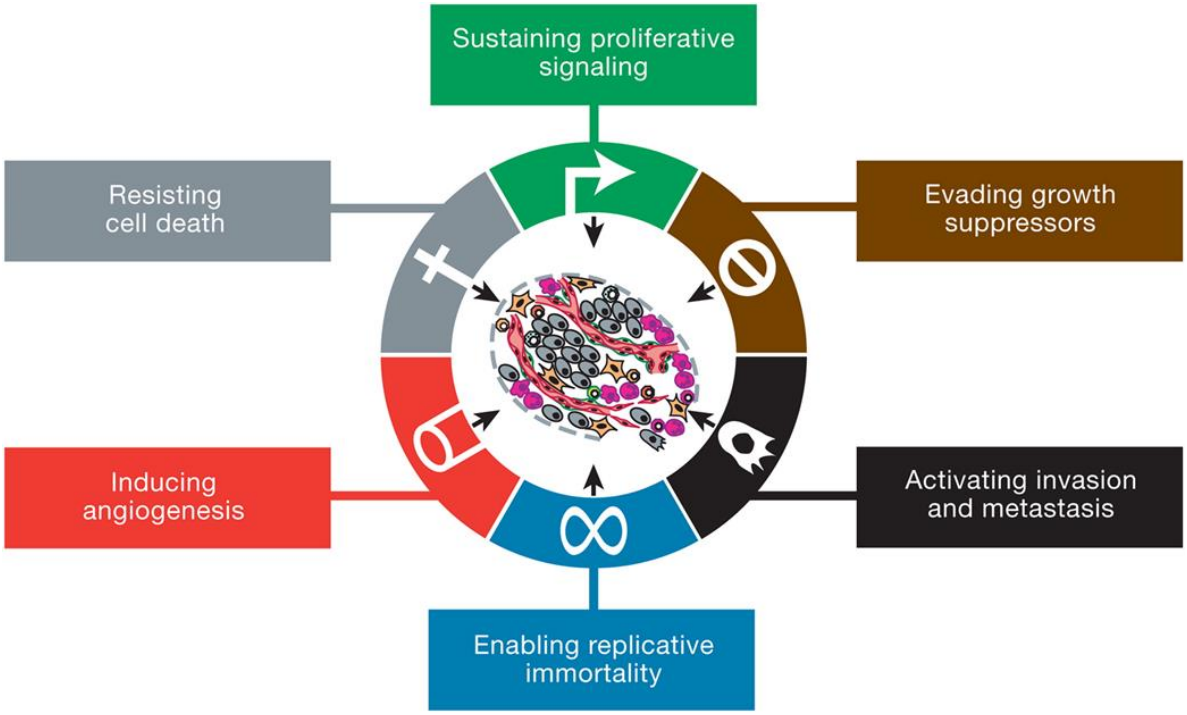

Figure 1.2: *The hallmarks of cancer cells.[13] Image reproduced with permission from Elsevier, license number: 4513561000413.*

1.2.1 Sustained proliferative signaling

The fundamentally outstanding feature of cancerous cells is their ability to chronically sustain proliferation. The signals that regulate the homeostatic growth of cells in healthy tissue are disrupted in cancer cells.[13] Persistent proliferative signaling in cancer cells is achieved through several ways, such as i) the secretion of growth factor ligands which ultimately result in autocrine proliferative stimulation, ii) stimulation of neighbouring healthy cells to secrete growth factors that regulate cell cycle progression,[14] iii) overexpression of growth receptors[15] or iv) via growth factor-independent proliferative signalling.[16]

1.2.2 Evading growth suppressors

In addition to maintaining high proliferative rates, cancerous cells circumvent mechanisms that negatively regulate cellular proliferation, a phenomenon mediated through the inactivation of various tumour-suppressor genes.[4] The two classical proteins encoded by the tumour suppressor genes in healthy cells are retinoblastoma-associated (RB) and tumour protein p53 (TP53). The RB protein serves as a cell cycle gatekeeper through recognition of intrinsic and extrinsic cellular signals that promote or prevent cell cycle progression.[17-18] After sensing intracellular stress signals such as low oxygen (O_2), low nucleotide pools or subminimal glucose concentrations, the TP53 protein mediates apoptosis and halts cell cycle progression.[19] The mutation or functional inactivation of these two proteins in cancer enables the cells to evade critical growth suppressing signals that regulate normal cell division.[13]

1.2.3 Resisting cell death

Maintenance of the healthy physiology of tissue is achieved by the homeostatic balance between proliferation and cell death.[20] Apoptosis (programmed cell death) is a well-studied natural barrier against the development of cancer.[21] Healthy cells respond to stress signals by activating either the extrinsic (death receptor-mediated) or intrinsic (mitochondrial) apoptotic pathways. Despite cancer cells being constantly exposed to stress signals, such as genomic instability and cellular hypoxia, they are able to evade these apoptotic pathways.[22] Amongst other reviewed mechanisms,[23] resistance to apoptosis by cancer cells can be achieved through overexpression of anti-apoptotic proteins[24] and/or downregulation of pro-apoptotic proteins.[25]

1.2.4 Enabling replicative immortality

A widely-accepted notion is that cancer cells replicate unlimitedly, and as a consequence, develop into macroscopic tumours.[13] This hallmark is distinct from the behaviour of non-cancerous cells, which are only limited to a number of replication cycles. The genomic integrity of healthy cells is maintained by specialized nucleic acid-protein complexes known as telomeres.[26] Successive cell cycle divisions shorten the telomeres, leading to genomic instability.[27] Two lines of defence exist to prevent unlimited replication in healthy cells. Cells with damaged telomeres are removed through induction of permanent cell cycle arrest and tissue remodelling; a process known as senescence.[28-29] When extreme telomere damage occurs, the cells go

through a telomeric crisis phase, which is characterised by cytogenic anomalies and cell death.[30] In the majority of cancer cells, the telomerase enzyme lengthens the telomeres, allowing for the circumvention of senescence and telomeric crisis. This in-turn enhances the limitless replicative potential, and ultimate survival of cancer cells.[26]

1.2.5 Inducing angiogenesis

Tumour cells need extensive vasculature for O_2 perfusion, nutrient supply and elimination of metabolic waste. Tumours cannot metastasize nor grow beyond 2-3 mm^3 without sufficient vasculature.[31-32] The tumour-associated neovasculature is generated through angiogenesis, a process that involves rapid division and migration of endothelial cells from pre-existing blood vessels. Hypoxia is the major driver of tumour angiogenesis.[33] Endothelial cells are enriched with sensors of the hypoxia-inducible transcription factor (HIF) family.[31] The HIF transcription factor released from the hypoxic cancer cells activates genes encoding the vascular endothelial growth factor (VEGF), a cardinal growth factor for angiogenesis.[34] In addition to HIF-mediated transcriptional activation, VEGF is overexpressed in various cancers through direct growth-signaling pathways.[35]

1.2.6 Activating invasion and metastasis

Cancer cells often migrate from their primary tumour site to both neighbouring tissue and distant organs; a process known as metastasis.[36] Through metastasis, secondary tumours develop that play a major role in the morbidity and mortality related to cancer.[36] Tumour cell invasion is an integral part of metastasis and involves degradation of the basement membrane and dysregulation of proteins that mediate cellular migration.[37] Various cellular adhesion molecules play a role in the sequential processes of metastasis and invasion,[13] with E-cadherin being one such an example. E-cadherin is responsible for maintaining cell-cell adhesion. Should loss of the protein occur in cancer, it leads to the enabling of the metastatic cascade.[38] Additionally, molecules that are normally involved in embryogenic cellular migration, are overexpressed in cancer. A typical example is N-cadherin, which has been shown to promote metastasis through facilitating epithelial-mesenchymal transition:[39] a mechanistic process that enhances the migratory and invasive potential of cancer cells.[40]

1.2.7 Enabling characteristics and emerging hallmarks of cancer

A decade after the initial description of the hallmarks of cancer, new experimental evidence led to the identification and description of a new generation of cancer-cell capabilities, which encompass enabling characteristics and emerging hallmarks.[13] The enabling characteristics include genomic instability, an alteration of the cells' genome during successive divisions[41] and tumour promoting inflammation.[42] The emerging hallmarks involve circumvention of destruction by the immune system[43] and the reprogramming of cellular energy metabolism.[44]

1.3 Breast cancer

Cervical, colorectal, liver, lung, and breast cancers are responsible for over half (54%) of the incidence burden of cancer in developing countries.[45] Following lung cancer, breast cancer is the second most commonly diagnosed and cause of cancer-associated deaths globally.[5] In females, breast cancer is the most frequently diagnosed cancer, and the leading cause of cancer mortality in the majority of countries in the world (Figure 1.3).[5] In the year 2012 alone, approximately 1.7 million new cases of breast cancer were identified, with 521,900 associated fatalities.[6] These numbers have since increased, where in 2018, 2.1 million people were diagnosed with breast cancer and 626,679 individuals succumbed to the disease.[5]

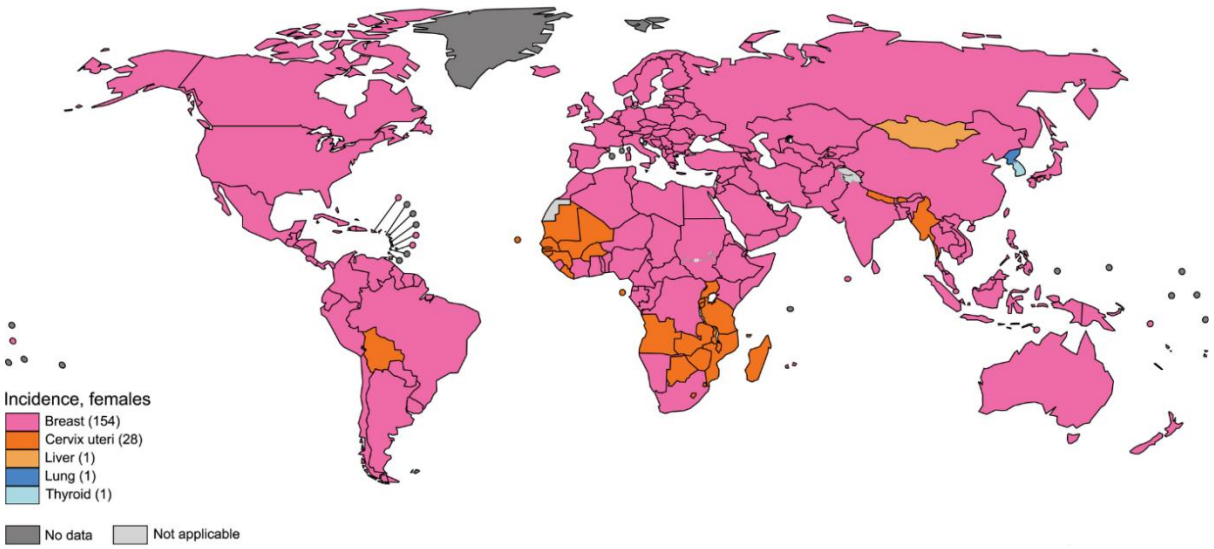

Figure 1.3: *Global map showing the ranking of breast cancer as the most commonly diagnosed cancer in females per country in 2018.[5] Reproduced with permission from the IARC.*

1.3.1 Risk factors of breast cancer

The neoplastic transformation of healthy breast cells is multifactorial. Both endogenous/intrinsic and exogenous/extrinsic risk factors are associated with the development thereof.[46]

1.3.1.1 Intrinsic risk factors of breast cancer

Although breast cancer is predominantly diagnosed in females,[46] males may also be sporadically afflicted by the neoplasm (1% of diagnosed breast cancer cases).[47] Being female is, therefore, an inherent risk factor for developing breast cancer.

The age at the time of diagnosis also plays a key role in the incidence of the neoplasm. An increase in age is associated with a higher risk of developing the disease.[48] Women older than 45 years are more likely to have the disease compared to younger individuals; it is, therefore, imperative for women to have a mammography screening before they reach 45 years of age.[49]

Race remains a major intrinsic risk factor that influences the occurrence of breast cancer.[50] Analysis of a Surveillance, Epidemiology, and End Results (SEER) database showed that the incidence (127.4 in 100,000 individuals) and 5-year survival rate (90.4%) of breast cancer were higher amongst Whites, compared to Blacks, who had an incidence and 5-year survival rate of 121.4 in 100,00 individuals, and 78.6%, respectively.[51]

Dysfunction of various hereditary genes makes some people more susceptible to breast cancer. Germline mutations of the breast cancer susceptibility genes 1 and 2 (BRCA1 and BRCA2) are commonly associated with a 65% increase in the risk of breast cancer occurrence.[52] These genes primarily play a role of tumour suppression, and their dysfunction results in selective growth advantages and accelerated proliferation of tumours.[53]

High concentrations of endogenous estrogen, as well as changes of the hormonal levels during maturation, also have an impact on the potential for developing breast cancer.[46] Early menarche leads to prolonged exposure to estrogen and consequential development of breast cancer.[54] Additionally, early-age pregnancy and due date delivery are known to serve a protective function against hormone receptor-positive breast cancer; thus, these factors could lower the risk of breast cancer.[51]

1.3.1.2 Extrinsic risk factors of breast cancer

The risk of breast cancer can also be influenced by exogenous hormonal exposure and other external risk factors.[46] Elucidation of the role of extrinsic factors in the development of breast cancer is imperative, as the number of women using contraceptive medication and hormone replacement therapy (HRT) is increasing.[55] The risk of breast cancer is higher in women who use contemporary contraceptives compared to those who do not, and the risk increases with prolonged duration of use thereof.[56] Extensive evidence shows that use of HRT is correlated with an increased risk of breast cancer,[57] predominantly with combination therapies containing both estrogen and progesterone.[46,58]

Dietary habits are an additional external factor that influences breast cancer risk.[59] Foods that are rich in fat lead to weight gain or obesity, which increases the risk of breast cancer.[60] Furthermore, the chemical entities that are added to food that act as colorants or preservatives can potentially augment the neoplastic transformation of healthy breast tissue.[46] Alcohol alters the metabolism of estrogen in the liver, and, therefore slight consumption of alcohol could increase the risk of neoplasm occurrences.[61] To combat this, dietary interventions, such as consuming foods rich in antioxidants and vitamin D, can reduce the breast cancer risk by up to 20%.[62]

1.3.2 Classifications of breast cancer

Breast cancer is a cluster of diseases characterised by distinct histopathological oddities, heterogeneous molecular cues and differential response to therapy.[63-65] Copious evidence suggests that breast cancers with different morphological features behave differently and should be approached with different treatment strategies.[66-67] For decades, clinicopathological features of tumours (e.g. stage and grade) have been used as a basis for classifying different types of breast cancers.[68] However, histologically-identical cancers may behave differently and have distinct susceptibility to similar therapeutic approaches.[67] The advent of advanced microarrays in biological research has led to the discovery of receptors[69-70] and molecular traits[71] that underpin the heterogeneous behaviour of different types of breast cancer.

1.3.2.1 Hormone-receptor classification of breast cancer

Initially regarded as a predictor of response to therapy, expression of hormone receptors is now considered to be the main biological feature of breast cancers, and is used for molecular and prognostic taxonomy of breast cancer.[71] Three common types of receptors are known to fuel the growth of breast cancers, namely estrogen (ER),[70] progesterone (PR), and human epidermal growth factor receptor 2/erb-b2 receptor tyrosine kinase 2 (HER2/ERBB2) receptors.[15,72]

The hormone estrogen modulates physiological processes such as the development of reproductive organs and the homeostatic regulation of cardiovascular, immune, and central nervous system functions. These effects of estrogen are regulated by the ER, which primarily exists in two isoforms (ERα and ERβ).[73] In ER-overexpressing breast cancer, binding of estrogen to the ER stimulates proliferation of mammary cells, leading to an increased risk of replication errors, ultimately resulting in mutations that are implicated in disruption of normal cellular functions such as apoptosis, and DNA repair. As such, drugs that either reduce biosynthesis of estrogen (aromatase inhibitors) or act as antagonists for estrogen (selective estrogen receptor modulators) are used for the treatment of ER-positive breast cancers.[74]

Progesterone is another steroid hormone implicated in the pathogenesis of some breast cancers. Progesterone normally plays a major role in different reproductive processes in women, such as; embryo implantation, sexual maturation, lactation, and breast tissue development during puberty.[75] These effects are mediated through interaction with two main variants of the high-affinity PR, namely the PR-A and PR-B isoforms.[76] The PR-A isoform is involved in uterine and reproductive-associated functions, while the PR-B regulates breast tissue development.[77] In PR-overexpressing cancers, abnormal proliferation is achieved through both PR-mediated autocrine/paracrine signaling and PR-dependent transcriptional activity.[78] Slow advancement has been made in the successful development of PR-targeted treatment strategies. Antiprogestins have demonstrated anti-cancer efficacy in *in vitro* and animal models,[79] however, the clinical investigation of these compounds had to be halted due to off-target nuclear receptor binding, and consequential altered hepatic function.[80] Next-generation antiprogestins have greater selectivity for the PR, and their

experimental anti-tumour efficacy has renewed the optimism for using PR targeting in the treatment of breast cancer.[81]

The HER2 receptor is a member of the human epidermal growth factor family, which includes the epidermal growth factor receptor, HER2, HER3 and HER4.[82] The principal functions of this family of receptors are to promote growth, differentiation, survival, and proliferation. Overexpression of the HER2/ERBB2 gene plays a crucial role in the etiology of approximately 15% of breast cancer cases.[15] This overexpression of the HER2 gene results in a 10- to 20-fold increase in the HER2 protein and subsequent expression of 2 million receptors on the surface of the tumour cell.[83] The discovery of trastuzumab (HER2 monoclonal antibody) and other several biologics such as pertuzumab, lapatinib and trastuzumab emtansine has profoundly revolutionized and improved the clinical outcome of HER2-overexpressing breast cancer.[84]

Analysis of receptor overexpression can, therefore, be used to classify the neoplasm into ER-positive, PR-positive, and HER2-positive breast cancer, which also assists with the selection of treatment modalities.[71] However, some breast cancers overexpress none (for example, triple negative breast cancer or TNBC)[85] or more than one of these receptors,[86] and have various gene expression profiles.[71] This necessitated the need to cluster breast cancer into subtypes that encompass and emphasize the molecular heterogeneity of the disease.[87]

1.3.2.2 Molecular classification of breast cancer

Profiling of DNA and RNA alterations in primary breast cancer samples has led to the classification of breast cancer into four intrinsic molecular subtypes; luminal A, luminal B, HER2-enriched, and basal-like breast cancer.[88] An additional subtype known as normal-like is commonly described in literature, however, it is thought to arise from contamination of samples with non-cancerous mammary tissue.[89] The four intrinsic subtypes have distinct histology, prognosis and hormone-receptor and gene expression profiles. The difference between various features of the different molecular subtypes is summarized in Table 1.1.

Table 1.1: *Comparison of the intrinsic molecular subtypes of breast cancer. Table adapted from Eliyatkın et al. 2015.*[87]

	Intrinsic molecular subtype			
Features	**Luminal A**	**Luminal B**	**HER2**	**Basal-like**
Prevalence of invasive breast cancer	50%	20%	15%	~15%
Hormone-receptor expression	ER+, PR+, HER2-	ER+, PR+, HER2 variable	ER-, PR-, HER2+	ER-, PR-, HER2- (triple-negative)
Gene expression profile	LMW[a] luminal cytokeratins, high expression of hormone receptor and related genes	LMW luminal cytokeratins, medium expression of hormone receptor-related genes	High expression of HER2, low expression of ER genes	Basal epithelial and basal cytokeratin genes. Low expression of hormone receptor genes.
Response to targeted therapy	Endocrine therapy effective	Endocrine therapy effective (less than luminal A)	Trastuzumab effective	Endocrine therapy & trastuzumab not effective
Response to general chemotherapy	Variable	Variable	Responds to anthracyclines	Responds to PARP[b] inhibitors and platinum compounds
Prognosis	Good	Good	Unfavourable	Poor

[a]LMW = low molecular weight. [b]PARP = Poly-ADP-ribose polymerase.

Of the four molecular subtypes, basal breast cancer has the worst clinical outcome and is associated with high proliferative rates.[90] The most common feature of the basal subtype is the frequent lack of overexpression of the ER, PR, and HER2 receptors (triple-negative). The terms “basal breast cancer” and “TNBC” cannot simply be interchanged, as not all basal subtypes are triple-negative, and discordance of 30% has been described between basal breast cancer and TNBC (a separate sub-classification of breast cancer).[91]

1.3.3 Triple-negative breast cancer

Approximately 12 to 17%[85] of breast cancer patients have TNBC. The TNBC subtype is immunohistochemically defined as breast cancer that has no overexpression of HER-2/ERBB2 and is both ER- and PR-negative. A characteristic trait of TNBC is its aggressive nature and high relapse rate compared to non-TNBCs.[85] In a study of 1,601 women with breast cancer, women with TNBC had a distal recurrence rate of 33.9% compared to 20.4% in patients with non-TNBC.[92] The clinical features of TNBC are summarized in Table 1.2.

Table 1.2: *Clinical characteristics of triple-negative breast cancer.*

Characteristic	**Description**	**Reference**
Patients at risk	• Premenopausal women • African origin • Presence of BRCA1 mutation	Newman et al[93]
Tumour features	• Lack ER, PR and HER2 • Large, with involvement of axillary node • Rapid mitotic rate • Infiltrating ductal carcinoma	Schmadeka et al[94]
Treatment and prognosis	• Sensitive to chemotherapy • No approved targeted drugs • Poor prognosis	O’Reilly et al[95]

The TNBC subtype is heterogeneous, and approximately 75% of all TNBCs are basal-like (BL). This led to the further classifications of breast cancer into six molecular subtypes, namely BL-1 and BL-2, immunomodulatory, mesenchymal, mesenchymal stem cell-like, and luminal androgen receptor.[96] The molecular alterations in these different subtypes can, therefore, potentially be exploited in the therapeutic targeting of pathways implicated in TNBC.[97]

1.3.3.1 Treatment of triple-negative breast cancer

Hormone and growth factor receptor-targeted therapy is ineffective in individuals with TNBC due to the lack of receptor overexpression. Surgery and chemotherapy remain the only available treatment modalities for TNBC patients. Currently, the optimal chemotherapeutic strategy for the specific treatment of TNBC has not been tailored.[98] Chemotherapy approaches that are used for the treatment of other main subtypes of breast cancer are also used in TNBC. Adjuvant chemotherapy is recommended for stage I (tumour size > 0.5 cm) breast cancer,[98] and neoadjuvant chemotherapy is used in early stages of the neoplasm with a goal of breast-conserving lumpectomy, or for patients who temporarily cannot undergo surgery.[99]

Third-generation adjuvant or neoadjuvant regimens consisting of taxane combined with cyclophosphamide/anthracycline-based formulations are currently used as chemotherapy.[85] This treatment regimen results in a higher pathologic complete response (pCR) in TNBC (28-30%), compared to hormone receptor-positive breast cancer (6.7%).[99] Docetaxel and paclitaxel are examples of taxanes that are used in this regimen. These drugs execute their antineoplastic activity through stabilization of microtubule dynamics, and consequential disruption of the cell cycle.[100] Cyclophosphamide is a pro-drug that is converted through enzymatic and chemical activation into nitrogen mustard. This product results in inter-strand and intra-strand crosslinking of DNA that account for the cytotoxic activity of cyclophosphamide.[101] Anthracyclines are a class of cytotoxic compounds that are derived from antibiotics, and doxorubicin is a classic example.[102]

Doxorubicin remains one of the most commonly used chemotherapeutic drugs to date. Doxorubicin exerts its anticancer activity through inhibition of topoisomerase I and II, and intercalation with DNA to disrupt its uncoiling, ultimately leading to programmed cell death.[102] The aglycone (glycoside-free) component of doxorubicin is composed of a tetracyclic ring with quinine-hydroquinone adjacent groups, a methoxy-substituent side chain, and a terminal carbonyl group. A 3-amino-2,3,4–trideoxy-L-fucosyl moiety forms the sugar (daunosamine) component of the drug via a glycosidic bond with one of the rings in the aglycone component.[102] Hydrochloric acid (HCl) is added to enhance the solubility of the drug to form the doxorubicin-HCl salt (Figure 1.4).

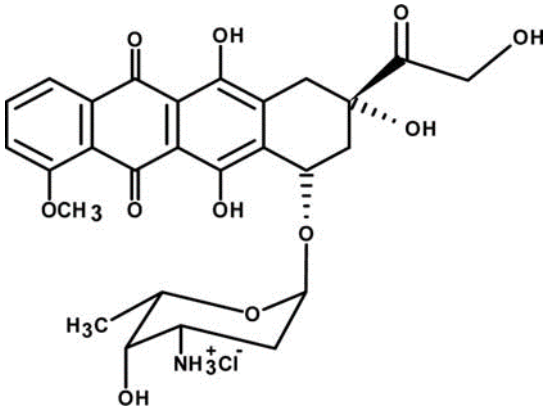

Figure 1.4: *The chemical structure of doxorubicin hydrochloride.[103] Permission for the re-use of image was obtained from Springer Nature. License number: 4531700037775.*

The DNA intercalation and inhibition of DNA and RNA polymerase by doxorubicin results in cessation of DNA replication and RNA transcription. Furthermore, doxorubicin may exert its antitumor effects through DNA unwinding, generation of free radicals which aggravates DNA damage, and inhibition of the production of macromolecules.[102] Together with the binding of other molecular targets such as topoisomerase I and II, broad cytotoxic effects occur in conjunction with antiproliferation via various mechanisms. The anticancer mode of action of doxorubicin depends on the concentration, duration, and type of cancer.[102]

The addition of platinum agents is currently being investigated as an alternative chemotherapeutic approach in TNBC. In the recent GeparSixto trial, increased pCR rates and long term disease-free survival were noted in patients treated with carboplatin compared to those treated with paclitaxel and non-pegylated-liposomal doxorubicin.[104] In addition to this, various techniques are used to identify the molecular alterations in TNBC in a bid to identify and clinically peruse the efficacy of novel

therapeutic entities that target such aberrations.[105] The molecular classification methods, associated novel compounds, and the currently used classical chemotherapeutics for TNBC are presented in Figure 1.5.

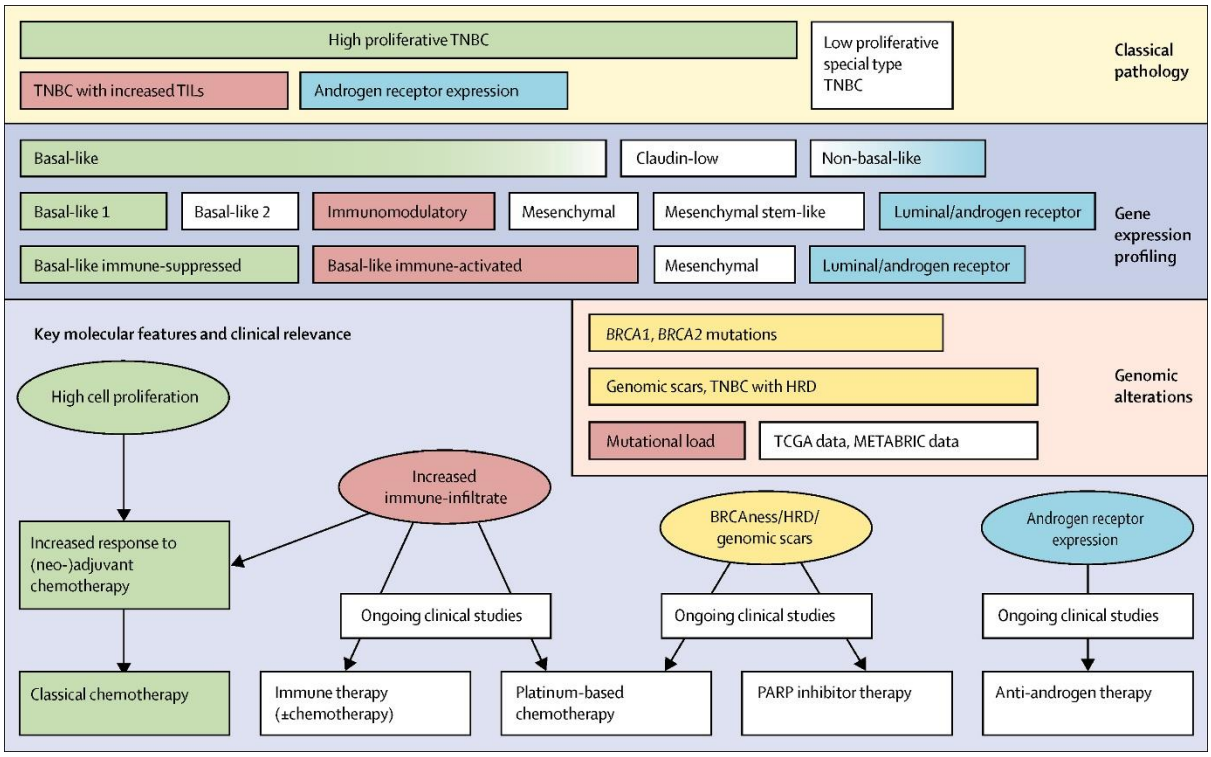

***Figure 1.5**: Molecular alterations and associated therapeutic targeting in triple-negative breast cancer.[105] Image reproduced with permission from Elsevier, license number: 4513560720461.*

Although conventional chemotherapy results in higher pCR, TNBC is associated with higher relapse rates compared to other breast cancer subtypes. This phenomenon is known as the triple-negative paradox, which is primarily driven by high relapse rates of some patients who have residual disease after chemotherapy.[106] This necessitates the development of predictive markers in TNBC, to allow for the identification of patients with a high likelihood of recurring after neoadjuvant chemotherapy.[106] Despite advancement in the characterisation of the genetic alterations and molecular drivers of cancer, oncology drugs are associated with higher attrition rates compared to drugs for other ailments.[107] Though there are various reasons for these high attrition rates, the historical inability to efficiently translate pre-clinical research to clinical success is a major cause.[108]

1.3.3.2 The role of pre-clinical cancer research in drug development

The drug development process is time-consuming and costly. It costs approximately 1.4 billion United States dollars and takes 12 to 24 years for a single drug candidate to be clinically approved.[109] The process begins with the identification and synthesis of a novel chemical with potential efficacy, followed by appropriate *in vitro* and *in vivo* testing to assess the biological activity and toxicity of the synthesized compound.[109] Upon collation of corroborating and satisfactory results from cell culture and animal studies, an Investigational New Drug Application is submitted to the Food and Drug Administration in the United States (or each country's respective regulatory authority) before clinical trials are initiated. Clinical trials involve sequential evaluation of safety and dose range (phase I), efficacy and side effects (phase II), and subsequent recruitment of many patients to develop a wide database for efficacy and safety (phase III).[109] Following clinical investigations, various regulatory procedures have to be conducted before the drug is approved for clinical use (Figure 1.6).[109]

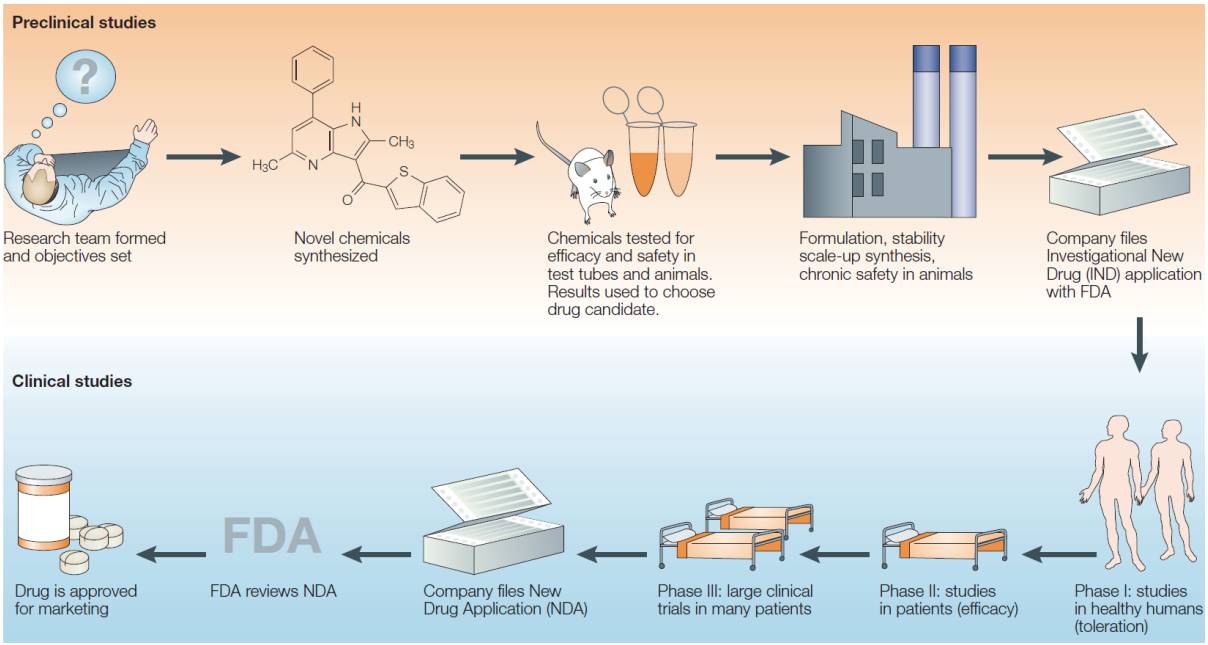

Figure 1.6: *Stages of the drug development process.[109] Image reproduced with permission from Springer Nature, license number: 4513561342470.*

The attrition rates for oncology drugs are higher than those for other ailments, and most novel drugs fail during phase III of clinical trials. Despite various improvements in the execution of clinical trials, 84% of investigational breast cancer drugs are discontinued during clinical trials,[110] therefore, drug attrition remains a major cost driver in drug development. Additionally, high attrition rates further aggravate the societal need for truly-innovative drugs that are effective against diseases without optimally-available treatment avenues.[111] The costly and time-consuming nature of drug development necessitates the elucidation and consideration of intricate interactions of the tumour cell environment in the design and synthesis of optimally effective anticancer compounds.

1.3.4 The tumour microenvironment

The tumuoral niche consists of cellular and non-cellular components which make up the tumour microenvironment (TME). The main components of the TME include cancer-associated fibroblasts (CAFs), immune cells, blood vessels, lymphatic vessels, and various other components of the extracellular matrix (ECM).[112] Collectively, these components play a substantial role in tumour initiation, growth and invasion through the production of different growth factors and chemokines.[113] As such, identification of biological alterations within the TME is used in the therapeutic targeting of the key physiological and molecular role players in cancer.[114]

A major biochemical alteration within the TME is the development of permanent or transient hypoxic regions due to aberrations in the neovasculature and poor blood perfusion.[115] In a rapidly growing tumour, cells that are further from blood vessels receive poor O_2 and nutrient supply, while those peripheral to the blood vessels are richly perfused. In a hypoxic environment, the tumour cells switch to glycolytic metabolism, which leads to the accumulation of acid in the TME.[116] The products from the glycolytic metabolic pathway are then subsequently used by the cancer cells for growth. The mediated-type stromal cells within the hypoxic environment release signaling molecules that promote the transformation of fibroblasts into CAFs. These CAFs interact with the cancer stromal cells to produce a stiff ECM that supports cell migration (Figure 1.7).[115]

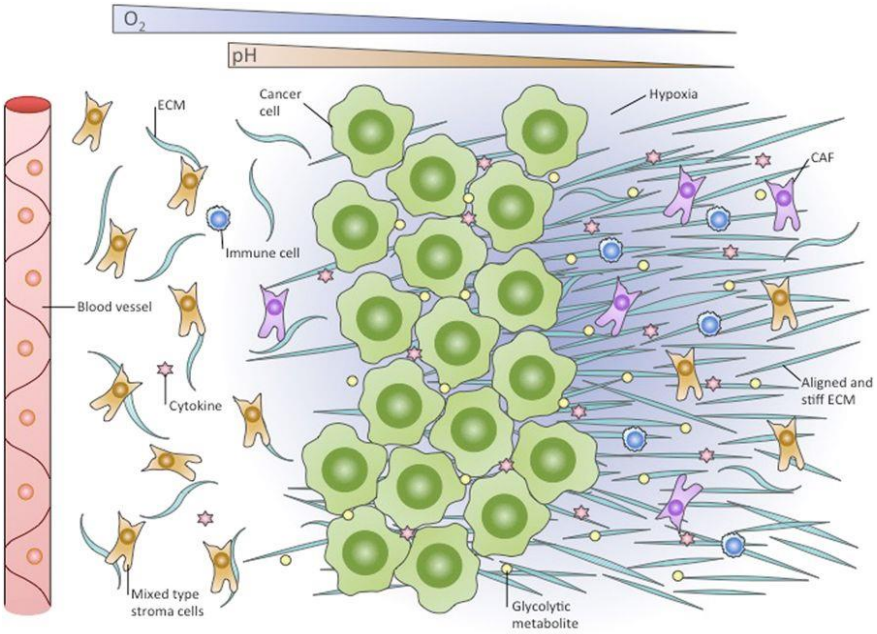

Figure 1.7: *Interactions of various cell types in the hypoxic tumour microenvironment.*[115] *Figure reproduced under the Wiley Creative Commons Attribution License (CC BY).*

In the development of anti-cancer drugs, *in vitro* platforms used for high throughput pre-clinical screening should be able to accurately produce reliable and biomedically-relevant information.[117] Considering implications of the complexity of the TME in the physiological attributes of cancer, it is imperative that the cellular environment of the *in vitro* cellular environment adequately recapitulates the phenotype of cells within the TME.[118]

1.4 Monolayer cell culture

Many groups in academia and the biomedical industry rely on the traditional, two-dimensional (2D) cell culture model for pre-clinical drug screening.[119] In this model, cells are grown on a flat, solid culture surface such as plastic or glass.[120] This forces the cells to undergo cytoskeletal rearrangement attaining artificial polarity, which results in abnormal gene and protein expression.[121] Growth and sustenance of tissue requires complex intercellular interactions in a microenvironment composed of various hormones, nutrients, growth factors, ECM components and adhesion molecules.[122] In primary tumours, a poor blood supply results in the establishment of hormone and nutrient gradients, development of hypoxic regions and zonal differentiation.[123] The cell exchange area-to-culture media ratio in 2D-models is increased, and the cells receive an excessive supply of O_2 and nutrients. Furthermore, all cells are exposed to unrealistically high concentrations of drugs when conducting drug screens. Therefore,

the O_2, hormone and nutrient gradients that are established in *in vivo* tumours are not reproduced. Moreover, cell-to-cell and cell-to-ECM interactions are not represented in this model. These interactions play a significant role in tumour growth-regulation, angiogenesis, aggression, and metastasis.[124]

It is thus apparent that the 2D-model does not optimally mimic the *in vivo* tumour microenvironment, and consequently, findings from 2D-cell culture-based experiments can only partially be translated to *in vivo* models.[125] Animal models provide a better representation of the tumour environment; however, they are more time-consuming and expensive to perform than cell culture for high throughput drug screening.[126] In a bid to circumvent these experimental inconsistencies, three-dimensional (3D) models have been suggested as a potential bridge to the gap between 2D- and animal models,[117,127] as shown in Figure 1.8.[119]

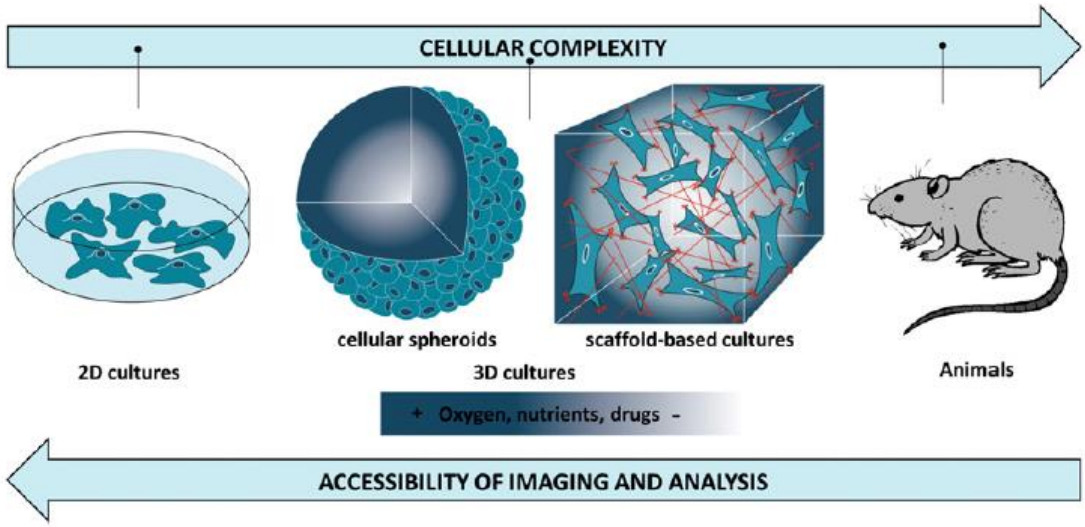

Figure 1.8: *Schematic showing use of 3D culture as a potential bridge between 2D culture and animal models.[119] Image reproduced with permission from Elsevier, license number: 4513570265432.*

1.5 Three-dimensional cell culture

Various 3D cell culture techniques exist and allow for heterogeneous cellular aggregates that resemble avascular tumour nodules/micrometastases or intervascular regions of large solid tumours with respect to micromilieu, volume growth kinetics and some histomorphological features.[128] The methods for the 3D recapitulation of tumours include; tissue explants, tumour-on-a-chip, and multicellular spheroids.[129]

To create explants, excess fat and necrotic tissue is removed from primary tumour biopsies, and after washing, the remaining tissue is cultured in a collagen matrix. After

embedding or adhesion of the processed tissue into the collagen, various experimental compounds are then added.[130] The main advantage of using explants is the maintenance of the components of an original tumour, however, the main drawback is the loss of sample uniformity due to interpatient variation.[131]

Micro-engineered 3D tumour models known as “organs-on-a-chip” are a recent innovation that remains at the frontiers of drug discovery.[132] These devices are miniaturized functional units of tumours created through the integration of microfluidics with tissue engineering, microfabrication, and biomaterials research.[133] A porous membrane containing endothelial cells provides a niche for tumour cell growth, while microfabricated channels that are imprinted onto inert material allow for navigation of circulating immune cells.[133] Combined, the components of the chip enable tissue culture, drug and nutrient supply, and waste removal functionality.[134]

Multicellular tumour spheroids are well-characterised organotypic spherical clusters that form from a single cell suspension.[135] Depending on the desired experimental requirements, various scaffold-based and scaffold-free methods can be used to generate spheroids (Figure 1.9).[131] In scaffold-based methods, synthetic hydrogels facilitate 3D spheroid formation and provide cues that promote cell-cell and cell-ECM interactions that are analogous to those in *in vivo* tumours.[136] These scaffolds can be used in bioreactors (spinning or rotating) to allow for large-scale production of multicellular spheroids. Dynamic rotating spinner flasks or bioreactors are the most appropriate method for the large-scale and long-term culturing of spheroids.[122] Such culturing techniques, however, require high quantities of cell culture medium, conflicting with the need to use small volumes during the testing of novel compounds. Moreover, when using these dynamic culturing methods, it is necessary to transfer the spheroids to stationary culture environment prior to analysis of any parameters.[122] Transferring the spheroids could potentially disrupt the original biology of the spheroids and makes the monitoring of individual spheroids a challenging task.[122]

In matrix-free platforms such as the liquid overlay and hanging drop techniques, no exogeneous artificial platforms are used to promote spheroid formation, but tight intercellular junctions result in formation of highly-organized spherical clusters that produce their own ECM.[137] These stationary spheroid culturing techniques allow for generation of spheroids with uniform sizes. Further sorting and transferring are not necessary and this allows for optimal monitoring and manipulation of spheroids.[128]

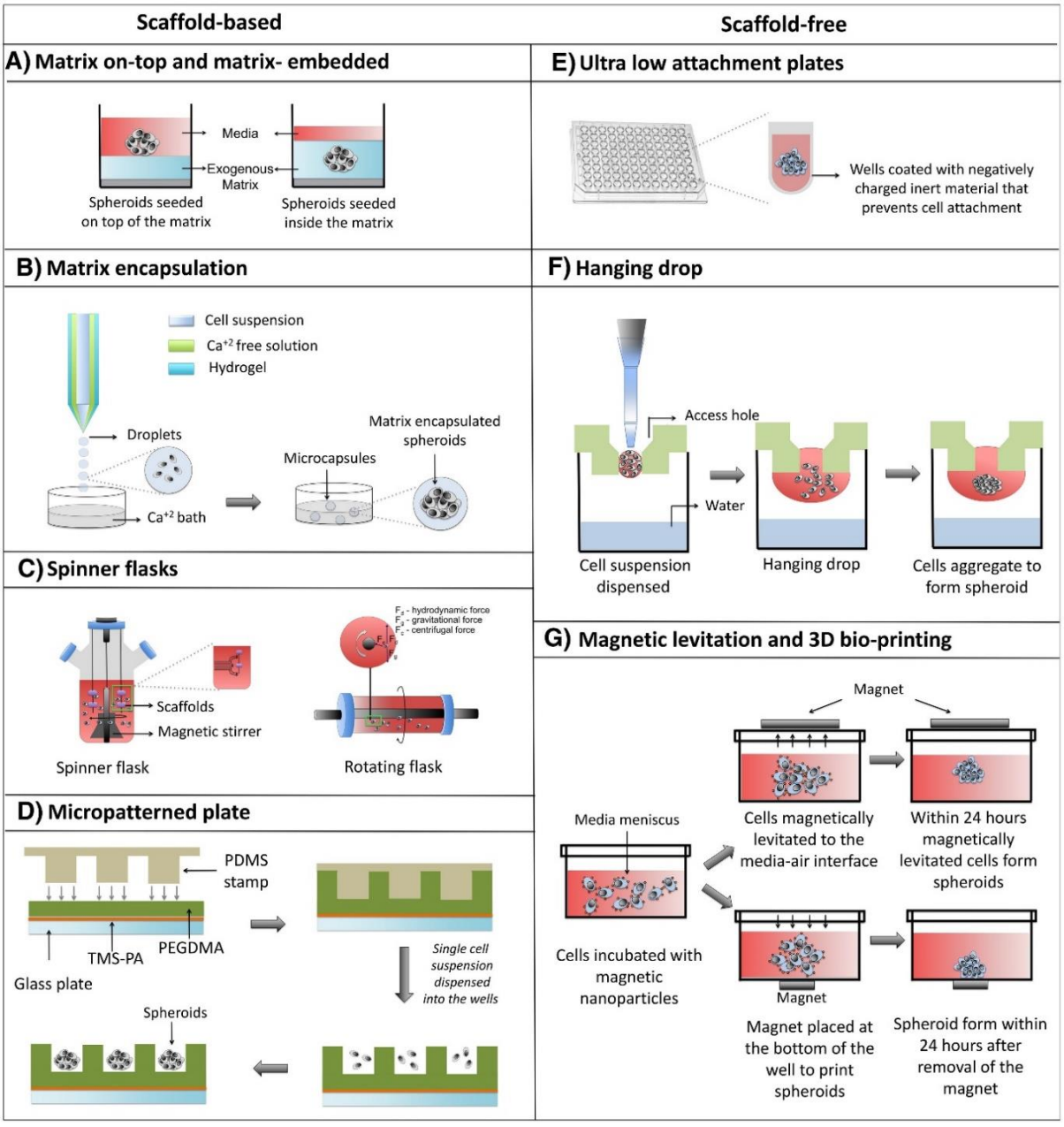

Figure 1.9: *Techniques for generating multicellular spheroids.[131] Image reproduced with permission from Elsevier, license number: 4513571185343.*

Multicellular spheroids are known to resemble *in vivo tumours* better than monolayers (Table 1.3). The growth of cells as multicellular spheroids encourages cell-cell and cell-ECM interactions that are analogous to those in the native tumour microenvironment.[129,138] Spheroids offer a diffusion limit of about 100 to 150 µm for most drugs and, therefore, provide an *in vitro* platform for evaluating mass transportation limitations that compounds may encounter *in vivo*.[139] The gene and protein expression profile in spheroids closely resembles solid tumours, compared to the conventional monolayer model.[140] Cells in the tumour microenvironment[141] are heterogeneous with respect to gene expression and regulation, proliferative capacity, metabolic stress, and drug sensitivity.[131] This feature is recapitulated by the differential spatial architecture of cells in different spheroid regions.[142]

Table 1.3: *Comparison of monolayers and spheroids with in vivo solid tumours. Table adapted from Nath and Devi.*[131]

Feature	**Monolayers**	**Spheroids**	***In vivo tumours***
Morphological zonal differentiation	x	✔	✔
Inherent hypoxia	x	✔	✔
O_2, and metabolite gradients	x	✔	✔
Glucose flux rate	Low	High	High
Cell-cell and cell-ECM interactions	Different	Similar	Similar
Gene expression profile	Different	Similar	Similar

1.5.1 Zonal differentiation of cells in spheroids

Decreasing nutrient and O_2 concentrations from the outer surface of the spheroid to the core results in a heterogeneous cellular arrangement, with an outer layer of actively-proliferating cells, a middle layer of quiescent cells, and a core of necrotic cells.[143] In this manner, spheroids resemble the architecture of poorly vascularised microregions of *in vivo* tumours (Figure 1.10).

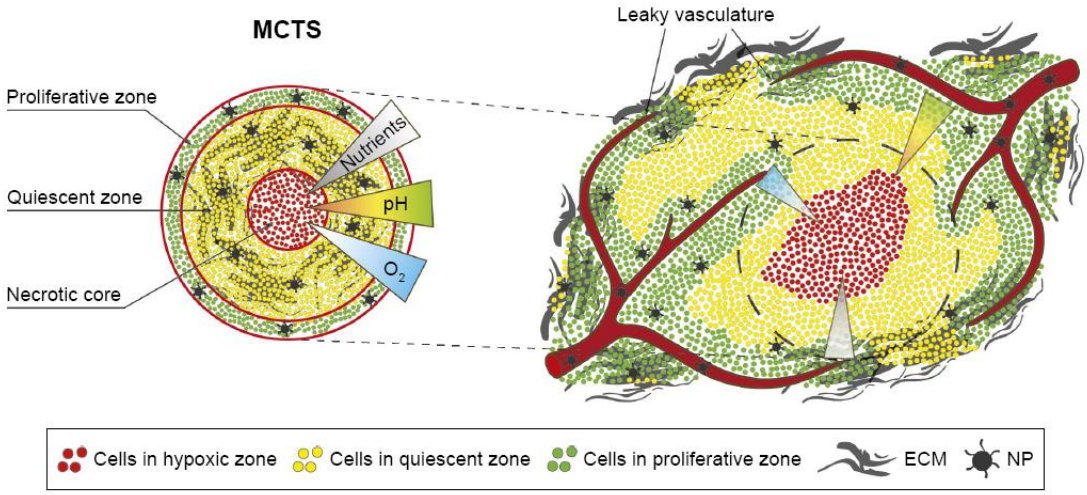

Figure 1.10: *Schematic showing the resemblance multicellular spheroids with tumour microregions.[144] Permission for re-print provided under PubMed Central open source copyright law. MCTS = multicellular tumour spheroid, ECM = extracellular matrix, NP =nanoparticle.*

1.5.1.1 The necrotic centre

Due to low O_2 delivery to the spheroid core, cells within this region encounter hypoxic stress and subsequent necrosis.[145] Hypoxic conditions in tumours result in the stabilisation of hypoxia-inducible factor 1α (HIF 1-α), a transcription factor implicated in activation of genes associated with angiogenesis and survival.[34] Activation of these genes leads to alteration of biochemical pathways, which may result in an increase of cells with a drug-resistant phenotype.[146] The HIF-1α transcription factor promotes a metabolic switch from oxidative phosphorylation to aerobic glycolysis and lactic acid fermentation.[13] Accumulation of lactic acid results in lowering of the pH within the tumour microenvironment. Acidic conditions result in protonation of basic anti-neoplastic agents, leading to the reduction of drug cellular uptake and efficacy. For example, a 2012 study[147] demonstrated that the uptake of doxorubicin into cells decreased with depth into colon cancer spheroids, where acidic regions (pH = 6.4) had a 1.7-fold lower uptake compared to regions with a higher pH. Additionally, hypoxic conditions promote radio-resistance, as drugs like doxorubicin need O_2 to produce DNA-damaging free radicals.[148]

1.5.1.2 The quiescent zone

As a consequence of moderate O_2 perfusion and nutrient supply,[149] cells adjacent to the hypoxic core enter quiescence.[125] Quiescent cells are viable, metabolically-active cells in a reversible state of growth arrest.[149] Elucidation of the molecular mechanisms responsible for tumour cell dormancy is a challenging area in oncology research which awaits exploration.[150] This is in part due to the low abundance of disseminated dormant cells in blood and tissue samples,[151-152] rendering characterisation of these cells extremely difficult.[149] Many potential mechanisms implicated in tumour cell dormancy and chemotherapy resistance have been proposed and reviewed.[150] For example, it has been reported that signaling of p38 in dormant cells results in promotion of survival and protection from chemotherapy.[153] This mitogen-activated protein kinase plays a role in the biosynthesis of pro-inflammatory cytokines,[154] however, studies have shed light into the role of p38 in the regulation of other processes such as cellular dormancy.[153] When re-perfused in a solid tumour, quiescent cells are able to resume growth and repopulate the tumour.[155] Most conventional and genotoxic anticancer drugs target an aspect of the replication process,[155] and it is, therefore, likely that cancer cells that have entered a quiescent state would not be killed by antineoplastic drugs. If quiescent cells are present in large numbers they could contribute to the recurrence and drug resistance seen in TNBC.[156] The notion that the lack of proliferation in dormant cells is the sole reason for chemoresistance still needs to be confirmed.[153] Molecular characterisation of quiescent regions within spheroids can, therefore, prove useful in the discovery of pathways implicated in quiescence-related chemoresistance. Furthermore, use of 3D-culture in drug screening can aid in the identification of compounds that specifically target the dormant spheroid core regions, which would not be identified in 2D-culture models under similar conditions.[129] A high-content-based screen has been shown to be effective in identifying compounds that specifically induce cell death in inner spheroid core regions, which would not be detectable using 2D culture models.[125]

1.5.1.3 The proliferative zone

The cells on the outer rim of the spheroids proliferate rapidly, due to rich O_2 and nutrient supply. Considering that most anticancer drugs target actively proliferative cells, the cells in the proliferative zone can be more sensitive to antineoplastic drugs, compared to cells in inner regions. Persistence of high proliferative indices is

recognised as a fundamental trait of cancerous cells.[13] Tumour cells acquire the ability to proliferate rapidly through upregulation of growth factor receptors, or stimulation of growth factor release from normal cells.[14] Additionally, mutations of the p53 tumour suppressing gene result in loss of function, leading to typical hallmarks of cancer, including sustained proliferation.[157] Mutant p53 proteins are expressed in many cancers and are therefore attractive targets for cancer therapy.[158]

Biomolecular pathways may thus be upregulated or downregulated in the different regions of the 3D-tumour spheroids, potentially resulting in circumvention of anti-cancer drug action. The 3D-models provide an attractive platform for pre-clinical cancer drug screening, as they combine the flexibility and cost-effectiveness of cell culture with some of the spatial and molecular complexity of tissue.[159] Despite the advantages associated with using 3D-models for preclinical drug screening, well-established biochemical and proteomic assays that are used in monolayer culture and tissue samples cannot easily be employed in 3D-culture systems. However, some analytical tools can be adapted to spheroid culture.[128,160]

1.5.2 Tools for spheroid characterisation

It is recommended to not blindly apply monolayer-based assays on spheroid characterisation without prior validation, as many of these assays have previously failed in multicellular spheroids.[161] Attempts have been made to selectively dissociate and characterise single cells from spheroids,[162] however, such experimental practices are labour-intensive, and may result in artificial cell loss. Optimisation of cytotoxicity, morphology and proteomic profiling assays is, therefore, a crucial step in the characterisation of multicellular spheroids.[128]

1.5.2.1 Cytotoxicity assays

Basic and complex analytical endpoints have been used to assess the effects of compounds on spheroids and monolayer cultured cells.[128] Spheroid volume,[128-129] spheroid integrity,[129] acid phosphatase (APH) activity[128-129] and resazurin conversion[129] have been shown to provide high predictive power of response of spheroids to drug exposure.

Spheroid volume measurement and morphological assessment have been used extensively from the inception of multicellular spheroid research.[143,163] The

development of high-throughput platforms for spheroid generation such as the liquid overlay technique introduced a need for incorporation of automated spheroid-size analysis software. Computational prototype analysis modules have recently been developed, allowing for automated analysis of various characteristics of spheroids such as volume,[164-165] aggregation,[166] nuclei-count,[167] and spaciotemporal invasion dynamics.[168] Many of these programs require advanced analytical tools which may not be accessible to some research laboratories, and this could hamper the widespread adoption of 3D *in vitro* cell culture models.[164] This challenge is abrogated in an algorithm for automated spheroid size measurement written by Delyan Ivanov,[129] as it is relatively simple to use and runs on the freely-available ImageJ Fiji[169] bioimaging analysis platform. SpheroidSizer is an equally user-friendly, open-source, MATLAB-based computational platform for precise measurement of spheroid volume.[165]

Conversion of blue resazurin (non-florescent) to red resofurin (fluorescent) by metabolically active cells is principally used to elucidate the viability and biotoxicological response of cells to novel therapeutic entities.[170] Resazurin is not toxic to cells and can, therefore, be multiplexed with other assays.[129] Despite the successful validation of the resazurin assay for use in a multicellular spheroid model,[129] vast limitations preclude its implementation on 3D-culture bioanalysis. For precise quantification, resazurin and the resofurin metabolic product should diffuse in and out of the spheroid, respectively,[164] this diffusion is limited in compact spheroids, resulting in reduced reliability of the assay. Additionally, some antineoplastic compounds are known to induce an increase in cellular metabolic activity at cytotoxic concentrations, leading to misinterpretation of drug sensitivity.[171] Due to these limitations, the resazurin conversion assay should, therefore, be used as a last resort when more robust platforms like the APH assay are unavailable.

Quantification of cytosolic APH activity is used as a basis for the APH assay. Intracellular APH enzymes dephosphorylate the colourless *p*-nitrophenol phosphate to a yellow *p*-nitrophenol product, which can be spectrophotometrically measured at a wavelength of 400 nm (reference: 630 nm).[172] In addition to the established use in monolayer cytotoxicity evaluation,[172] the APH assay has been found to be linear over a wide range of cell numbers in multicellular spheroid cultures.[161] The APH assay

involves disintegration of the multicellular spheroid and, therefore the penetration challenge associated with the resazurin assay is circumvented.[164]

1.5.2.2 Measuring hypoxia in multicellular spheroids

Metabolism of 2-nitropimodazole to a metabolite that is amenable to immunohistochemical detection has been historically used to evaluate hypoxia in spheroids.[173] The compound has been commercialized as Hypoxyprobe-1™, and it demonstrated a good spatial resolution of hypoxia in multicellular spheroids.[174] However, the technique distinguishes hypoxic cells at a limited threshold, and can only be used in fixed sections.

Cell-permeable probes have recently been synthesized to improve the efficiency and sensitivity of hypoxia detection in spheroids. A click-assembled, O_2-sensing nanoconjugate allows for deep optimum imaging of hypoxia in intact spheroids using near-infrared confocal microscopy.[175] Additionally, cell permeable conjugates of platinum have been applied to high-resolution phosphorescence imaging of multicellular spheroids, with no cytotoxic effect at concentrations ≤10 μM.[176] Other iridium-based conjugates have also been made commercially available as the Image-iT® hypoxia probe.[177]

1.5.2.3 Microscopic analysis of multicellular spheroids

Standard phase contrast microscopy is used to assess the general morphology of multicellular spheroids.[128] The main drawback, however, is that it fails to reveal the structural features and position of cells inside the spheroids. Routine sectioning and histological staining can be performed to visualize the different spheroid zones.[178] However, fixing and staining introduces a lot of experimental artefacts, and histological stains generally have a low spatial resolution.[174]

Scanning electron microscopy can be used to visualize the surface features,[179] while transmission electron microscopy allows for higher resolution imaging of the cells to enable visualization of cell-cell and cell-ECM interactions in spheroids.[180] Other advanced microscopy techniques have been adopted for spheroid imaging, each with its advantages and disadvantages,[174] allowing for procurement of better spatially resolved images. One such technique is confocal microscopy, which can be used to characterise the cytoskeletal and *in situ* protein expression of spheroids. Confocal

microscopy achieves a resolution in the z-level that allows for the imaging of multiple cell layers when performed in combination with optical clearing techniques.[181] Using tissue clearing removes lipids from the sample which hinder laser light penetration and diffuse emission enhancing the ability to image spheroid interiors.[182]

Various techniques can be used for the optical clearing of multicellular spheroids. An ideal clearing protocol should allow for deep imaging into the spheroid core, result in minimal sample changes, be minimally complex and be compatible with standard confocal microscopy. The Clear^{T2} originally developed in 2013[183] possesses these attributes, and it has been shown to be superior in optimal clearing of spheroids compared to other techniques, as it maintains spheroid size and allows for the visualization of the spatial distribution of antibody-stained proteins across the spheroids.[184] Advancements have been conducted to improve the Clear^{T2} protocol for imaging 3D cultures, and it has recently been shown that optimization of the molecular weight of the polyethylene glycol (PEG) component of the clearing agent enhances the confocal imaging of MCTS.[185]

Imaging modalities such as confocal microscopy rely on detection of fluorescent or radiolabelled moieties; detection of molecules without fluorescence or radiolabels, therefore, becomes a challenge.[139] Furthermore, these imaging methods suffer from millimeter spatial resolution,[186] fail to provide the overall proteomic information of the sample, and rely on identification of known proteins.[174] Use of mass spectrophotometry imaging (MSI) circumvents the challenges associated with traditional imaging methods and examines the distribution of classes of molecules in an unbiased fashion.[159] Matrix-assisted laser desorption ionization mass spectrometry imaging (MALDI-MSI) is one such technique that can be used for spatial proteomic imaging of multicellular spheroids.[187] Traditionally, MALDI-MSI has been used for analysis of animal samples in drug development,[188] and as a diagnostic tool in various types of cancer.[189] Application of MALDI-MSI to 3D-cell culture has garnered attention over the past few years,[174,190-191] and can prove powerful in the elucidation of proteomic and metabolomic changes associated with spheroid zonal differentiation. Despite the value of mass MALDI-MSI in providing spatially resolved proteomic profiles of tumour spheroids, sample preparation is complicated by the small size of spheroids, and this hinders the adoption of the technique in 3D spheroids.[159]

1.6 Study rationale

Use of poorly characterised cell lines hampers the recapitulation of human disease in the monolayer models currently used.[108] The situation is worse in 3D-culture, as the spheroidal model system is not as widely used. While advances in medical sciences and healthcare have allowed for early diagnosis and prevention of disease progression into a metastatic state, several molecular mechanisms that underlie the aggressiveness and chemoresistance of breast cancer remain elusive.[192] Characterisation of an *in vitro* spheroid model of TNBC can provide a platform for the elucidation of various molecular cues contributing to the chemoresistance of breast cancer. Even though traditional imaging techniques like phase contrast microscopy and biochemical methods like the APH assay can be used to characterise spheroids,[128] they do not fully reveal the original biology of cell within spheroids. Optical tissue clearing, coupled with confocal microscopy is an approach that has recently emerged and that can be used to study the spatial distribution of proteins across multicellular spheroids, with minimal sample disruption.[184] In this study traditional methods were therefore used to characterise the growth parameters of BT-20 TNBC spheroids. Furthermore, optical clearing was combined with immunostaining as proof of principle.

1.7 Aim and objectives

1.7.1 Aim

This aim of the study was to develop and characterise a spheroid model of BT-20 TNBC cells with regards to growth, zonal differentiation, and drug sensitivity.

1.7.2 Objectives

The objectives of the study were to:

- Establish a multicellular spheroid model of the BT-20 cell line using both the liquid overlay and hanging drop techniques to select the most appropriate culture mechanism.
- Determine growth and maturity characteristics of spheroids over ten days with regards to:
    - Morphology and size using phase contrast microscopy;
    - Protein content using the bicinchoninic acid assay;
    - Live/dead status using the FDA/PI assay;
    - Spheroid morphology using haematoxylin-eosin staining;
    - Hypoxic status using the Image-iT® hypoxia probe.
- Determine the cytotoxic range of doxorubicin in a 2D-model using the sulphorodamine B assay
- Determine the effect of toxic and sub-toxic concentration of doxorubicin in the 3D model:
    - Acid phosphatase activity using the acid phosphatase assay;
    - Morphology, size, and volume using phase contrast microscopy;
    - E-cadherin and Ki-67 expression using immunostaining, clearing, and confocal microscopy.

1.7.3 Project overview

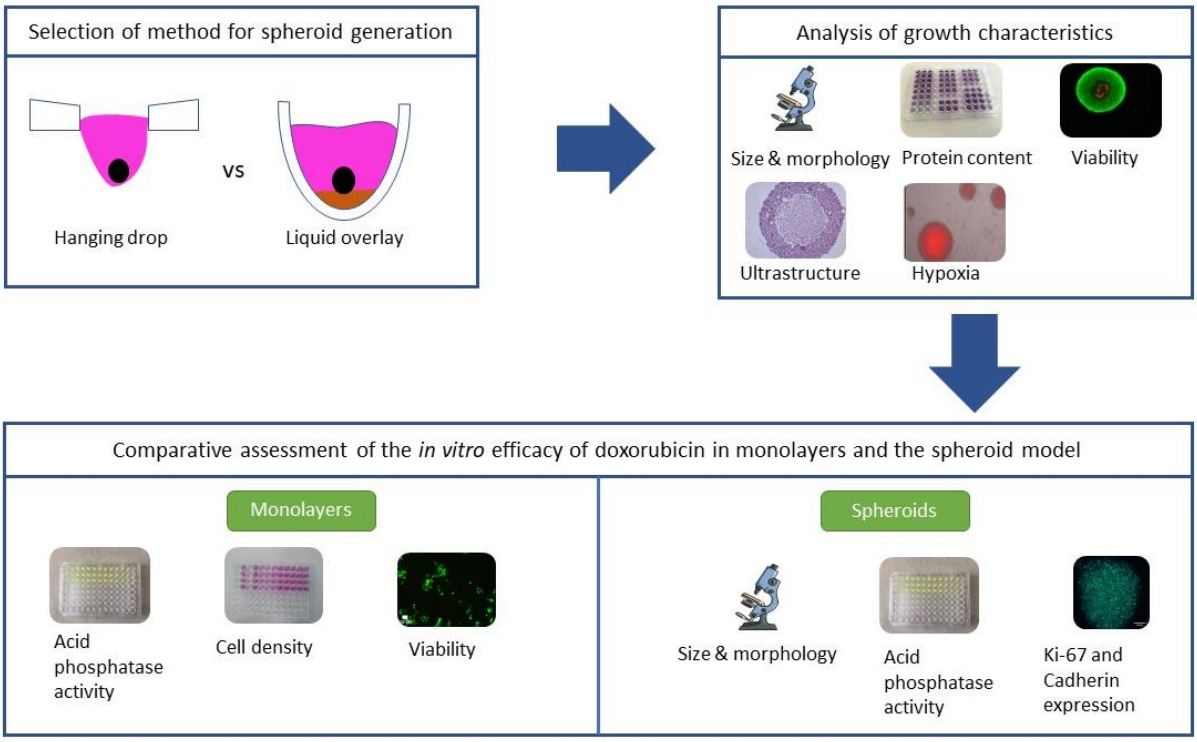

Figure 1.11: *Overview of the project*

Chapter 2: Methods

2.1 Growth and maintenance of the BT-20 cell line

The TNBC BT-20 (ATCC® HTB-19™) cell line gifted by Dr. Iman van den Bout was grown in a mixture (1:1) of Dulbecco's modified essential medium (DMEM) and Ham's-F12 medium (Gibco-Life Technologies). The medium was supplemented with 10% heat-inactivated foetal bovine serum (FBS; Gibco-Life Technologies) and 1% penicillin-streptomycin (Gibco-Life Technologies), and the cells were grown in Corning® 75 cm^2 cell culture flasks. The flasks were placed in an HF 212 UV incubator (Heal Force®, Shanghai, China), with conditions set at 5% carbon dioxide (CO_2) and 37°C in a humidified environment. Cells were grown to an approximate confluence of 80%, after which they were rinsed twice with 2 mL of 0.1 M phosphate-buffered saline (PBS). The cells were detached using 1 mL of 0.25% trypsin-ethylenediaminetetraacetic acid (Gibco-Life Technologies) for 6 min. Cells were collected and centrifuged at 200 *g* for 5 min, counted using the trypan blue exclusion assay (0.1% w/v) and diluted to either 5×10^5 cells/mL (for monolayer and liquid overlay techniques) or 1.1×10^6 cells/mL in complete culture medium as described above (for the hanging drop spheroid assay).

2.2 Selection of the most suitable method for spheroid generation

2.2.1 Hanging drop method

In the simplest form of the hanging-drop technique, a drop of cells is suspended on a lid of a petri dish and inverted to form a hanging droplet.[193] Due to gravity, the cells aggregate at the bottom centre of the hanging droplet and homotypic cellular interactions promote the assembling of individual cells into a multicellular spheroid. Multiwell hanging drop plates (Figure 2.1) have been developed to increase efficiency, uniformity, and applicability to high-throughput drug screening.[194] Despite being associated with tedious media exchange, the hanging drop method allows for easy handling and downstream proteomic assessment of generated spheroids.[139]

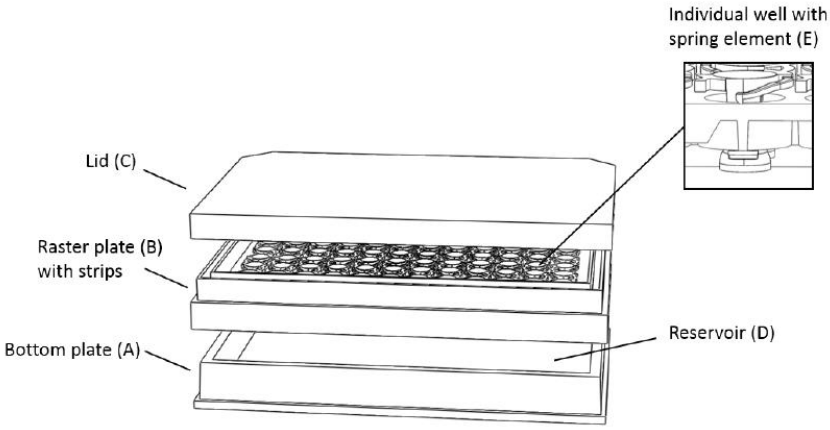

Figure 2.1: *Outline of the 96-well plate hanging drop spheroid array. Reproduced with permission from InSphero.*

Perfecta3D® 96-well plates (Sigma Aldrich, St Louis, USA) were used to generate spheroids via the hanging drop technique.[194] A cell suspension (45 µL, 5 × 10^4 cells/ well) in complete media was slowly pipetted into the aperture of the hanging drop plates, and allowed to assemble into a single multicellular spheroid over four days in each well. To minimize evaporation of media, the plate reservoir was filled with 3.5 mL autoclaved water.

2.2.2 Liquid overlay method

The liquid overlay method uses either in-house prepared poly-hydroxyethyl methacrylate[195] or agarose-coated culture plates or commercially available ultra-low attachment plates to prevent cells from growing as monolayers.[129] As cells cannot attach to the substrate surface due to a lack of attachment forces, the adhesive forces between cells dominate, and the cells migrate towards each other and aggregate into spheroids, where sustained cell proliferation results in an increase of spheroid size.[122]

To generate spheroids using the liquid overlay method, the protocol described by Friedrich *et al.*[128] was followed. Agarose (1% w/v) was prepared in FBS-free HAMS: F12 medium and solubilised by sterilization at 120°C for 30 min in an autoclave and stored at 4°C. Prior to seeding of cells, agarose was liquefied by briefly heating in a microwave. Corning® 96-well plates were then pre-treated with 50 µL agarose to create a low-attachment surface. The plates were cooled down to room temperature in a sterile environment until the agarose in the wells solidified. Cells (100 µL, 5 × 10^4 cells/well) were seeded into the agarose-coated microtiter plate, and an additional 100

µL medium (10% FBS) added. Plates were incubated for ten days. After the first four days, medium (100 µL, 10% FBS) was replaced every two to three days.

2.2.3 Monitoring of spheroid formation using phase contrast microscopy

Phase contrast microscopy was used to observe the gross morphology of the spheroids formed using the liquid overlay and hanging drop technique. This optical microscopy technique involves conversion of phase shifts of light passing through a transparent sample into differences in intensity of the image, allowing for the visualization of transparent objects.[196] Four days after seeding, spheroid formation on the hanging drop and liquid overlay techniques was observed using a Zeiss Axiovert 200 M inverted microscope (Carl Zeiss Inc, Oberkochen, Germany), using a 5X objective lens.

2.3 Evaluation of growth characteristics of spheroids

2.3.1 Morphological characterisation of spheroids using phase contrast microscopy

To determine spheroid growth, images of all spheroids were taken at Days 4, 7 and 10 using a Zeiss Axiovert 200 M inverted microscope (Carl Zeiss Inc, Oberkochen, Germany) with a 5X objective. SpheroidSizer[165] and a slightly modified ImageJ-based, automated spheroid size measurement algorithm[129] were used to calculate the volume and diameter of the spheroids.

SpheroidSizer is an automated, MATLAB-based open-source application that measures the volume of tumour spheroids. By using the active contour algorithm[197], length (L) and width (W) of the spheroid is determined, which is used to calculate the spheroid volume ($V = 0.5 \times L \times W^2$).[198]

An ImageJ macro encoded by Ivanov et al.,[129] as well as manual measurements with the Carl Zeiss AxioVision microscopy software were used to compare the spheroid volume measured using SpheroidSizer. The ImageJ macro automatically detects spheroids from whole folders containing phase contrast JPEG images and converts the pictures to black and white photos using the Yen thresholding algorithm. The algorithm then excludes artefacts from the images, fills in extra holes, and separates the spheroids from extracellular debris. The macro then proceeds to calculate the

area, minimum and maximum ferret diameter of spheroids. The 2D-projected area of the image is then used to calculate spheroid volume.[129]

With assistance from Dr. D Ivanov (University of Nottingham, United Kingdom), line 6 of the code was edited to 0.7778 pixels per µm in order to match the scaling of the microscope used, and line 11 was changed to using Li thresholding, as the Yen method could not distinguish the background of the spheroids.

The circularity index is an indicator of the degree of circularity of particles and was measured with the ImageJ plugin using the formula:

$$circularity = 4\pi \left(\frac{area}{perimeter^2}\right)$$

A circularity index of 1.0 represents a perfect circle, and when the index approaches 0.0, the particle assumes the shape of an elongated polygon.[169] ImageJ was used to measure the circularity index of the spheroids.

The percentage change in the volume of spheroids was calculated by dividing the difference in the average volume between different days by the average of volume on an earlier day. For example, the change in the percentage in spheroid volume between Day 4 and Day 7 was calculated using the formula:

$$Percentage\ change\ in\ spheroid\ volume = \frac{Volume\ on\ Day\ 7 - Volume\ on\ Day\ 4}{Volume\ on\ Day\ 4} \times 100$$

2.3.2 Change in protein content using the bicinchoninic acid assay

To monitor the increase in cellular growth, the change in the amount of protein content per spheroid was measured using the bicinchoninic acid (BCA) assay. The BCA compound is stable and forms a purple-coloured complex with cuprous ions (Cu^+) in an alkaline environment, which is used to analytically monitor Cu^+ ions produced in the reaction of proteins with alkaline Cu^{2+}. The colour produced in this reaction is stable, and its intensity increases in proportion to increasing protein concentrations.[199] This assay has minimal interferences from detergents and media additives.

The protein content of spheroids (Day 4, 7 and 10) was determined using the BCA assay.[199] Eight spheroids were pooled together and washed twice with 100 µL of 0.1 M PBS at 200 *g* for 5 min in a 1.5 mL centrifuge tube. The spheroids were then lysed using a 100 µL radioimmunoprecipitation assay (RIPA) buffer (50 mM Tris-hydrochloride [pH 7.4], 150 mM sodium chloride, 1% Triton X-100, 1% sodium deoxycholate, 0.1% w/v sodium dodecyl sulfate, 1 mM EDTA and 0.02% w/v Roche cOmplete™ protease inhibitor cocktail). To achieve complete lysis, spheroids were vortex mixed, sonicated in ice for 5 min, and centrifuged for 10 min at 16,000 *g* and the supernatant lysate was collected and stored at -80°C until analysis. Into a clear, flat-bottom 96-well plate was added 5 µL bovine serum albumin (BSA) standards (0.1, 0.2, 0.25, 0.5, 1.0, 1.5 and 2 mg/mL, prepared in PBS) or spheroid lysate. The BCA working solution was prepared by combining Reagent B, (4% w/v copper II sulphate pentahydrate) and Reagent A (1% w/v BCA disodium hydrate, 0.9% sodium bicarbonate, 2% w/v sodium carbonate, 0.16% w/v sodium tartrate [pH 11.25]) at a volumetric ratio of 1:50, and 195 µL of this BCA solution was added to the 5 µL of BSA or lysate samples in the plate. The plate was shaken for 10 min at room temperature and incubated at 60°C for 30 min. The plate was cooled to room temperature, and the absorbance measured with a ELX800UV microplate reader (BioTek instruments Inc, Highland Park, USA) using a 570 nm flitter with a 10 nm band width. Lysate protein content (mg/mL) was interpolated from the BSA standard curve, and dilutions considered to determine individual spheroid content (µg/spheroid). The percentage change in the protein content was then calculated by dividing the difference in the average protein content between different days by the protein content on an earlier day. For example, the change in the percentage of protein content between Day 4 and Day 7 was calculated using the formula:

$$Percentage\ change\ in\ protein\ content = \frac{Protein\ (Day\ 7) - Protein\ (Day\ 4)}{Protein\ (Day\ 4)} \times 100$$

2.3.3 Live/dead status using the FDA/PI staining protocol

Live/dead staining[200] was conducted to elucidate the viability of the spheroids. Fluorescein diacetate (FDA) stains metabolically viable cells (green fluorescence), and propidium iodide (PI) stains membrane-compromised cells (red fluorescence).

Spheroids were harvested, washed three times with 0.1 M PBS, and transferred to a Corning® 24-well plate. Spheroids were stained for 4 min in the dark using a staining solution (1 mL) consisting of 4 µg/mL PI and 5 µg/mL FDA in PBS. The excess staining solution was removed by washing with 1 mL PBS three times (1 min), and the spheroids were immediately visualized with a Zeiss Axiovert 200 M inverted microscope (Carl Zeiss Inc, Oberkochen, Germany) with filter sets for Texas red (PI) and fluorescein isothiocyanate (FDA) fluorescence, and a 5X objective lens. ImageJ was used to create a composite of images taken under the different filters.

2.3.4 Histological analysis using haematoxylin-eosin staining

Haematoxylin-eosin (H&E) staining was done to investigate the histomorphological changes of the 3D-cultured cells over the growth period. This combination of dyes is commonly used to stain the fine structures of cells and tissue.[201] The deep blue-purple haematoxylin dye stains basophilic components of cells like the nucleus, rough endoplasmic reticulum, and ribosomes, while the pink eosin dye stains proteins non-specifically.[201] Paraffin embedding and microtoming were compared to gelatin embedding and cryosectioning, to select the most appropriate method for histological assessment of the 3D-cultured BT-20 cells.

For paraffin embedding and subsequent microtoming, spheroids were harvested and fixed in 4% v/v formalin in 0.1 M PBS overnight. The fixing solution was removed with three PBS wash steps (10 min each). Ethanol (50% for 10 min, 70% for 30 min, 90% for 30 min, and 100% overnight) was used for dehydration. Addition of xylene in 50% ethanol (15 min), and absolute xylene (1 h) followed dehydration. Spheroids were impregnated with paraffin wax (30% in xylene for 30 min, 70% in xylene for 30 min, and 100% for 1 h) at 60°C. The samples were cooled, embedded in paraffin blocks, and sectioned into 5 µm sections using a Leica RM2255 microtome (Lecia Microsystems, Wetzlar, Germany) and mounted on microscope slides. The sections were deparaffinized with xylene (two times for 5 min). Deparaffinized sections were rehydrated with distilled water for 1 min. The slides were stained with haematoxylin (0.1% w/v for 10 min), rinsed with Scott's buffer for 10 min, dipped in eosin (2% w/v) for 2 min, and rinsed with distilled water for 1 min. Sections were dehydrated and mounted between a microscope slide and cover slide using a xylene-based mounting media. The mounted sections were observed under a Zeiss Axiovert 200 M inverted

microscope (Carl Zeiss Inc, Oberkochen, Germany) at 10X and 40X objective magnification.

The procedure described by Wheatcraft *et al.,*[159] was followed before the histological analysis of gelatin-embedded and cryosectioned spheroids. Warm gelatin (1 mL, 75 mg/mL) prepared in high purity water (18 Ω) was added to each well of a Corning® 24-well flat-bottomed plate. Spheroids were harvested, stained with 0.5% v/v gentian violet in PBS to enhance visibility, washed twice in PBS (5 min), and placed on the solidified gelatin layer. To embed the spheroids, 0.6 mL of the gelatin solution was added, and the embedded 3D cultures were snap frozen and stored at -80°C until analysis. The gelatin-embedded spheroids were mounted on the cryotome chuck with the optimal cutting temperature (OCT) compound, and frozen to ensure secure mounting then sliced into 15 µm sections using a Shandon E cryostat microtome (ThermoFischer Scientific, Waltham, Massachusetts, United States) at -20°C and directly placed on microscope slides. Staining with H&E was done as descibed for the parafin-embedded spheroids.

2.3.5 Hypoxic status of the spheroid using hypoxia probe staining

The Image-iT® hypoxia is an iridium-based, cell-permeable, and fluorescent probe that is used to detect hypoxic conditions within living cells. It is non-fluorescent in environments with atmospheric O_2 concentrations but fluoresces when the O_2 saturation is less than approximately 5%. The fluorescence of the probe correlates with HIF-1α activation in hypoxic environments.[177]

The manufacturer's protocol was followed with slight modification to the incubation time to assess the inherent hypoxic status of spheroids and monolayers. On Days 4, 7, and 10, 100 µL of medium from the 3D culture was replaced with 10 µM of the Image-iT® hypoxia probe (Invitrogen, California, USA), prepared in FBS-supplemented medium, to achieve a 5 µM in-well concentration of the probe. After 24 h, the fluorescence of the probe was imaged with a Zeiss Axiovert 200 M inverted microscope (Carl Zeiss Inc, Oberkochen, Germany), using a Texas red filter, at 5X objective magnification. Monolayers were allowed to attach, and after 24 h, the hypoxia staining procedure described for the 3D cultures was followed.

2.4 Evaluation of the cytotoxic range of doxorubicin on 2D culture

2.4.1 Sulforhodamine-B assay

Doxorubicin was selected as an antiproliferative agent to assess the chemosensitivity of the BT-20 monolayers and spheroids. The cytotoxic range of doxorubicin was determined on 2D-cultured cells using the sulforhodamine-B (SRB) assay with minor modifications to the protocol of Vichai and Kirtikara.[202] The SRB assay relies on the ability of the aminoxanthane dye to bind to the basic amino-acid residues in fixed cells. The dye binds under mildly acidic conditions and dissociates under basic conditions. Binding occurs in a stoichiometric manner, therefore the amount of dye extracted is equivalent to the cell protein mass.[202] In comparison to commonly used cell enumeration assays, the SRB assay has been shown to have fewer interferences with experimental compounds and greater sensitivity over a wide range of cell densities.[203]

Attached monolayer cells were exposed to 100 µL medium (negative control), saponin (1%, positive control), DMSO (0.2%, vehicle control) or half-log dilutions of 32 µM doxorubicin (in-well), prepared in FBS-free medium for 72 h. A sterility and background noise control consisted of 200 µL medium supplemented with 5% FBS. After exposure, cells were fixed with 50 µL cold trichloroacetic acid (TCA; 50% v/v) and left overnight at 4°C. On the following day, plates were washed four times with slow-running tap water via plastic tubing connected directly to a faucet then allowed to dry. An SRB solution (100 µl, 0.057% w/v in 1% acetic acid) was added to each well and allowed to stain for 30 min. Plates were rinsed with 1% v/v acetic acid to remove any unbound dye and allowed to dry. Tris-buffer (200 µl, 10 mM, pH 10.5) was added to each well. The plates were shaken on a Gemmyco VRN-200 orbital plate shaker (Gemmy Industrial Corporation, Taipei, Taiwan) for 1 h to solubilize the protein-bound dye. The optical density (OD) was measured at 540 nm (reference: 630 nm) using in an ELX800 microplate reader (BioTek instruments Inc, Highland Park, USA). All values were blank-subtracted, and the cell density (%) calculated using the formula below:

$$Cell\ density\ (\%\ relative\ to\ negative\ control) = \frac{ODsample}{Average\ ODnegative} \times 100$$

Where '*ODsample*' refers to the corrected optical density of the sample and '*ODnegative*' is the corrected optical density of the negative control.

2.4.2 Acid phosphatase assay

The APH assay[128] was used to corroborate the cytotoxic concentrations of doxorubicin on monolayer cell cultures obtained using the SRB assay. This assay assesses cell viability through quantification of cytosolic APH activity. Intracellular APH enzymes in viable cells hydrolyse *p*-nitrophenyl phosphate to *p*-nitrophenol. The absorbance of *p*-nitrophenol at 405 nm is directly proportional to the number of viable cells.[161]

The same doxorubicin exposure conditions that were used for the SRB assay were maintained for the APH assay. After 72 h exposure, cells were washed three times with 100 µL PBS (5 min), and an aliquot of 100 µL was left after the third wash step in each well. The APH assay buffer (100 µL) was added, containing para-nitrophenylphosphate (2 mg/mL) and Triton X-100 (0.1% v/v) in citrate buffer (0.1 M). Plates were incubated for 90 min at 37°C. After incubation, sodium hydroxide (1 M, 10 µL) was added to the wells, and the OD was measured within 10 min at 405 nm (reference: 630 nm) on an ELX800UV microplate reader (BioTek instruments Inc, Highland Park, USA). All values were blank-subtracted, and the APH activity (%) calculated using the formula below:

$$APH\ activity\ (\%\ relative\ to\ negative\ control) = \frac{ODsample}{Average\ ODnegative} \times 100$$

Where '*ODsample*' refers to the corrected optical density of the sample and '*ODnegative*' is the corrected optical density of the negative control.

2.5 Comparison of the efficacy of doxorubicin in the 2D and 3D model

2.5.1 Exposure procedure

Monolayer cells were allowed to attach in Corning® 96-well plates for 24 h after which the cells were exposed to 100 µL of the in-reaction IC_{25}, IC_{50}, and IC_{75} concentrations of doxorubicin (calculated using the SRB assay). Spheroids were grown for four days using the liquid overlay method outlined in Section 2.2.2, and 100 µL medium replaced with two-fold IC_{25}, IC_{50}, and IC_{75} concentrations, as well higher concentrations (6 µM, 8 µM and 10 µM in-well) due to hypothesised reduced drug sensitivity.

2.5.2 Phase contrast microscopy

After the exposure period, a Zeiss Axiovert 200 M inverted microscope (Carl Zeiss Inc, Oberkochen, Germany) was used to capture phase contrast images of the cells using a 10X objective lens for monolayers and a 5X objective lens for spheroids. SpheroidSizer was used to calculate the change in volume elicited by doxorubicin on the spheroids, using the formula:

$$Spheroid\ volume\ (\%\ relative\ to\ negative\ control) = \frac{Vsample}{Average\ Vneg} \times 100$$

Where '*Vsample*' refers to the volume of the treated sample, and '*Vneg*' refers to the volume of the negative control.

2.5.3 Monolayer viability assessment

Monolayers treated with the IC_{25}, IC_{50}, and IC_{75} of doxorubicin for 72 h were washed three times with 0.1 M PBS and stained for 4 min in the dark with 5 µg/mL FDA (200 µL). The staining solution was removed by washing with PBS three times (5 min), and the cells were visualized using a Zeiss Axiovert 200 M inverted microscope (Carl Zeiss Inc, Oberkochen, Germany) with a filter set for FDA fluorescence at 10X objective magnification.

2.5.4 APH assay

After the 72-h exposure period, the APH activity assay was conducted on monolayers as described in Section 2.4.2. Spheroids were transferred into a non-agarose-coated round bottom 96-well plate, washed three times with PBS (100 *g,* 1 min), and assayed as described for monolayer cells.

2.5.5 Tissue clearing and immunostaining of treated spheroids

The Clear^{T2} protocol[183] was used to optically clear doxorubicin-treated and immunostained spheroids prior to confocal imaging. The solvent and detergent free clearing technique involves immersion of spheroids in increasing concentrations of formamide and PEG.[185] The components of the clearing agent promote the replacement of water in cells with the aqueous solution of formamide and PEG, until an equilibrium is reached. This allows for the enhancement of the transparency and reduction of the refractive index of the sample, while hydration of the sample is

maintained. Additionally, PEG is used to maintain the stability of the fluorescently-labelled proteins, and to reduce fluorescence quenching caused by formamide.[185]

Prior to clearing, the Ki-67 monoclonal antibody (mAB) and the anti-pan cadherin polyclonal antibody (pAB) were used to immunofluorescently stain doxorubicin-treated spheroids. The antigen Ki-67 is a nuclear protein that is expressed in proliferating vertebrate cells. In cultured cells, the levels of this protein are highest in the G_2 and mitosis phase[204] of the cell cycle and is, therefore, commonly used as a marker for proliferation or absence thereof. The anti-pan cadherin pAb is broadly cross-reactive with all members of the cadherin family: N-cadherin, E-cadherin, P-cadherin, and R-cadherin. Classic cadherins play a role in homophilic cellular adhesion interactions, and E-cadherin is responsible for mediating cell-cell interactions within multicellular spheroids.[205] The 4',6-diamidino-2-phenylindole (DAPI) dye was used as a counterstain for nuclei, as it forms a fluorescent complex by binding to adenine-thymine rich regions of DNA.[206]

Spheroids treated with the IC_{25}, IC_{50}, IC_{75}, and 10 µM of doxorubicin for 72 h were collected into 1.5 mL centrifuge tubes and washed with PBS three times (5 min). After washing, the spheroids were fixed in 4% formaldehyde and stored at 4°C until further assessment. All subsequent steps were conducted at room temperature on an orbital shaker at 90 revolutions per min (rpm). Permeabilization and blockage of non-specific staining was achieved by immersing the spheroids in 1% Triton X-100, 10% normal foetal calf serum, and 4% BSA in PBS (B-PBT) for 2 h. The spheroids were incubated overnight in 1 µg/mL of the Alexa Fluor® 488 conjugated anti-Ki 67 mAb (Abcam, Cambridge, United Kingdom) and in 1:1000 of the anti-pan cadherin pAb (Abcam, Cambridge, United Kingdom) diluted in B-PBT. The spheroids were then washed twice in 0.2% Triton X 100 in PBS (0.2% PBT) for 2 h, and one 2h wash in B-PBT. The Goat Texas Red anti-mouse secondary (Abcam, Cambridge, United Kingdom) antibody was added at a concentration of 1:300 in PBT overnight. The spheroids were washed twice in B-PBT (2 h) and stained with 1 µg/mL DAPI in B-PBT for 1h. Samples were then returned to PBS for clearing. For clearing, PBS was removed and replaced with, 25% formamide/10% PEG in PBS for 10 min, and subsequently 50% formamide/20% PEG in PBS for 30 min. The 50% formamide/20% PEG solution was replenished until the samples were opaque. Fluorescent images of cleared spheroids were acquired using a Zeiss Laser Scanning Microscope LSM800 (Carl Zeiss Inc, Oberkochen,

Germany), using a 20X air objective lens. The laser power was kept constant during acquisition. A 488-nm argon laser was used to visualize Ki-67, a 561 nm diode laser was used to visualize cadherin bound secondary antibody and a 405 nm diode laser was used to visualize DAPI. The imageJ Fiji package[169] with the Bio-Formats importer plugin was used to analyse the images generated from the different filters, and to create composites of images.

2.6 Statistics

Raw data was captured using Microsoft Excel (Microsoft) and statistical analyses performed with GraphPad Prism 8.0.2 (GraphPad Software, San Diego California USA). At least three biological repeats were conducted per experiment, with four technical repeats for monolayer studies, and at least six representative spheroids per experimental condition. All data are expressed as mean and standard error of the mean (SEM). Changes in spheroid protein content and volume over the culturing period was calculated using a Kruskal-Wallis analysis of variance (ANOVA) test with a Dunn's multiple-comparison post-test. For monolayer cytotoxicity studies, the logarithmic drug concentration was plotted against the response (compared to the negative control), and the IC_{25}, IC_{50}, and IC_{75} of doxorubicin was calculated using non-linear regression curve fit (log[inhibitor] vs response) with robust fit. Comparison of the changes in spheroid viability and volume after exposure to the different concentrations of doxorubicin was determined using a Kruskal-Wallis test with a Dunn's multiple-comparison post-test. Outliers were identified and removed using the GraphPad Robust regression and outlier removal (ROUT) method.[207]

Chapter 3: Results and discussion

3.1 Selection of spheroid generation platform

The liquid overlay and hanging-drop methods are versatile techniques that can be used for the high-throughput generation of multicellular spheroids. The main advantage of these assays are their ease of use and adaptability to high-throughput downstream biochemical assays.[131] From in-house experience: compared to loose aggregates, dense spheroids allow for minimal disaggregation and cell loss during medium exchange, and circular spheroids are better-amenable to growth evaluation relative to irregularly-shaped spheroids. The robustness of the hanging drop and liquid overlay methods in the generation of dense and reproducibly circular BT-20 spheroids was compared in a bid to select the most appropriate method for establishing a robust 3D culture technique.

Across three biological repeats, cells grown using the hanging-drop method either failed to assemble into spheroids (Figure 3.1 A), developed into loose spheroids (Figure 3.1 B) or developed into semi-dense, irregularly-shaped spheroids (Figure **3.1** C) by Day 4. The yield of these semi-dense spheroids was exceptionally low (approximately 4 per 96-well plate). In contrast, cells grown using the liquid overlay method developed into a single, dense and circularly-shaped spheroid per well on Day 4. The formation of these dense and circularly-shaped spheroids was constant through biological repeats (Figure 3.1 D-F).

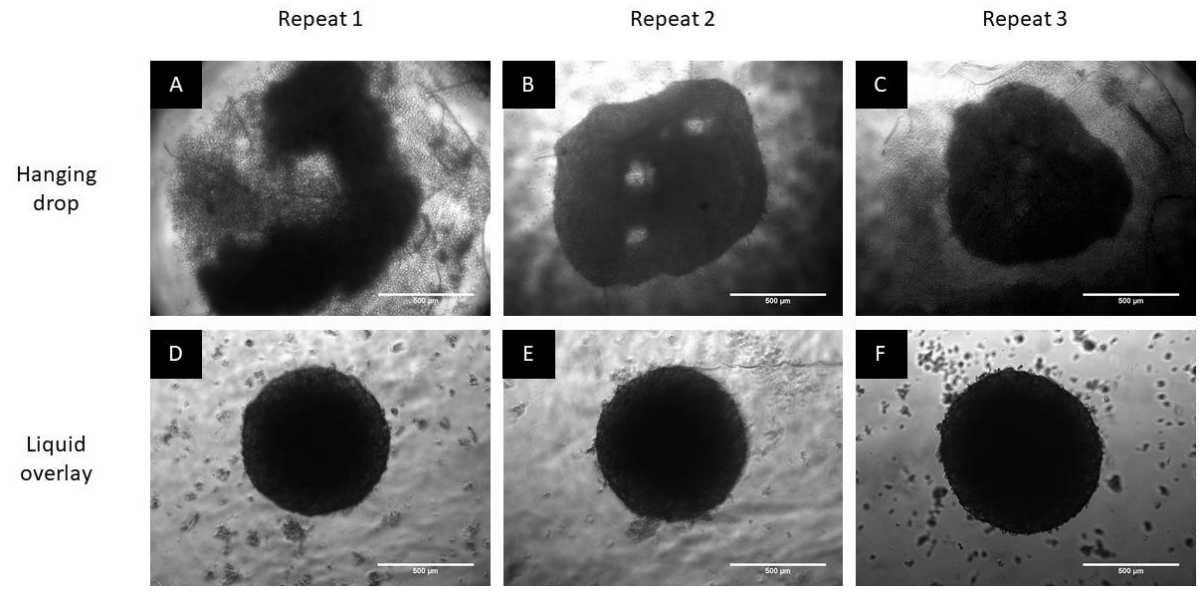

Figure 3.1: *Representative phase contrast images of spheroids grown using the hanging drop technique (A-C) and liquid overlay method (D-F). Images captured using a 5X objective lens, scale bar = 500 µm.*

The type of cell line, source and passage number of immortalized cells are inherent factors that influence spheroid formation and growth.[208] Phenotypic differences in spheroids of the same cell line grown from different cell stocks have recently been noted.[208] Additionally, the potential of cells to assemble into spheroids is largely dependent on the spheroid-generation platform used.[209] Cells propagated as spheroids using different arrays exhibit differential morphometric, diffusion, and chemosensitivity attributes.[209] The systematic comparison to evaluate various assays is, therefore, a critical step that needs to be conducted before the adoption of a specific technique for growth of spheroids of any desired cell line.[209]

The degree of successful spheroid formation in this study was lower with the hanging drop technique compared to the liquid overlay method. Various factors have been shown to play a role in the reproducibility of spheroids grown using the hanging drop technique.[208] The seeding volume influences spheroid growth, as larger medium volumes produce spheroids with greater fold-change and end-point protein content, relative to those grown in smaller volumes.[208] In the current study, a seeding volume of 45 µL was used in the hanging drop technique, whilst 200 µL was used for the liquid overlay technique. The discrepant spheroid formation capacity between the two assays can, therefore, partially be attributed to differential culture medium volumes.

In a study conducted in 2016 by Raghavan et al.[209] it was demonstrated that MCF 7 breast cancer spheroids grown using the hanging drop method were more viable and more compacted compared to those generated from the liquid overlay method, a contradictory observation from that obtained in the current study. This discrepancy can be explained by the difference in seeding densities used in the two studies. While Raghavan et al.[209] used 500 cells per drop, in the current study 50 000 cells were used (a 100 fold difference in seeding density). The growth and nourishment of immortalized cells requires an adequate nutrient supply from the surrounding medium, and it is historically known that cells grown in larger volumes of medium have higher proliferative potential than those grown in smaller volumes.[210] This implies that nutrients may get depleted quicker at higher seeding densities, leading to a decreased yield of spheroids. The reduced yield of spheroids in the hanging drop technique could, therefore, potentially be a result of insufficient nutrient supply to the seeded cells.

In addition to nutrient depletion, reproducibility of well-established spheroids can be hampered by the rapid movement of plates in the incubator, a limitation that can be circumvented by reducing movement and plate monitoring within the first 48 h after initial seeding.[128] Relative to the liquid overlay, spheroids grown using the hanging drop technique are more susceptible to rapid motion, and consequential alteration of successful spheroid formation.

The observations obtained from the comparison of the liquid overlay and the hanging drop technique corroborate the view that; it is imperative to compare various spheroid generation assays to obtain stable characteristics, prior to any downstream experimentation.[208-209] In this study, the liquid overlay method formed reproducible dense spheroids which were subsequently used for further characterisation.

3.2 Characterisation of spheroid growth characteristics

Though multicellular spheroids have been used for *in vitro* simulation of the *in vivo* micromilieu for approximately half a century,[143] characterisation of the phenotypic properties of many of these models is not widely conducted.[211] Elucidation of various structural and functional characteristics can reveal baseline parameters that could potentially be altered by new test compounds with varied mechanisms of action. Additionally, well-characterised 3D cultures can be routinely adapted as 'spheroid controls' or standards when conducting drug screening on poorly-characterised spheroid types.[128] In an attempt to characterise the BT-20 multicellular spheroids generated using the selected liquid overlay technique, various morphometric and biochemical parameters were evaluated during the ten-day growth period.

3.2.1 Gross morphology of the multicellular spheroids

By Day 4, the spheroids had a circular structure, which was maintained up to Day 10 (Figure 3.2 A-C). The circularity index for 49 randomly selected Day 4 spheroids was 0.87 ± 0.01 (Figure 3.3). The spheroids were reproducibly circular, suggesting that across different biological repeats, the 3D cultures were susceptible to similar depth penetration of nutrients and compounds.

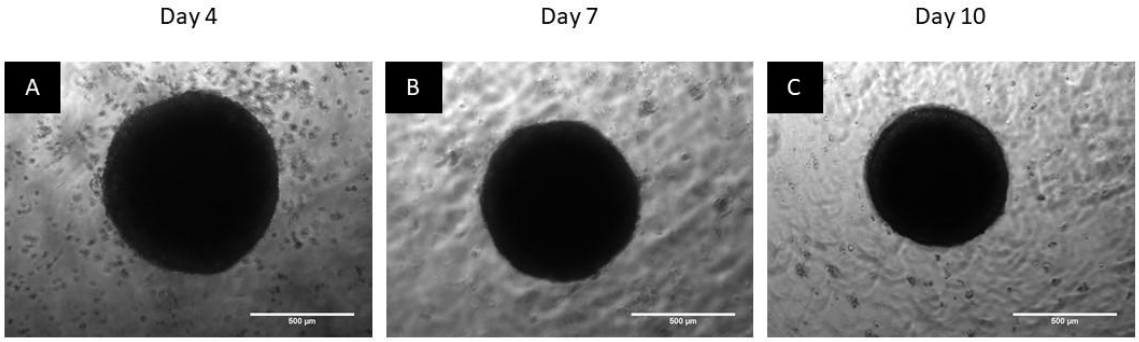

Figure 3.2: *Representative phase contrast images of spheroids grown using the liquid overlay method on Day 4 (A), Day 7 (B) and Day 10 (C). Images captured using a 5X objective lens, scale bar = 500 µm.*

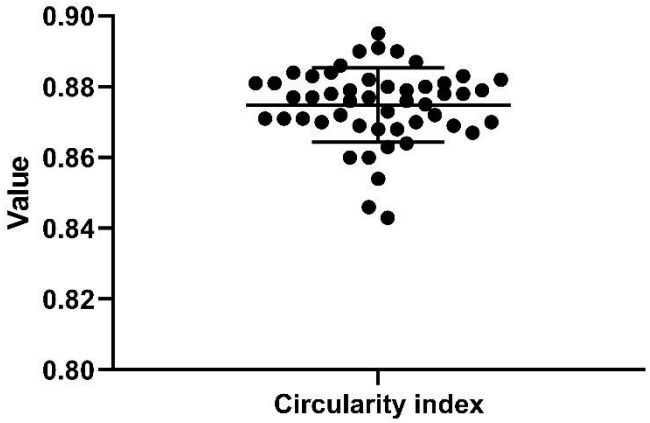

Figure 3.3: *The circularity index of randomly selected Day 4 spheroids. N = 49 randomly spheroids from 4 biological repeats, with at least 6 technical repeats per experiment.*

In studies describing various 3D cellular clusters, the term 'spheroid' is widely used.[208] Generalised use of this term does not reflect the gross structural heterogeneity of spheroids generated from different cell lines and is sometimes unjustifiably used to describe loose cellular aggregates which easily disassemble during handling.[212] Large-scale profiling of a wide panel of breast cancer cells cultured in 3D format has led to the identification of four main morphological classes of spheroids morphology namely; round, mass, grape-like and stellate (Figure 3.4).[213]

Spheroids that are clustered under one morphological class have similar patterns of gene expression,[213] and therefore, characterisation of spheroid morphology can partially provide potential clues to some of the molecular attributes of the cells. Additionally, predictions of potential drug susceptibility of spheroids can be drawn from observing the gross morphology. For example, loosely-compacted breast cancer spheroids have been shown to be more chemosensitive than tightly-compacted spheroids, potentially due to decreased drug penetration in dense spheroids.[214]

Using the morphological classification depicted in Figure 3.4, the spheroids developed in the current study could potentially be clustered under the mass or round-type spheroids. The cells in the round class have strong intercellular adhesion properties,[213] and this phenomenon is reflected by the dense architecture of the developed spheroids.

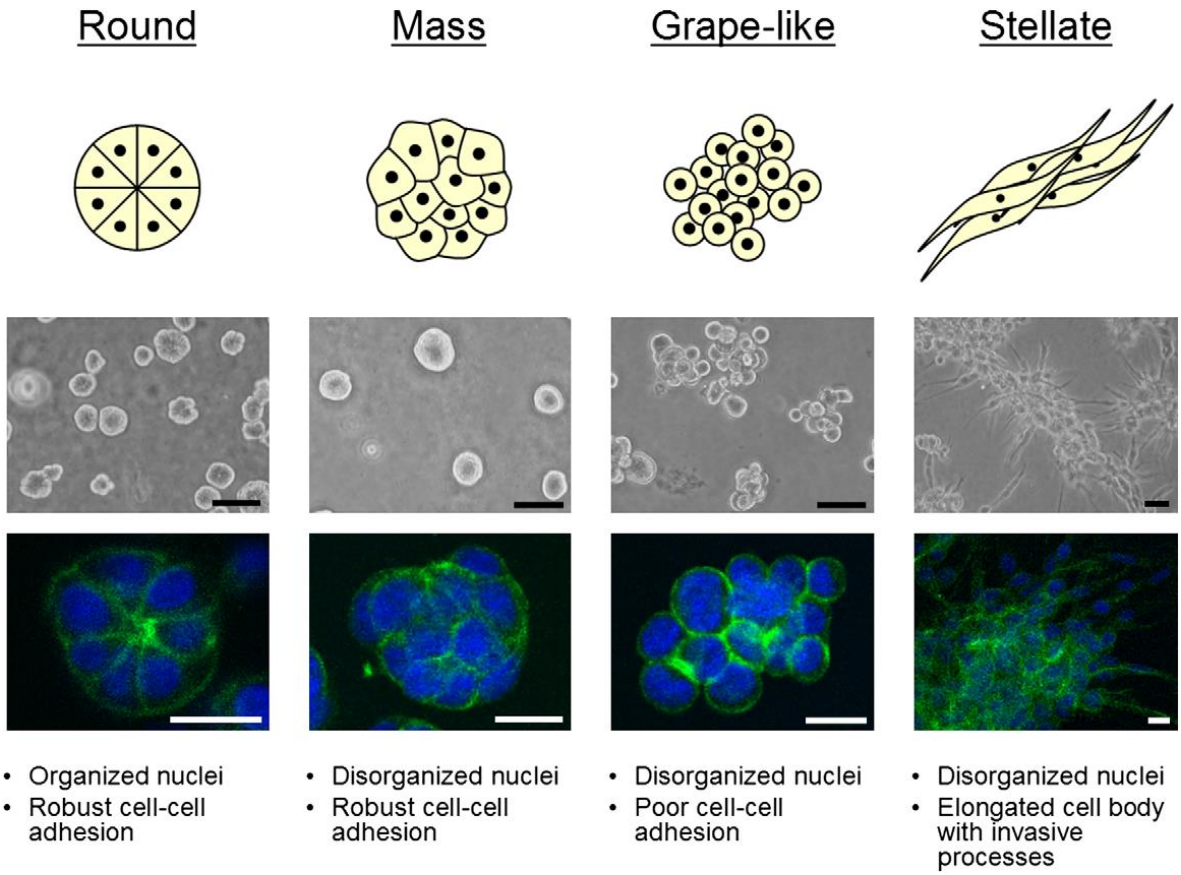

Figure 3.4: *The four distinct morphologies of breast cancer 3D cultures.[213] Figure reproduced under the Wiley Creative Commons Attribution License (CC BY).*

It is important to note, however, that not all initially seeded cells were incorporated into the compact spheroids, as a small proportion of cells remained on the periphery (white arrows on Figure 3.5). Any cellular debris or other artefacts can preclude accurate morphometric analysis of spheroids.[129] Therefore, prior to capturing images for assessment of spheroids, the medium was replenished to wash off the unattached cells surrounding the spheroids. Though it is likely that these cells are dead debris, the cells surrounding spheroids were identified and named non-spheroid forming (NSF) cells in a recent study.[215]

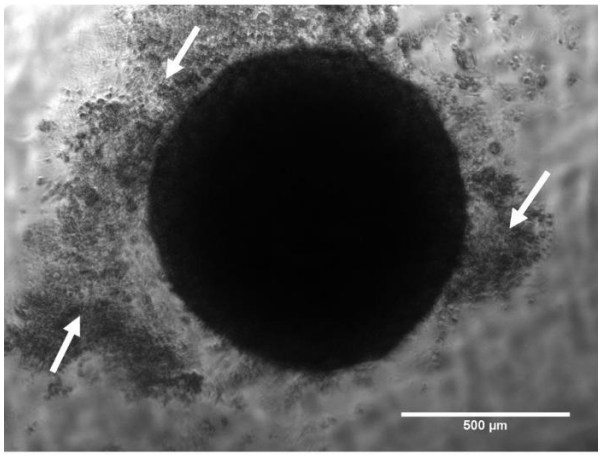

Figure 3.5: *Non-spheroid forming cells (white arrows) on the periphery of a Day 4 spheroid. Image captured using a 5X objective lens, sale bar = 500 µm.*

Upon isolation and characterisation of these NSF cells, the authors demonstrated that the cells had lost essential cell-cell adhesion molecules such as E-cadherin, and only formed loose aggregates when sub-cultured in 3D format.[215] Spheroid formation is dependent on homotypic interactions of these adhesion molecules, which are also responsible for the dynamic change in spheroid size during growth,[215] a parameter that was analysed to further characterise the BT-20 spheroids.

3.2.2 Change in spheroid size over the growth period

The use of phase contrast microscopy in the characterisation of spheroid morphology can be extended to the evaluation of spheroid size kinetics.[128] Circumscribing the perimeters of the region covered by spheroids in 2D projections of phase contrast images is used to calculate the spheroid area. Mathematical equations are then applied to calculate the spheroid volume; a robust analytical endpoint for evaluating the change in spheroid size.[129]

Many researchers use software packages that are procured with microscopy equipment to manually draw the perimeter of the spheroid. Use of such an approach in the high-throughput analysis of spheroids is impractical, as a large number of images are generated.[165] Advances in computational biology have aided in the development of automated spheroid image analysis algorithms,[164-168] thus reducing labour and speeding up the analysis process. However, many of these software packages require re-adjustment for different batches of images, and this reduces the robustness of high-throughput image analysis. SpheroidSizer[165] and an ImageJ macro[129] are relatively simple spheroids image analysis tools that circumvent this

limitation, as they require minimal adjustments. To select an appropriate tool for the evaluation of the change in the size of BT-20 spheroids, the ease of use and validity of these two software packages was compared to manual measurements.

A total of 60 Day 4 spheroids were measured using the three image analysis platforms. Representative images of correctly measured spheroids are shown in Figure 3.6 (A-C). Manual measurement of the length and width of a spheroid requires the arbitrary selection of two points that the user deems appropriate. Depending on judgement, different dimensions were recorded from the same image (Figure 3.6 D). Additionally, upon analysis of the resultant measurements from the ImageJ macro and SpheroidSizer, it was noted that some images were erroneously analysed (Figure 3.6 E and F, respectively). The incorrect measurements were excluded from all datasets and 38 spheroids were used for final comparison of the spheroid volume measured using the three modalities. There was no significant ($P > 0.05$) difference between the spheroid volume measured using manual delineation (3.9×10^8 $\mu m^3 \pm 0.1 \times 10^8$), ImageJ macro ($3.8 \times 10^8$ $\mu m^3 \pm 0.1 \times 10^8$), and SpheroidSizer ($3.7 \times 10^8$ $\mu m^3 \pm 0.1 \times 10^8$, Figure 3.7). Despite the successful validation of the image analysis platforms, each one is associated with different shortcomings and advantages.

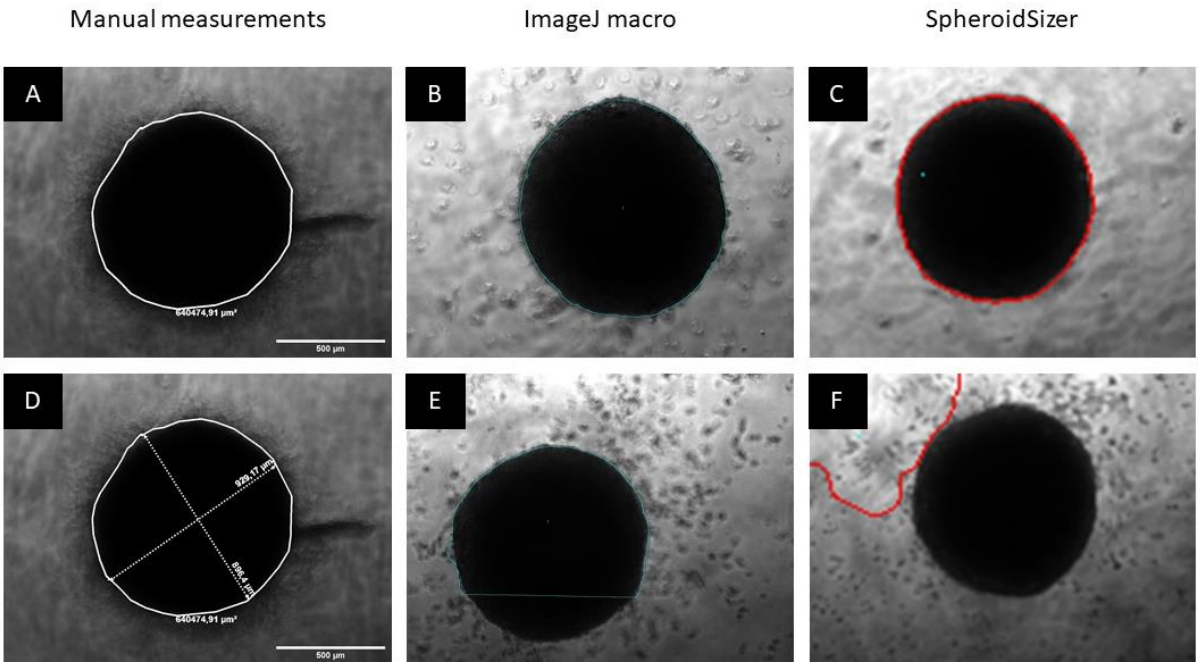

Figure 3.6: *Representative phase contrast micrographs of spheroids measured using manual measurements (A), the ImageJ macro (B) and SpheroidSizer (C). Image D shows different spheroids diameters obtained from arbitrary manual measurements, which could lead to potential error. Output images showing erroneously measured spheroids using the ImageJ macro (E), and SpheroidSizer are also shown (F). Image captured using a 5X objective magnification. Scale bar = 500 µm. Scale bars for figures B, C, E and F are not included, as these are output images from automated software, without microscope scaling.*

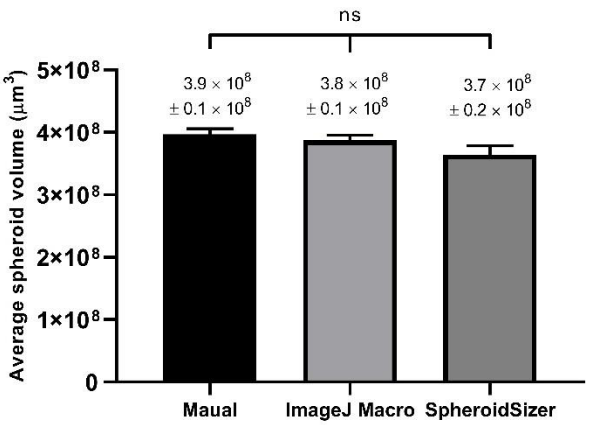

Figure 3.7: *Comparison of the average spheroid volume calculated using manual measurements, SpheroidSizer and ImageJ. One-way ANOVA, with Dunn's post-test, ns = not significant. N = 50 spheroids, from 4 biological repeats, with at least 6 technical repeats per experiment.*

When analysing a large number of images using automated analysis software, errors that are caused by thresholding artefacts are inevitable.[165] In SpheroidSizer, a tool known as "hand draw" allows the user to manually draw the outline of incorrectly

measured spheroids in the software. The software then uses the user-defined boundaries to calculate the spheroid volume, which is incorporated into the rest of the correctly-measured results, and in this way, any imperfect segmentation is salvaged.[165] On the contrary, such a feature does not exist in the ImageJ macro, and erroneously delineated spheroids need to be manually-measured using vendor-supplied microscopy software. The obtained result will have to be manually typed into data capturing software (such as Microsoft Excel) before volume calculations can be conducted, and this could be disadvantageous in high-throughput analysis.

SpheroidSizer calculates volume (V) by using the measured length and width of the spheroid using the formula: $(V = 0.5 \times L \times W^2)$. This approach is problematic as it assumes that all spheroids to be measured are perfectly circular.

This limitation is circumvented in the ImageJ macro, as it uses the projected area (S, μm^2) of the spheroid to calculate the radius: $\left(R = \sqrt{\frac{S}{\pi}}\right)$ and volume: $\left(V = \frac{4}{3}\pi R^3\right)$ in μm^3.[129] This approach is not only limited to circular spheroids as it is applicable to ellipsoids with a L:W ratio of up to 1:5.[129] An additional advantage of the imageJ macro is that it computes the circularity index of spheroids, and therefore, provides a platform for automated analysis of both spheroid size and shape.

Not considering the few associated limitations, both the software are robust and time-saving platforms that require minimal user input for the automatic measurement of the size of spheroids. The results in SpheroidSizer are exported in a 96-well plate formatted spreadsheet that is amenable for use in spheroid drug screens, however, this requires an investment of time into naming the images according to their respective position on the experimental plate. In instances where the locus of the spheroid is of no substantial importance, the ImageJ macro can be alternatively used, as no specific naming of the files is required prior to computation. Considering these convenience factors, ImageJ was chosen to analyse the change in spheroid size over ten days, while SpheroidSizer was used to analyse the alteration of spheroids volume after drug treatment.

The average spheroid volume decreased significantly ($P < 0.001$) from Day 4 ($3.9 \times 10^8\ \mu m^3 \pm 0.1 \times 10^8$) to Day 7 ($2.7 \times 10^8\ \mu m^3 \pm 0.1 \times 10^8$) and further decreased to Day 10 ($2.1\times 10^8\ \mu m^3 \pm 0.1 \times 10^8$), representing a 31% decrease in volume between Day 4 and Day 7 and a further 22% decrease between Day 7 and Day 10 (Figure 3.8 A). The average spheroid diameter also decreased significantly ($P < 0.0001$) from 901 ± 7.0 µm on Day 4 to 800 ± 6.7 µm and to 737 ± 7.1 µm on Day 10, with an 18% reduction in spheroid diameter between Day 4 and Day 10 (Figure 3.8 B). The greatest decrease in spheroid volume was, therefore, between Day 4 and Day 7, and the volume continued to decrease from Day 7 and Day 10.

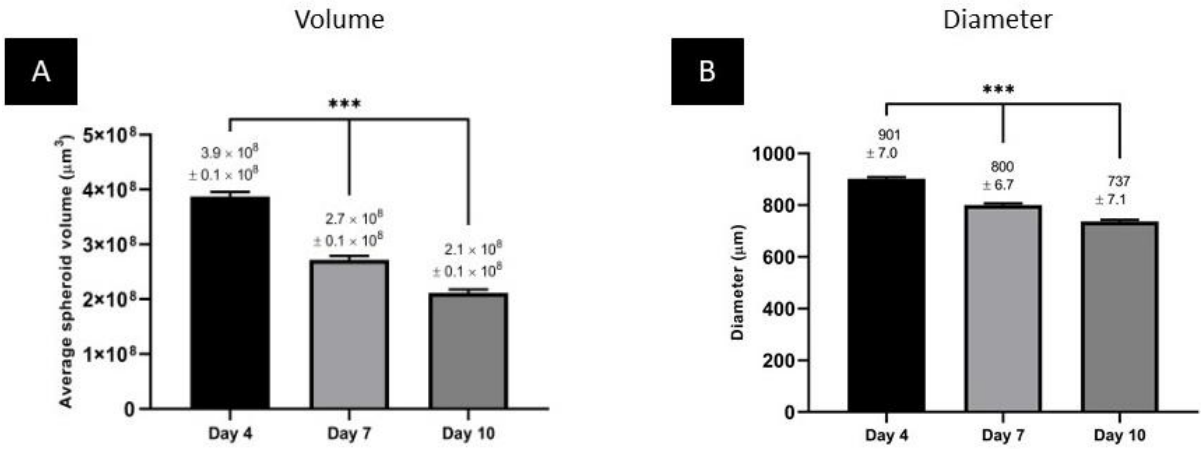

Figure 3.8: *(A) The average spheroid volume on Day 4 (N = 50 spheroids), Day 7 (N = 62 spheroids) and Day 10 (n= 35 spheroids). (B) The average spheroid diameter on Day 4 (N = 50 spheroids), Day 7 (N = 62 spheroids) and Day 10 (N = 35 spheroids) from 4 biological repeats, with at least 6 technical repeats per experiment. One-way ANOVA, with Dunn's multiple comparison post-test, *** = P ≤ 0.001.*

Spheroid compaction over time is a consequence of the establishment of strong intercellular connections.[216] Analysis of the 2D projected area of hepatoma[205] and prostate cancer[216] phase contrast images has been used to investigate the compactness of spheroids during formation. This led to the identification of three distinct phases during spheroid growth; an initial stage of rapid compaction, a delay period, and a period where there is a decline in size[205] (Figure 3.9). A further decrease in the size of spheroids on subsequent days following initial formation has recently been reported,[217] and this phenomenon is regulated by the cytoskeleton and constituents of the ECM such as cadherins and integrins.

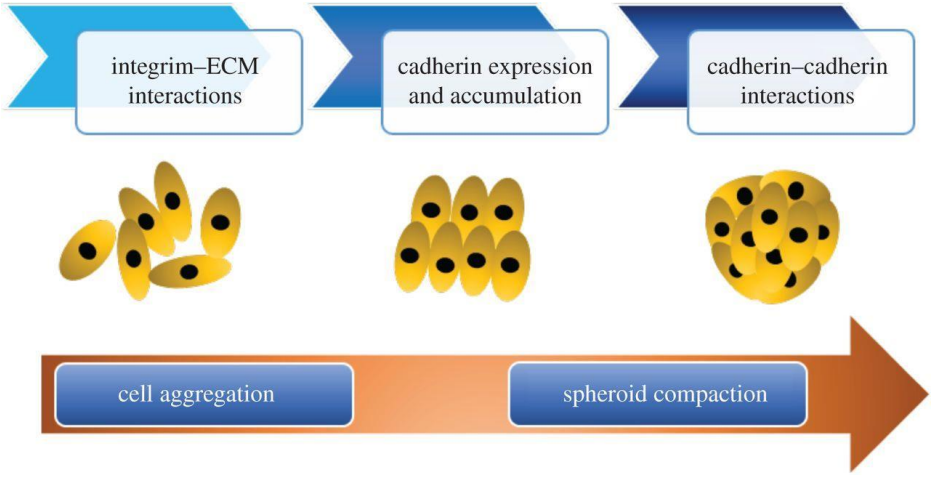

Figure 3.9: *Stages of spheroid formation.[218] Image reproduced with permission from the Royal Society, license number: 4519211100872.*

Though spheroid volume is a robust parameter that can be used to characterise spheroid growth and chemotherapeutic sensitivity, estimating the health of the spheroid exclusively based on size can be misleading due to distinct reasons. Shedding of cells on surfaces of spheroids with a diameter greater than 250 µm has been described,[219] therefore, the decrease in size could be due to cellular death rather than compaction. Secondly, the cell density across the spheroid can differ, with loosely-packed cells in the inner parts of the spheroid, and tightly packed cells on the periphery.[220] Thirdly, cells might shrink in response to stress signals, without any alteration in metabolic activity.[164] To substantiate the findings from spheroid volume assessment, it was imperative to further investigate parameters such as protein content, live/dead status and the histology of the spheroids.

3.2.3 Time-course protein content of the spheroids.

On Day 4, an average of 7.0 ± 0.48 µg of protein was measured per spheroid. The amount of protein increased by approximately 11% to 7.8 ± 0.54 µg per spheroid on Day 7. Similarly, from Day 7 to Day 10, the protein content (µg per spheroid) increased by 9% to 8.5 ± 0.73 µg (Figure 3.10). Therefore, across the 10-day growth period, the protein content per spheroid only increased by 21.4%, and the difference in the protein content across the different days was not statistically significant (P >0.05).

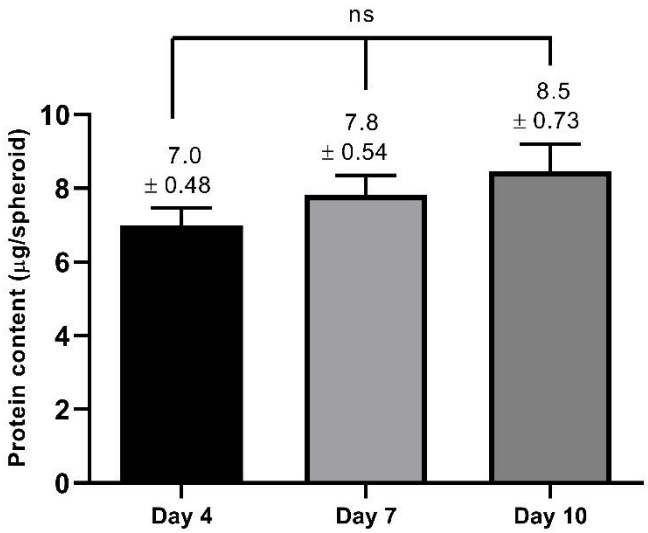

Figure 3.10: *Average protein content (µg per spheroid) of Day 4, Day 7 and Day 10 spheroids. N = 5 biological repeats. one-way ANOVA with Dunn's multiple comparison test. ns = not significant (P >0.05).*

The increase in the protein content per spheroid coupled with a decrease in size supports the speculation that the decrease in spheroid size is due to compaction rather than cell death. In addition to playing a central role in spheroid compaction, the protein E-cadherin interacts with β-catenin to promote the transcriptional activation of proteins such as cyclin D1 and c-myc.[221] These proteins facilitate the G1 to S-phase progression of cells of the cell cycle, and thus their upregulation could promote the differentiation and proliferation of cells in spheroids.[218]

Given that the doubling time of monolayer-cultured BT-20 cells is approximately 60 h,[222] if the 3D-cultured counterparts retain the same proliferative rate, at least a three-fold increase in protein content per spheroid would be expected between Day 4 and Day 10. However, the change in the protein content was lower than this, suggesting a reduction of the proliferative capacity of the BT-20 cells when grown in 3D format. Compelling evidence has shown that metabolic reprogramming in spheroids during growth is coupled with a decrease in cellular growth rates.[223] Additionally, it has been reported that viable cells are restricted to the outer 150 µm of spheroids, while cells in the inner regions either progress slowly through the cell cycle or resort to a dormancy due to O_2 and nutrient starvation.[224] The insignificant change in protein content over the growth period is, hence, potentially due to the altered cellular kinetic profile of cells across the spheroid. Although time-course protein content analysis can provide insight into the zonal differentiation of spheroids,[208] this

phenomena should be confirmed with assays that specifically reveal the viability and structural attributes of cells across the spheroids.

3.2.4 Live dead status

The hydrolysis of esters such as FDA by viable cells produces fluorochromasia; a phenomenon characterised by the appearance of bright-green fluorescence that can be easily visualised under a microscope.[225] The FDA substrate is non-polar and readily penetrates through cell membranes before it is converted to polar fluorescein by intercellular esterase enzymes in viable cells.[225] This conversion can be used as an indicator of the viability and membrane integrity of cells within multicellular spheroids. Propidium iodide is a red fluorescent, DNA intercalating and membrane impermeable compound that is used to stain membrane-compromised or dead cells.[200] The viable and dead cells within the spheroids were identified using two-colour staining with green (FDA for viable cells) and red (PI for dead cells) fluorescence.

The majority of cells within spheroids were viable after ten days of growth, as indicated by the dominance of green fluorescence after FDA staining. The fluorescence intensity of FDA was high in cells on the outer spheroid rim, gradually decreasing towards the centre, inferring decreased viability of cells in inner spheroid regions. Quiescent cells typically have reduced metabolic rates, and the decreased fluorescence in the inner regions could be a consequence of slower cleavage of the FDA moiety. The PI fluorescence was higher in cells situated in the middle region of the spheroids, compared to those towards the periphery. The staining of PI was maintained during the growth period, however, on Day 10 the dye was more dispersed compared to Day 4, suggesting an increase in the distribution of membrane-compromised cells during the growth period. Considering the merged staining patterns of FDA and PI, it is likely that the metabolically active cells were confined to the periphery, while the middle portion mainly contained membrane compromised cells (Figure 3.11).

Disruption of the cell membrane is a classical hallmark of necrosis.[226] The observed increase in PI staining and decreased fluorescein retention in the middle spheroid regions suggests centralised cellular necrosis in the developed spheroids. However, careful consideration must be taken when making such an inference solely based on results from the live/dead assay. Dead cells may present residual esterase activity, hence complicating the evaluation of cells that stain positively with both FDA and PI.[227]

Additionally, intact spheroids with many cell layers are used in the analysis of the distribution of FDA and PI across the sample, and reduction of fluorescence intensity could be a consequence of insufficient light penetration rather than the attenuation of metabolic activity. In this way, the true representation of the spatial heterogeneity of cellular viability/death across the spheroids might not be sufficiently revealed. To alleviate these shortcomings, the spheroids were sectioned and histologically evaluated to confirm the results obtained from the live/dead assay.

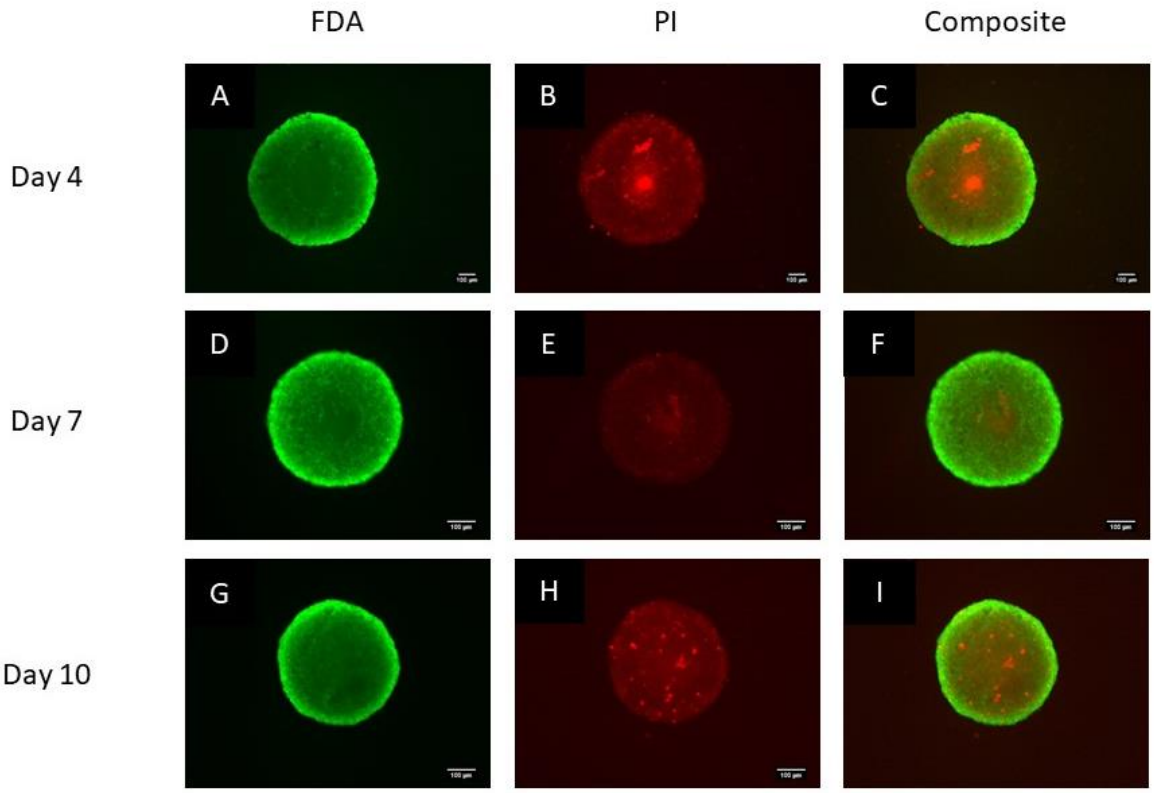

Figure 3.11: *Representative fluorescence microscopy images of spheroids stained with FDA and PI, and a composite thereof on Day 4 (A-C), Day 7 (D-F) and Day 10 (G-I). Images captured using a 5X objective lens, scale bar = 100 µm.*

3.2.5 Histological characterisation of the spheroids

Histological examination has been used to analyse various characteristics of tissue in microscopic environments. A commonly used technique is based on fixation with 4% formaldehyde prior to paraffin embedding and subsequent sectioning.[228] The major challenge with this approach is its laborious and time-consuming nature. Fixation further aggravates this limitation, as it results in cross-linking of antigen binding sites, thus necessitating an investment of time in conducting antigen retrieval steps before

immunostaining.[228] These challenges are worse in the histological analysis of 3D cultures due to their small size and delicate nature.[229] Recently, gelatin embedding has been used prior to cryosectioning and analysis of the spatial distribution of proteins across spheroids.[159] The embedding process is quicker and tissue fixation is not necessary, therefore, the numerous steps associated with paraffin embedding are circumvented.[159] The applicability of gelatin embedding and cryosectioning in the evaluation of the architecture of cells in the BT-20 spheroids was compared to traditional paraffin embedding and microtoming.

The whitish colour of unfixed gelatin-embedded spheroids made them indistinguishable against the milky background of frozen gelatin. To enhance visibility the spheroids were stained with 0.5% gentian violet prior to embedding (black arrows in Figure 3.12 A and B). Staining of cryosectioned spheroids resulted in background staining of the gelatin sections, making it difficult to identify the mounted spheroids on the slide (Figure 3.12 C). Microscopic examination of the mounted slides indicated that the spheroids were torn during sectioning, as indicated by the disruptions of the continuous boarder of the spheroid (Figure 3.12 D). In future, heating of the mounted slides can potentially aid in the removal of the gelatin matrix, however, this heating can result in disruption of the original morphology of the spheroids. Alternative embedding material such as the OCT compound could also be used in facilitating the optimal sectioning of cryopreserved unfixed spheroid samples.[230]

In the paraffin-based protocol, the wax was removed using xylene, resulting in circumvention of background staining of the embedding matrix. Additionally, there was only minimal tearing of the spheroid edges during sectioning of paraffin blocks (Figure 3.13). Paraffin embedding and microtoming were therefore chosen over gelatin embedding and cryosectioning.

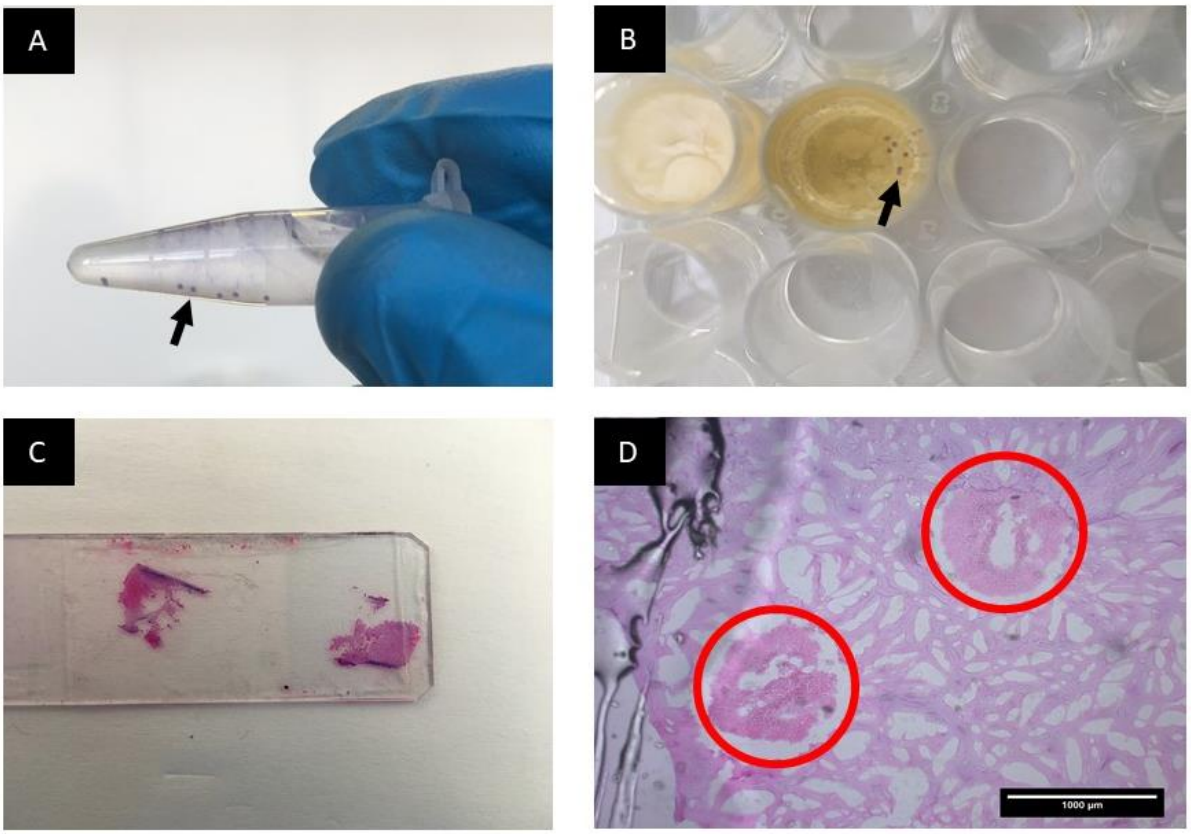

Figure 3.12: *Multicellular spheroids stained with 0.5% gentian violet (A) and embedded in gelatin (B). The mounted slides had background staining (C), and the spheroid structure was not preserved after sectioning (D). Image D captured using a 10X objective lens, scale bar = 100 µm.*

The manual processing of paraffin-embedded samples improves spheroid survival and maintains sample integrity.[229] Spheroid drug screens often generate many samples,[128] resulting in the need to conduct high-throughput histological assessment. Semi-automated tissue processing platforms are conventionally used for the histological assessment of macroscopic clinical samples, however, such arrays cannot be used on spheroids, due to the increased risk of the degradation of the delicate samples.[229] There remains a need to develop techniques that are optimised for the high-throughput, automated analysis of spheroid histology. The development of microarrays for the high-throughput single-cell analysis of spatial patterns in spheroids has consequently garnered attention recently,[178] and successful adoption of such platforms in future can possibly lead to a decrease in the turnaround time and reduction of sample disruption.

The H&E staining pattern was almost homogeneous in Day 4 spheroids, with slightly more nuclear (haematoxylin) staining on the outer spheroid regions compared to the inner areas (Figure 3.13 A). There was a distinct gap separating a cluster of cells in the middle region from the outer rim (yellow arrow in Figure 3.14 B). The cells in the inner portion of the spheroid appeared less disorganised and smaller compared to those on the periphery, suggesting continued spatial differentiation of cellular architecture from Day 4 to Day 7. This differentiation was more pronounced on Day 10, which displayed distinct spatial heterogeneity of cell morphology across the spheroid (Figure 3.13 C). Micrographs of Day 10 spheroids captured using a 40X objective lens indicated that the outer ~90 µm of the spheroid consisted of densely packed cells with evident staining for both nuclear and cytoplasmic components (Figure 3.14 A). In contrast cells in the inner region were smaller, more dispersed, and only predominantly stained with eosin, with minimal binding of haematoxylin (Figure ***3.14*** B).

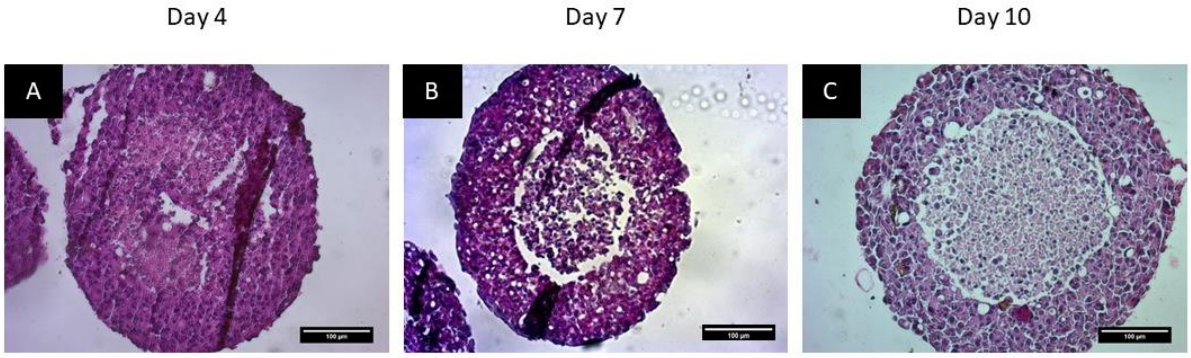

Figure 3.13: *Representative brightfield images of spheroids stained with H&E on Day 4 (A), Day 7 (B), and Day 10 (C). Spheroids captured using a 20X magnification lens. Scale bar = 100 µm.*

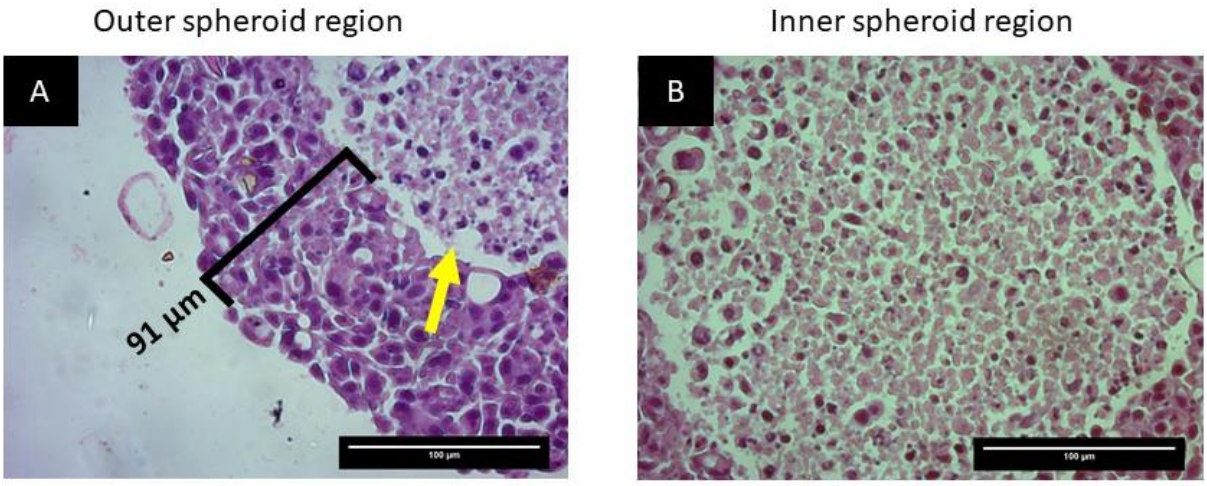

Figure 3.14: *Representative high-magnification brightfield micrographs of H&E stained spheroids. Large and intense staining cells were confined to the outer 91 µm of the spheroid, and a distinct gap separated the inner spheroid region from the outer rim (A). Cells in the inner core appear smaller and predominantly stain with eosin (B). Images captured at 40X magnification. Scale bar = 100 µm.*

Similar findings were reported by the pioneers of the multicellular spheroid model system in 1971. The research group demonstrated that centralised necrosis occurred in multicellular lung cancer spheroids.[143] Analysis of an H&E stained micrograph revealed three distinct zones: an outer layer of four or five darker-staining cells, an intermediate zone containing cells with less densely-staining nuclei, and a central necrotic zone.[143] The distinct gap separating the inner necrotic mass from the outer rim was also apparent (Figure 3.15).

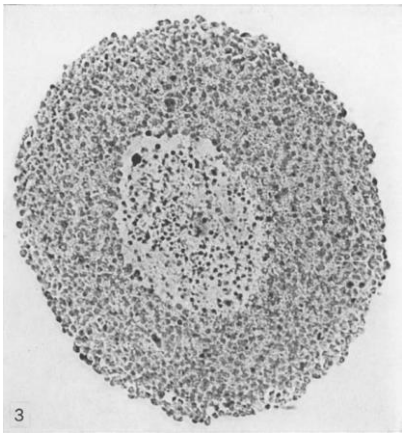

Figure 3.15: *Multicellular spheroid stained with H&E, as described by Sutherland and colleagues.[143] The spheroid has a well-defined necrotic region, surrounded by an outer rim. The diameter of the spheroid is 450 µm. Image reproduced with permission from Oxford University Press, license number: 4527521156868.*

Considering that DNA increases substantially during the S-phase of the cell cycle and that haematoxylin primarily binds to nucleic acids,[201] it is reasonable to assume that the profound staining of haematoxylin in the marginal rim of the BT-20 spheroid is a consequence of the rapid proliferation of these cells. Likewise, the reduction of nuclear staining in the inner spheroid core suggests reduction of growth and potential necrosis of this population of cells. Such a deduction would corroborate with the protein content and live/dead data that speculated the existence of a spatial proliferative gradient with rapidly growing cells near the spheroid margin, and dormant or necrotic cells near the core of BT-20 spheroids.

From early days of spheroid research, it was established that the development of centralised necrosis is a function of the diameter, with occurrence of cellular necrosis from spheroids with a diameter of 400 µm and above.[231] Spheroids developed in the current study had diameters that are larger than this, therefore, development of necrosis in cells within the inner regions was likely.

Various mathematical models have been used to establish the role of microenvironmental cues in the development of cellular necrosis in multicellular spheroids.[232] All these models suggest that both cellular necrosis and cell proliferation are dependent on the concentration of molecules that diffuse from surrounding culture media into inner parts of spheroids.[232] Examples of such chemicals are glucose and O_2. The proliferation rate of cells in spheroids is thought to be an empirical function of these molecules.[219]

In the late 1980s, it was demonstrated that necrosis is caused by joint-deprivation of both glucose and O_2. It should be kept in mind that the depletion of a single molecule does not exclusively lead to necrosis in tumour analogues.[233] Cells that are only starved of O_2 could use anaerobic glycolysis, and cells deprived of only glucose could catabolize other substances to survive, provided they still retain the ability to carry out oxidative phosphorylation.[233] However, there is no obvious mechanism of survival for cells that lack both O_2 and glucose.[233] Joint-starvation of O_2 and glucose can result in the depletion of ATP, and cell death has been demonstrated in spheroids when ATP levels are below a specific critical level.[232]

The necrosis in the BT-20 spheroids could accordingly have been due to reduced O_2 and glucose delivery into the inner part of the spheroids. Even though the medium was replenished constantly, the third dimension in the inherent conformation of spheroids might pose a barrier to sufficient penetration of molecules across the entire structure. Small molecules penetrate easily in loose spheroids, compared to more compact ones.[205] Therefore, it could have been more difficult for nutrients to sufficiently diffuse as the spheroid compacted during growth, thus explaining the continued differentiation of cellular morphology in the spheroid core from Day 4 to Day 10.

In addition to joint O_2 and glucose depletion, other factors contribute to the development of necrotic regions in spheroids. The pH is known to decrease with depth into the spheroid centre.[131] Due to low oxygenation, the cells in inner spheroid regions might adapt to anaerobic metabolism, leading to the accumulation of acid and other metabolic waste and subsequent death.[131] Freyer and colleagues[234] isolated and partially purified extracts from spheroids with extensive necrosis, and these extracts demonstrated cytotoxic activity on monolayer-cultured cells. This led to the speculation that the release of growth-inhibitory molecules by necrotic cells in spheroids causes the collateral damage of neighbouring cells, ultimately exacerbating centralised necrosis.[234]

Although various mechanisms have been proposed to explain this existence of growth-regulatory substances in necrotic spheroid regions,[234] very limited efforts have been made to provide insight into the role of such chemical mediators. However, in a recent study,[235] the content within necrotic regions of breast cancer spheroids was isolated and analysed. It was shown that the content of these necrotic cells enhances angiogenesis and proliferation of endothelial cells, induces vasculature and increases migration, invasion, and cell-cell interactions *in vitro*.

In vivo experimentation in the same study, where xenografts of these breast cancer cells were exposed to necrotic lysates resulted in enrichment of tumour-promoting factors. These findings suggest a paradigm shift where characterising and therapeutic targeting of factors secreted by necrotic cells can be used to enhance therapy.[235] Tumour necrosis occurs primarily in advanced fast growing tumours,[236] characterisation of these chemical entities in necrotic tumour regions may be hampered by some of the limitations associated with human and animal testing. The

observed necrosis in the BT-20 spheroids renders the model a potentially attractive alternative platform for conducting such investigations.

While necrotic cell death in central regions of these BT-20 spheroids was demonstrated, the potential existence of dormant cells in this region cannot be neglected. Though the inner region of Day 10 spheroids predominantly stained for eosin, the region was not completely void of haematoxylin-positive cells. A few dispersed nuclei were identified on the inner core of the spheroid (Figure 3.14 B), however, they appear smaller than the nuclei in the outer rim, suggesting reduced growth of some of the cells in the core (Figure 3.14 A). Correspondingly, as shown in Figure 3.11 G, the cells in the central spheroid regions exhibited a level of metabolic activity though it was lower than that of cells in the outer rim. Combining these observations, it could be speculated that there is a co-existence of both necrotic and dormant cells within the inner circle of the BT-20 spheroids. However, staining with markers for dormancy and apoptosis will need to be conducted in future to conclusively demonstrate this.

A closer observation of the outer spheroid rim shows that cells in the peri-necrotic half appear to have slightly less nuclear staining and smaller cells than the outermost half (approximately five to seven cell layers). This peri-necrotic portion of the outer rim could potentially be the ‘dormant layer’. It has been reported that proliferative cells make up about three to five cell layers of the viable rim while quiescent cells are located more centrally.[142] Therefore, even though the presence of dormant cells in the spheroid is very likely, their distribution is not clearly defined.

Researchers widely describe a concentrically-ordered pattern of spatial distribution of the proliferative potential of cells across multicellular spheroids, with an inner necrotic core, a middle dormant layer, and an outer proliferative rim.[131,220] However, in many experimental settings, this systematic distribution of different cells across spheroids is not always obvious. For example, in a recent study,[237] necrosis (indicated by H&E staining, Figure 3.16 A) and apoptosis (indicated by caspase-3 staining, Figure 3.16 C) were restricted to an inner core of LLC human sarcoma spheroids, while proliferative cells (indicated by Ki-67 staining) were restricted to the outer rim (Figure 3.16 B), without a clear gradient of distribution of these parameters across the spheroids.[237] Additionally, the morphological characterisation of a panel of spheroids of eleven

different cell lines using H&E staining showed that while some spheroids had a faintly-staining necrotic core, spheroids from some cell lines stained uniformly.[178] Therefore, the potential existence and extent of zonation of spheroids are reliant on experimental conditions and the identity of the cell line in question.

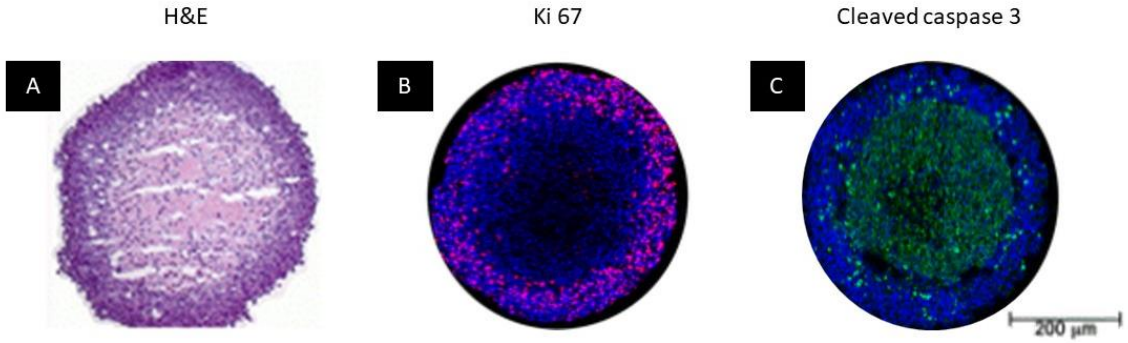

Figure 3.16: *Sections of LLC human sarcoma spheroids stained with H&E (A), Ki-67/DAPI (B) and cleaved caspase-3 (C). Scale bar = 200 µm. The image was adopted and slightly modified from Riffle et al.[237] There is no clear distinction of the distribution of spheroids zones. Permission to reprint provided under the Creative Commons Attribution 4.0 International License.*

The presence of dormant cells within spheroid regions has been previously reported.[125] Similar to poorly-perfused tumour microregions, some cells within inner spheroid regions remain in a viable, but non-proliferative state due to reduced O_2 and nutrient supply.[125] Additionally, some cells are known to disseminate from the primary tumour to distant sites where they remain inactive for many years.[149] Dormant cells often 'awaken' into a proliferative state after years or decades after chemotherapy to form resistant metastases.[155]

Patients with dormant disseminated tumour cells are, therefore, at a higher risk of metastatic relapse,[155] and this highlights the importance of understanding the biology of dormant cancer cells. As such, elucidation of mechanisms underlying the dissemination and reactivation of dormant tumour cells is a recent awakening field.[150] A variety of genetically engineered, orthotropic and metastatic mouse models have been used to gain insight into tumour cell dormancy.[238] However, the drawback of these models is their inability to allow for sufficient control of the organ environment for controlled investigations. Additionally, the inter-animal variability and costly nature of such models can render their use in studying cancer dormancy a challenging pursuit.[238] In recent years, bioengineered models (including 3D cultures) for studying

the role of the TME in cellular dormancy have been developed and extensively reviewed.[238] Multicellular 3D culture models such as the BT-20 spheroids described here could be useful as future tools for probing the role of the TME in regulating tumour dormancy, as they allow for optimum recapitulation of the tumour micromilieu in a physiologically robust and controlled manner.

Parameters such as glucose consumption, and accumulation of acid and various growth-regulatory mechanisms could have played a role in the observed spatial difference in the morphology of cells across the spheroid. However, the evaluation of such cues within the BT-20 spheroids was beyond the scope of the current study, due to the complexity associated with such analyses. Hypoxia plays a key role in the induction of cellular necrosis and other key features within the tumour micromilieu.[115] The development and commercialisation of a cell-permeable, iridium-complex that quickly fluoresces in environments with less than 5% O_2 have provided a flexible tool for detecting hypoxic environments within multicellular spheroids.[177] This type of probe was used to assess the induction of hypoxia within BT-20 spheroids.

3.2.6 Investigation of hypoxia within the spheroids

On spheroid culture Day 4, fluorescence of the Image-iT® probe was confined to the inner spheroid regions, while the fluorescent signal was slightly attenuated in the outer regions (Figure 3.17 A-C). On Day 7, the fluorescence intensity of the probe increased across the spheroids, with a marginal rim displaying reduced fluorescence (Figure 3.17 D-F) indicative of higher than 5% oxygen concentrations. With a smaller marginal rim that had minimal staining, the fluorescence was distributed through virtually all areas of Day 10 spheroids (Figure 3.17 G-I). The inner most spheroid regions had minimal staining, and this could be either due to i) limited penetrance of the probe, ii) light scattering within deep spheroid regions or iii) fluorescence quenching of the probe by metabolic waste. No fluorescence was detected in monolayers cultured for 24 h. These observations suggest the inherent development of hypoxic regions which increases with growth in BT-20 spheroids cultured in normoxic conditions, while such a hypoxic phenomenon is not evident in the monolayer-cultured counterpart.

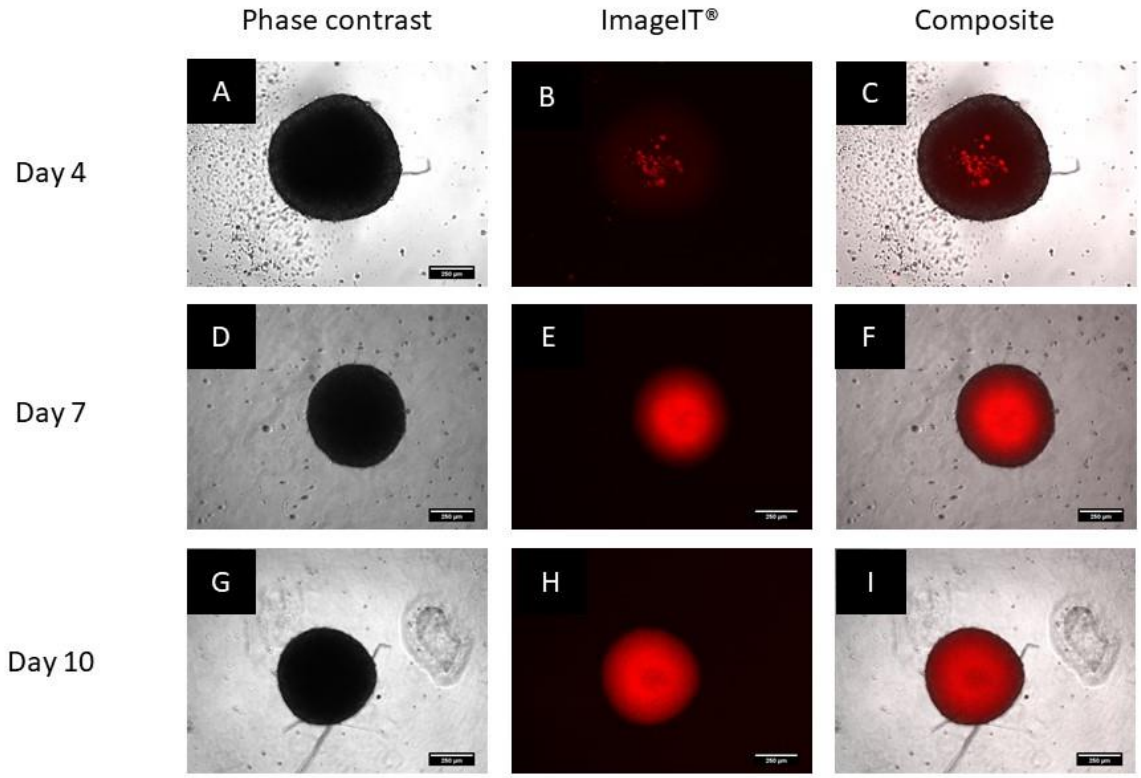

Figure 3.17: *Phase contrast, fluorescence and a composite of spheroids stained with the Image-iT® hypoxia probe on Day 4 (A-C), Day 7 (D-F) and Day 10 (G-I). All images captured using a 5X objective lens. Scale bar = 250 µm.*

The gradient profiles of the oxygenation status across the viable rim and necrotic regions of spheroids have been extensively described, and these gradients may vary in different spheroid types.[142] Hypoxia occurs to some degree in many *in vivo* solid tumours due to rapid O_2 depletion, inadequate neovascularization, and insufficient blood flow.[239] Cancerous tissue often exhibits heterogeneity in O_2 concentrations which range from normoxia to mild hypoxia and severe levels of hypoxia.[239] The development of hypoxia has implications on the cellular behaviour and therapeutic response of tumor cells.[239] Similarly, cells within spheroids are reported to undergo various adaptations within the hypoxic environment to promote the evolution of cells with a potentially aggressive phenotype.[240]

Severe hypoxia causes replication stress, which results in activation of the DNA damage response (DDR) kinases, Ataxia Telangiectasia Mutated (ATM) and ATM-and-Rad3 related (ATR).[1] These kinases then phosphorylate downstream targets such as the H2A histone family member X (γ-H2AX), p53-Ser15, Chk1-Ser345, and

Chk2-Thr68.[1] These ATM/ATR-regulated targets mediate the stabilisation of replication forks, prevent further DNA damage, initiate repair, and ultimate cellular survival. The phosphorylation of γ-H2AX is a critical step in facilitating the repair and survival of DNA-damaged cells.[1] In a recent study,[237] the spatial correlation between cellular proliferation and γ-H2AX staining in hypoxic regions of multicellular tumour spheroids was demonstrated, suggesting hypoxia-induced DDR and subsequent survival in 3D-cultured cells.

Hypoxia in spheroids often correlates with glucose deprivation.[233] In environments that are deprived of O_2 and glucose, cells in tumours metabolically adapt by storing glycogen during mild hypoxia, which is subsequently broken down to glucose during severe hypoxia.[13] Recapitulation of such metabolic adaptation was recently demonstrated in multicellular spheroids.[241] Characterisation of the glucose consumption of a human colon carcinoma spheroid model showed that rapid consumption of glucose was coupled with increased production of lactate and acidification of medium, confirming a metabolic switch from oxidative phosphorylation to glycolysis.[241] The simulation of cellular metabolic adaptations observed *in vivo* demonstrates the potential worth of spheroids as a physiologically relevant model for the *in vitro* therapeutic targeting of metabolic pathways in cancer.[240]

The therapeutic efficacy of anti-cancer compounds could, therefore, be affected by the adaptations of cells to the hypoxic environment of multicellular tumour spheroids. In combination with hypoxia, other phenotypic attributes of the BT-20 cell spheroids could contribute to the differential response to chemotherapy, in comparison to monolayers. For example, it has recently been shown that the induction of both hypoxia and necrosis contributes to the resistance of spheroids to 5-flourouracil.[242] Considering the possibility of altered drug susceptibility, the chemotherapeutic sensitivity of BT-20 cells was compared to that of monolayers.

3.3 Comparative assessment of the efficacy of doxorubicin in 2D and 3D

It is increasingly recognised that monolayer culturing is not a reliable *in vitro* platform for predicting the *in vivo* therapeutic efficacy of antineoplastic drugs.[214] Multicellular spheroids are emerging as a better *in vitro* alternative for conducting drug screens of innovative chemotherapy compounds, as these models better-simulate the

microenvironmental cues of *in vivo* tumours.[131] Prior to the adoption of the 3D model in such drug screening, it may be necessary to investigate the chemosensitivity of spheroids to drugs that are already in clinical use. In addition to allowing for the comparison of the efficacy of the compounds to the response observed *in vivo*, such probing would allow adoption of clinically-approved drugs as treatment controls when conducting drug screening of novel chemical entities on spheroids.[128] Examples of such compounds include cisplatin, doxorubicin, 5-fluorouracil, irinotecan and paclitaxel.[128] Doxorubicin was chosen in the current study to investigate the differential response of monolayer- and 3D-cultured BT-20 cells.

In the current study, the cytotoxic range of doxorubicin was evaluated on monolayer cultured cells prior to investigation of the effects of these concentrations on the BT-20 spheroids.

3.3.1 Evaluation of the monolayer cytotoxic range of doxorubicin

A wide array of cell enumeration assays exists for the evaluation of toxicity of compounds on cultured cells, each one with its associated advantages and shortcomings.[243] When choosing an assay for the cytotoxic evaluation of compounds, it is necessary to consider the linear range, sensitivity and reproducibility of the technique. The SRB assay is the preferred platform for screening lead compounds at the National Cancer Institute in the United States of America.[243] In addition to possessing high sensitivity, the SRB assay has low variability in comparison to other commonly-used monolayer cell enumeration assays, therefore, minimal replicates have to be conducted to obtain reliable results.[243] The SRB assay was therefore chosen to obtain the cytotoxic range of doxorubicin on 2D-cultured BT-20 cells. The APH assay was conducted in parallel as a means of partially confirming the dose-response observed with the SRB assay.

Increasing concentrations of doxorubicin exerted a sigmoidal, dose-dependent reduction in both cell density (Figure 3.18 A) and APH activity (Figure 3.18 B). The toxic and sub-toxic concentrations of doxorubicin tested are provided in Table 3.1. An IC_{50} of 310 nM and 287 nM was obtained with the SRB and APH assay, respectively. However, the IC_{25} and IC_{75} values obtained from the APH assay were lower than those from the SRB assay. While the sigmoidal dose-response tapers off at high concentration in the SRB assay, a complete cytotoxic response is noted with the APH

assay. The mechanistic differences in the principle of cytotoxicity evaluation may explain the discrepancies observed between the IC_{25} and IC_{75} of the two assays. In the APH assay, cytotoxicity is estimated by evaluating the alteration of metabolic activity, a cellular parameter that may be attenuated without significant cell death.[161] The SRB assay, on the other hand, is deemed as a true cell enumeration assay, as it does not rely on metabolic activity, but rather binds to fixed proteins and some dead cell portions.[202] In doing so, limitations associated with biological parameters that could alter cellular metabolic activity are circumvented. Additionally, the SRB assay is sensitive enough to detect low numbers of cells that are viable, which would potentially not be the case in metabolism-based enumeration assays.[243]

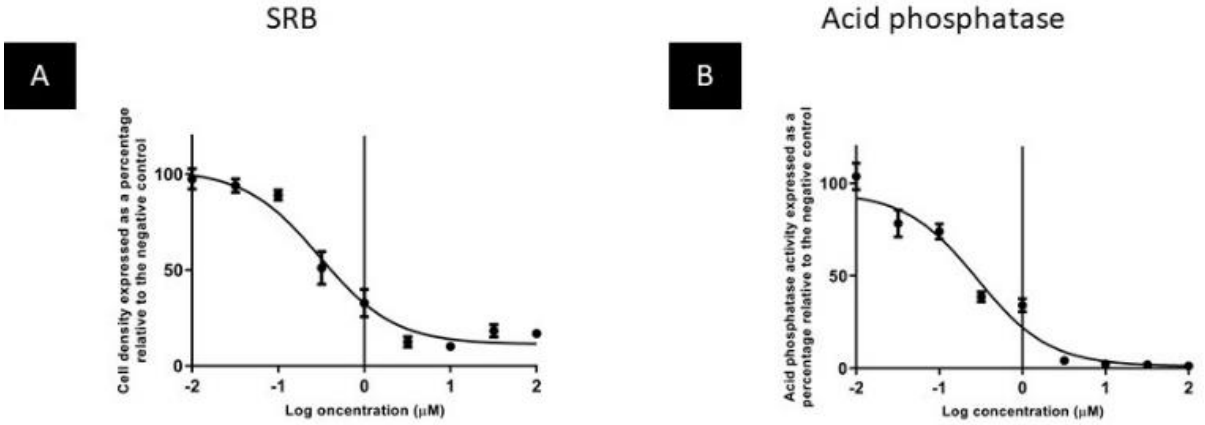

Figure 3.18: *Dose-response curves showing the alteration of cell density, N = 5 biological repeats (A) and APH, N = 4 biological repeats (B) of monolayers treated with half-log dilutions of 32 µM doxorubicin for 72 h. The IC_{50} was calculated using non-linear regression curve fit (log[inhibitor] vs response) with robust fit.*

Table 3.1: *Toxic and sub-toxic concentrations of doxorubicin (72 h) obtained using the SRB and APH assays.*

	IC_{25}	**IC_{50}**	**IC_{75}**
SRB	130 nM	310 nM	1580 nM
APH	79 nM	287 nM	850 nM

The concentrations from the SRB assay were, then used for downstream experimentation. Phase contrast microscopy and FDA staining were used to investigate the effect of toxic and sub-toxic concentrations of doxorubicin on monolayer cell density and viability, respectively. The number of cells per surface area decreased with increasing concentrations of doxorubicin, as indicated by the phase

contrast micrographs in Figure 3.19 (A-D). Similarly, the amount of staining of FDA decreased with increasing concentrations of doxorubicin, indicating reduced viability at the concentrations used (Figure 3.19 E-H).

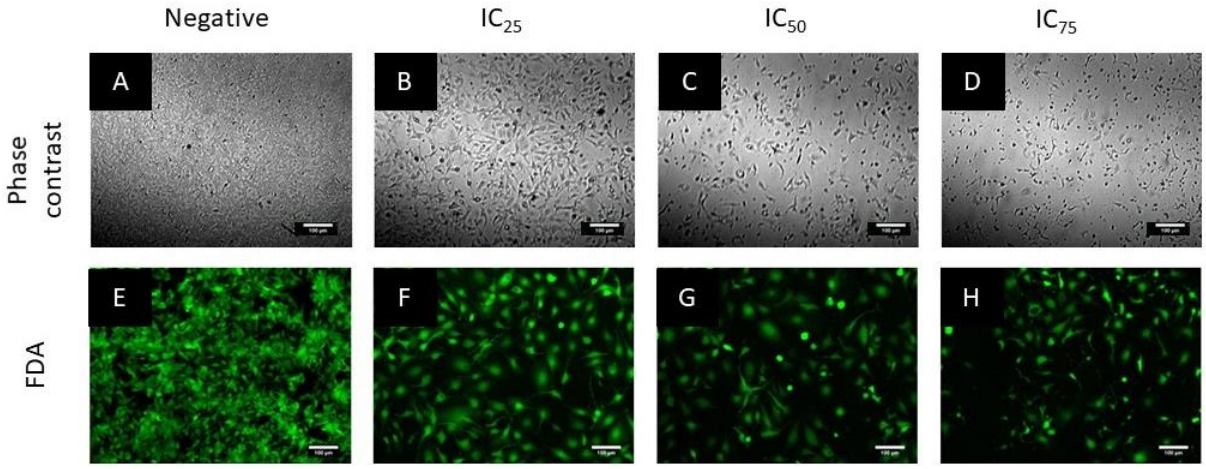

Figure 3.19: *Phase contrast micrographs (A-D), and fluorescence microscopy images of monolayers treated with toxic and sub-toxic concentrations of doxorubicin for 72 h. Images captured using a 10X objective lens. Scale bar = 100 µm.*

Doxorubicin elicited a cytotoxic response on monolayers at the concentrations, as indicated by the dose-responses in Figure 3.18 and the alteration of cellular parameters indicated in Figure 3.19. Comparable IC_{50} values of doxorubicin have widely been reported. For example, the evaluation of the antiproliferative efficacy of doxorubicin on a panel of ten different breast cancer cell lines using the SRB assay indicated that the concentrations required to inhibit cellular growth by 50% ranged from 181 nM to 1122 nM, with an IC_{50} of 459 nM for BT-20 monolayers.[244] The slight difference in the IC_{50} of doxorubicin to that in the current study can be attributed to different experimental parameters such as the seeding density, however, it is apparent that doxorubicin induces a cytotoxic effect on BT-20 monolayers within the hundred-nanomolar concentration range. Within these concentrations, doxorubicin induces cell death via several mechanisms including topoisomerase poisoning and cell cycle arrest at the G2/M phase of the cell cycle (Table 3.2).

Table 3.2: *Cytotoxic mechanisms of doxorubicin and their corresponding concentrations. Table adapted from Yang et al.*[245]

Mechanism	Concentration	Reference
Topoisomerase II poisoning	400 nM	Gewirtz et al[246]
Free radical formation	100 nM	Doroshow et al[247]
Ceramide overproduction	300 nM	Coldwell et al[248]
G2/M phase arrest	1 µM	Ling et al[249]

The anticancer efficacy of doxorubicin can mainly be attributed to inhibition of the topoisomerase II enzyme.[102] This is a highly-conserved ATP-dependent enzyme that maintains the tri-dimensional structure of DNA through breaking and re-sealing the entangled portions of DNA, thus releasing the torsional stress formed during replication.[250] Inhibition of the enzyme impedes the resealing of DNA, leading to DNA damage, inhibition of DNA replication, failure to repair strand breaks and ultimately cell death.[250]

Doxorubicin can exert its cytotoxic effects by inducing apoptosis via various mechanisms. The drug increases the levels of ceramide,[248] a lipid molecule that is involved in various cellular processes such as growth arrest and apoptosis. It has also been shown that the growth-inhibitory effects of doxorubicin are cell cycle-dependent and are partially mediated through the dysregulation of a $p34^{cdc2}$/cyclin B1 complex, which leads to a G2/M phase arrest and subsequent apoptosis.[249] Additionally, doxorubicin can induce apoptosis by enhancing the expression of death receptor 5 (DR5).[251] The tumour necrosis factor-related apoptosis-inducing ligand (TRAIL) interacts with the DR5 to induce apoptosis via the death inducing signaling cascade. It has been recently shown that doxorubicin acts as a DR5 agonist to augment TRAIL-mediated apoptosis in TNBC cells.[251]

Addition of one electron to the quinone moiety of doxorubicin by NADP(H) oxidoreductases results in the formation of a semiquinone radical. This semiquinone reacts with O_2, to form superoxide and hydrogen peroxide (H_2O_2).[252] Additionally, doxorubicin forms complexes with iron, which catalyse the conversion of H_2O_2 to highly reactive hydroxyl radicals. Doxorubicin-induced production of free radical causes oxidative stress and consequential cellular death.[245]

Considering that monolayers may display distinct susceptibility to chemotherapeutic drugs compared to spheroids of the same cell line, the cytotoxic concentrations determined using the SRB assay were used evaluate the efficacy of doxorubicin in monolayers, compared to spheroids.

3.3.2 Cytotoxic efficacy of doxorubicin on spheroids

While the percentage APH activity relative to the negative control at the IC_{25}, IC_{50} and IC_{75} decreased significantly ($P \leq 0.0001$) in monolayers (Figure 3.20 A), the enzymatic activity was not significantly ($P > 0.05$) altered in multicellular spheroids (Figure 3.20 B).

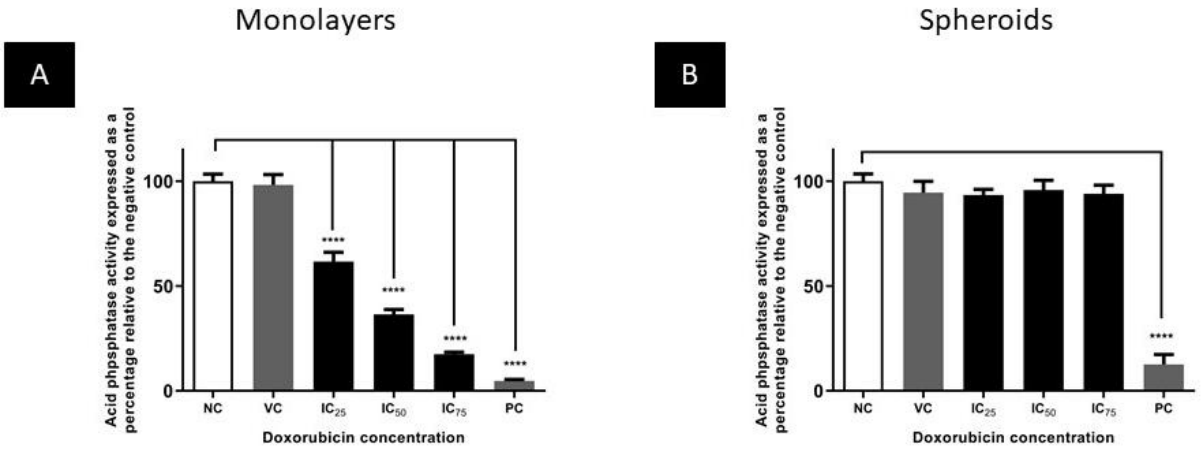

Figure 3.20: *The effect of the IC_{25}, IC_{50}, and IC_{75} of doxorubicin on the APH activity of monolayers, N = 4 biological repeats (A) and Day 4 spheroids, N =7 biological repeats (B). **** = P ≤ 0.0001. Statistical significance calculated using one-way ANOVA, with Dunn's multiple comparison post-test. NC = negative control, PC =positive control, VC = vehicle control.*

Relative to the negative control, the circular morphology and the integrity of the spheroids was maintained at the IC_{25}, IC_{50}, and IC_{75} (Figure 3.21). Additionally, the IC_{25} and the IC_{50} did not significantly ($P > 0.05$) alter the volume of the spheroid in comparison to the negative control, while the IC_{75} significantly ($P \leq 0.001$) decreased the spheroid volume by only 25% (Figure 3.22). Taken together, these results indicate that concentrations that elicit a cytotoxic response in monolayers did not alter spheroid volume and metabolic activity (robust parameters for endpoint analysis of drug efficacy on spheroids), thereby reducing the efficacy of the drug in spheroids compared to monolayers.

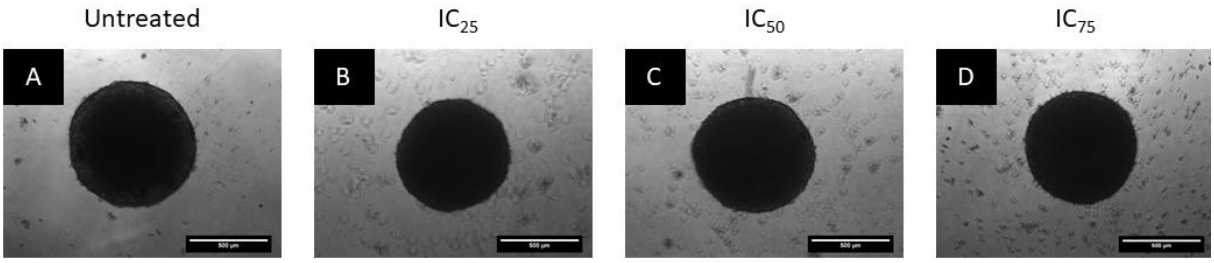

Figure 3.21: *Representative phase contrast images showing the change in morphology of spheroids after a 72-h treatment of Day 4 spheroids with the IC_{25} (A), IC_{50} (B) and IC_{75} (C) of doxorubicin. Images captured using a 5X objective lens, scale bar = 500 µm.*

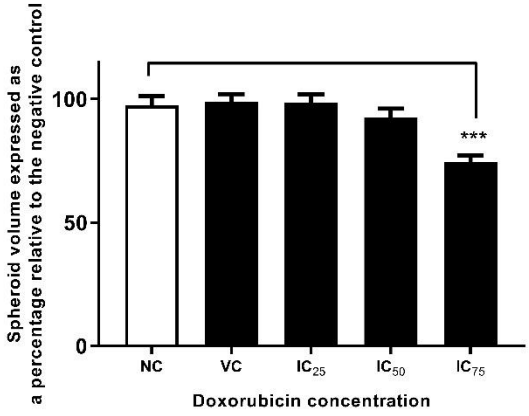

*Figure 3.22: Change in the volume of spheroids relative to the negative control after a 72-h treatment with the IC_{25}, IC_{50}, and IC_{75} of doxorubicin. N = 5 biological repeats. *** = P ≤ 0.001. Statistical significance calculated using one-way ANOVA, with Dunn's multiple comparison post-test. NC = negative control, PC = positive control, VC = vehicle control.*

To investigate whether higher concentrations of doxorubicin could elicit a cytotoxic effect on multicellular spheroids, the 3D model was treated with 3 µM, 6 µM, 8 µM, and 10 µM of this compound. At these concentrations, the structural integrity of spheroids was disrupted, with loss of the smooth edges at 3 µM (Figure 3.23 G), and disintegration of cells at concentrations >6 µM (Figure 3.23 H-J). Medium replenishment enhanced the elucidation of the alteration of the structural integrity of spheroids by doxorubicin. Prior to changing medium, the spheroids treated with higher concentrations (6, 8 and 10 µM) appeared larger than the negative control (Figure 3.23 C-E), and this could potentially be erroneously interpreted as an increase in spheroid volume at these concentrations. However, after medium replacement, a substantial number of cells were washed off, revealing the true disrupted morphology and decreased size of these spheroids (Figure 3.23 H-J). The importance of replacing

medium prior to analysing images of treated spheroids was previously emphasised, where the existence of a halo of dead and apoptotic cells at high drug concentrations was shown to impede image analysis, and washing these cells improved the speed and accuracy of analysis of spheroid size.[129] The substantial deterioration of the 3D architecture of breast cancer multicellular spheroids treated with 10 µM doxorubicin has also recently been reported.[253] Spheroid disintegration at high concentrations is most likely due to loss of cell-cell adhesion, as doxorubicin has recently been shown to alter cell membrane properties,[254] and E-cadherin expression levels.[255]

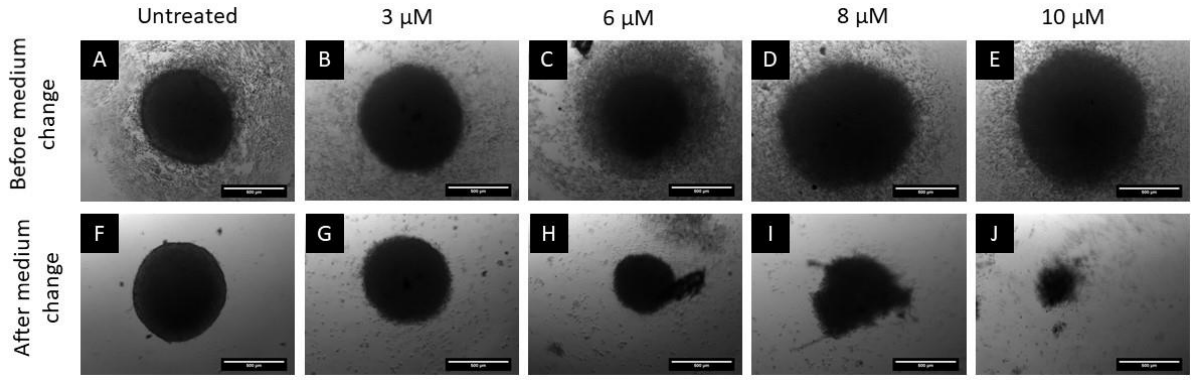

Figure 3.23: *Representative phase contrast microscopy micrographs of spheroids treated with various concentrations of doxorubicin for 72 h, before (A-E) and after (F-J) replenishment of cell culture medium. Images captured using a 5X objective lens. Scale bar = 500 µm.*

Though in some instances the spheroid disintegrated completely at concentrations above 6 µM, the projected area of those that did not completely dismantle was used to estimate the resultant spheroid volume. There was a significant ($P \leq 0.0001$) decrease in the average spheroid volume in comparison to the negative control when treated with 3 µM, 6 µM, 8 µM, and 10 µM doxorubicin (Figure 3.24). Similarly, the APH activity in comparison to the negative control was significantly reduced after treatment with 6 µM ($P \leq 0.01$), 8 µM ($P \leq 0.0001$) and 10 µM ($P \leq 0.0001$) doxorubicin (Figure 3.24).

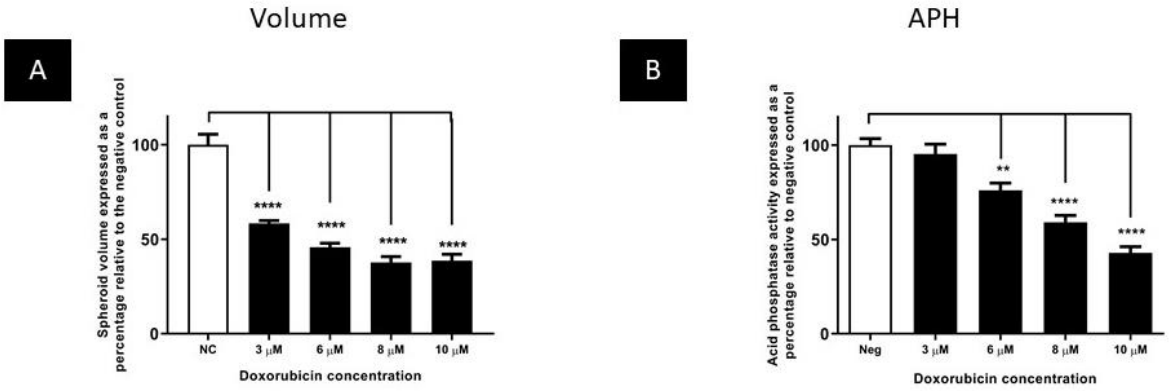

Figure 3.24*: Effect of high concentrations of doxorubicin (72 h) on the volume of spheroids, N = 4 biological repeats (A) and APH activity, N = 3 biological repeats (B) of spheroids in comparison to the negative control. ** = P ≤ 0.01, **** = P ≤ 0.0001. One-way ANOVA, with Dunn's multiple comparison post-test, NC = negative control.*

There are many limitations that render quantitative toxicology more complicated in spheroids compared to monolayers. Such limitations include 1) difficulty in accurately quantifying cell number; 2) extracting small portions of spheroids for analysis, due to their minute size and 3) cells have slower growth rates when cultured in 3D format. To overcome these challenges, Fey and Wrzesinski[256] normalised the drug dose (mg) to spheroid protein content (mg), allowing for the expression of the dose used in 3D cultures as mg drug/mg spheroid protein content. Such an approach can more easily be related to *in vivo* dosing, which is typically expressed as mass of drug (mg) per body weight of the animal in kilograms (Kg).[256]

In the current study, the 3D cultures had an average of 7.0 µg of cellular protein per spheroid on the day of treatment (Day 4). Normalisation of the IC_{50} with this protein content results in the extrapolation of a dose of 0.01 mg of doxorubicin/mg of cellular protein. In a 2011 study, an intravenous dose of 1.5 mg/Kg of doxorubicin resulted in significant reduction in tumour volume of a TNBC xenograft mouse model.[257] This dose of doxorubicin is commonly used in mouse studies and is equivalent to $1.5x10^{-6}$ mg doxorubicin/mg of the animal model, a very small amount compared to the IC_{50} dose obtained in the current study.

Though weight alone is commonly used in dose-translation studies, consideration of the surface area should be incorporated in such studies to allow for more appropriate dose extrapolation.[258] In devising the method for expressing the dose as a function of protein content, Fey and Wrzesinski[256] used planimetric analysis to demonstrate a correlation of spheroid area with protein content, a procedure which was not conducted in the current study. The correlation between the projected area and protein content of BT-20 spheroids, therefore, needs to be investigated further. Although it is currently not possible to relate the effective dose in monolayers or spheroids to the response observed *in vivo*, it is apparent that the BT-20 spheroids confer some level of resistance/reduced chemotherapeutic sensitivity compared to monolayer cultures.

The reduced sensitivity of the multicellular spheroids to doxorubicin, compared to the monolayer counterparts can be ascribed to several factors. The dense structural architecture of BT-20 spheroids could have hampered penetration of doxorubicin to all spheroid regions. When analysing spheroids of six breast cancer cell lines it became apparent that cell lines that formed loose spheroids displayed similar sensitivity to doxorubicin as the monolayer counterpart, while dense spheroids were more resistant.[214] Moreover, the addition of hyaluronidase to promote penetration has been shown to enhance the cytotoxic efficacy of doxorubicin in multicellular spheroids.[259] In addition to posing a barrier to sufficient drug penetration, the tight interactions of the cells within the spheroids, could preclude adequate perfusion of O_2, and subsequently induce hypoxia within spheroids.[240]

It is generally accepted that the development of hypoxia within solid tumours decreases the chemosensitivity of neoplastic cells and that experimental hypoxia induces resistance of various cell lines to anticancer drugs.[239] Therefore, the development of hypoxia in the BT-20 spheroids could have played a role in the attenuation of the cytotoxic efficacy of doxorubicin. As detailed in Section 3.2.6, cells in multicellular spheroids adapt to hypoxia by expressing phenotypic features that could promote survival and drug resistance.[240] The activation of DDR pathways in response to hypoxia implies that the DNA-damaging mechanistic action of doxorubicin could be circumvented.

The HIF-1α transcription factor is a vital component that mediates cellular adaptations to hypoxia. In addition to the previously stated adaptations, the activation of HIF-1α in tumour cells leads to increased expression of P-glycoprotein (P-gp), a transmembrane transporter that is responsible for the energy-dependent efflux of anticancer drugs out of cells.[260] It has been demonstrated that the activation of HIF-1α leads to increased expression of P-gp and increased resistance of breast cancer multicellular spheroids to doxorubicin.[260] Potentially rapid drug efflux could be responsible for the decreased sensitivity of BT-20 spheroids compared to monolayers.

Siddarth et al.[261] demonstrated that BT-20 spheroids express higher levels of DR5 and are more resistant to TRAIL-mediated apoptosis, compared to monolayers. Considering that doxorubicin partially exerts its cytotoxic effects through stabilizing the DR5-TRAIL apoptotic complex,[251] the decreased expression of DR5 could lead to circumvention of doxorubicin-induced apoptosis, and consequential reduction of the chemotherapeutic sensitivity of BT-20 spheroids.

The observed spatial heterogeneity of cells in the BT-20 multicellular spheroids could also have played a role in the reduced efficacy of doxorubicin. Doxorubicin and many other anticancer drugs target actively proliferating cells.[155] The outer faster proliferating rim of cells was potentially chemosensitive to doxorubicin, as evidenced by the decrease in spheroid size at the IC_{75}, while slower-cycling cells near the spheroid core were more resistant. Consistent with this, doxorubicin has been found ineffective in targeting solitary dormant cells injected into a murine mouse model.[156] Additionally, the enhanced cell-ECM interactions in the spheroids have recently been shown to play a pivotal role in the resistance of spheroids to doxorubicin compared to monolayers.[253]

Though mechanistic evaluation was not conducted, it is apparent that the reduction of sensitivity of the BT-20 spheroids to doxorubicin can be mediated through multifactorial mechanisms. Similarly, although TNBC is more sensitive to anthracycline-based chemotherapeutic approaches like doxorubicin compared to endocrine positive breast cancers, only a few patients fully benefit from chemotherapy, as 70% of TNBC patients have residual disease after chemotherapy, which is partially ascribed to chemoresistance.[262] Exploring the mechanisms of chemotherapeutic

resistance in TNBC could play a significant role in the improvement of the clinical outcome of TNBC.

3.3.2.1 Spheroid clearing and imaging of doxorubicin-treated spheroids

Imaging 2D-cultured monolayers is straightforward, however, more advanced imaging techniques are required when attempting to investigate protein expression and localization within interior cells of spheroids.[127] Serial sectioning and subsequent histological staining can be used to visualize the internal structure of spheroids as shown in the current study. However, these are time-consuming and can disrupt the 3D structure to introduce structural artefacts. Confocal microscopy can be used as an alternative although the depth of imaging is limited due to light scattering.[181] To overcome this shortcoming, optical clearing methods that remove scattering substances and provide refractive index matching have recently been described,[185] allowing for improved confocal imaging of multicellular spheroids.

To analyse the proliferative capacity of cells within the spheroids before and after treatment with doxorubicin, treated BT-20 spheroids were stained for the proliferation marker, Ki-67, made transparent, and imaged. To identify single cells within the spheroid, cadherins were stained using a pan cadherin pAb while nuclei were stained using DAPI.

Untreated spheroids displayed very low and diffuse staining for Ki-67, whereas cadherin staining indicated the cell boundary of each cell within the spheroid. Compared to the negative control, a decrease in the expression of cadherins was observed in doxorubicin-treated spheroids (Figure 3.25). At the highest concentrations, the spheroid had diminished in size and most of the cadherin staining appeared intracellular rather than on the cell border. All staining appeared somewhat diminished in the centre of spheroids, most likely due to lack of penetrance of laser light to this depth. The cadherin staining implies that cells were under duress at higher doxorubicin concentrations and lost their cell-cell adhesive capability, which corresponds with the disintegration of the 3D structure observed using phase contrast microscopy.

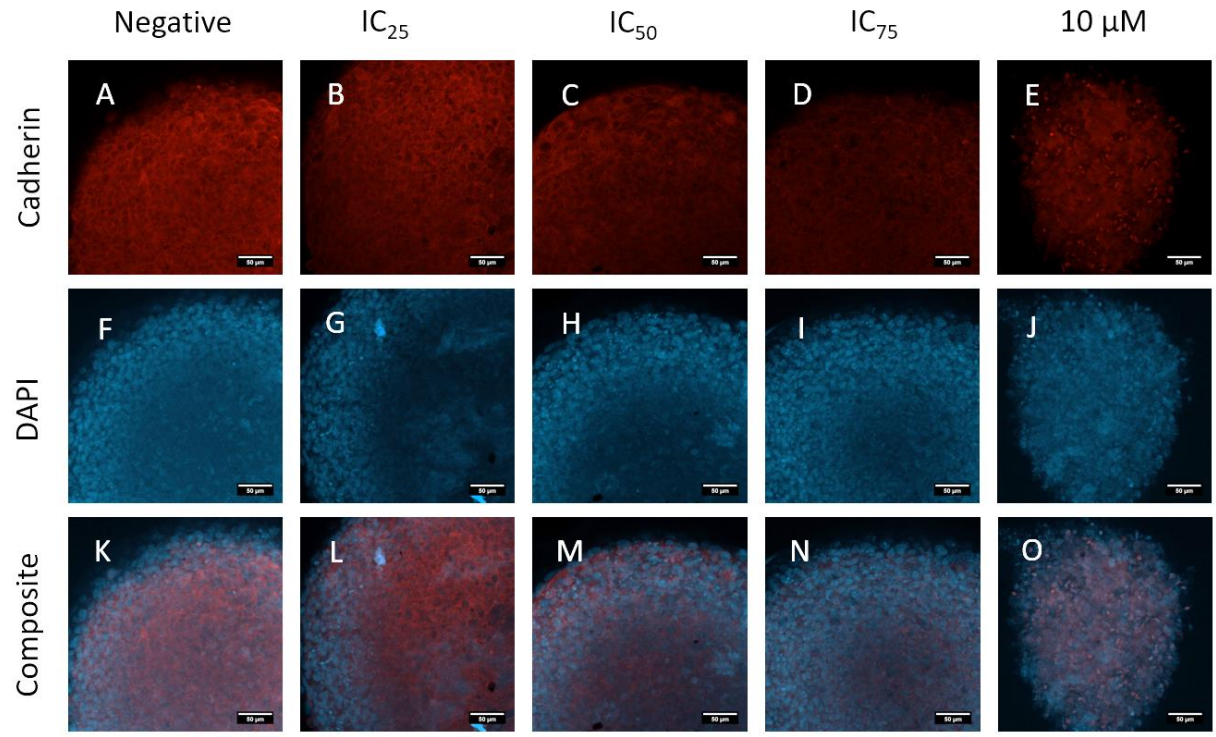

***Figure 3.25**: Representative confocal microscopy images of spheroids treated with various concentrations of doxorubicin for 72 h and stained with the ani-cadherin pAB (A-E), DAPI (F-J) and composite thereof (J-M). Images captured using a 20X air objective.*

Interestingly, Ki-67 staining was not pronounced within the spheroid, suggesting that the proliferative capacity of cells within BT-20 spheroids differs from that in 2D monolayer cultures, as supported by the spheroid protein content data. However, further quantitative evaluation needs to be performed to conclusively demonstrate this. A few brightly stained cells were visible in the spheroid indicating the presence of mitotic cells (Figure 3.26 A-E). The number of these bright spots increased slightly as the concentration of doxorubicin increased, up to the IC_{75}. At 10 µM spheroid size diminished while a large number of intensely bright cells were seen throughout the spheroid (Figure 3.26 E). This seemed to be a paradoxical effect, as Ki-67 stains proliferating cells. The Ki-67 protein is transiently expressed during cell growth, and the levels of the protein are highest during the G2/M phase of the cell cycle.[204] Doxorubicin exerts its cytotoxic effect by inducing a cell cycle arrest at the G2/M phase.[249] It is, therefore, likely that the observed staining of Ki-67 in spheroids treated with 10 µM doxorubicin does not represent a proliferative effect but indicates a cell cycle arrest before the cells became apoptotic.

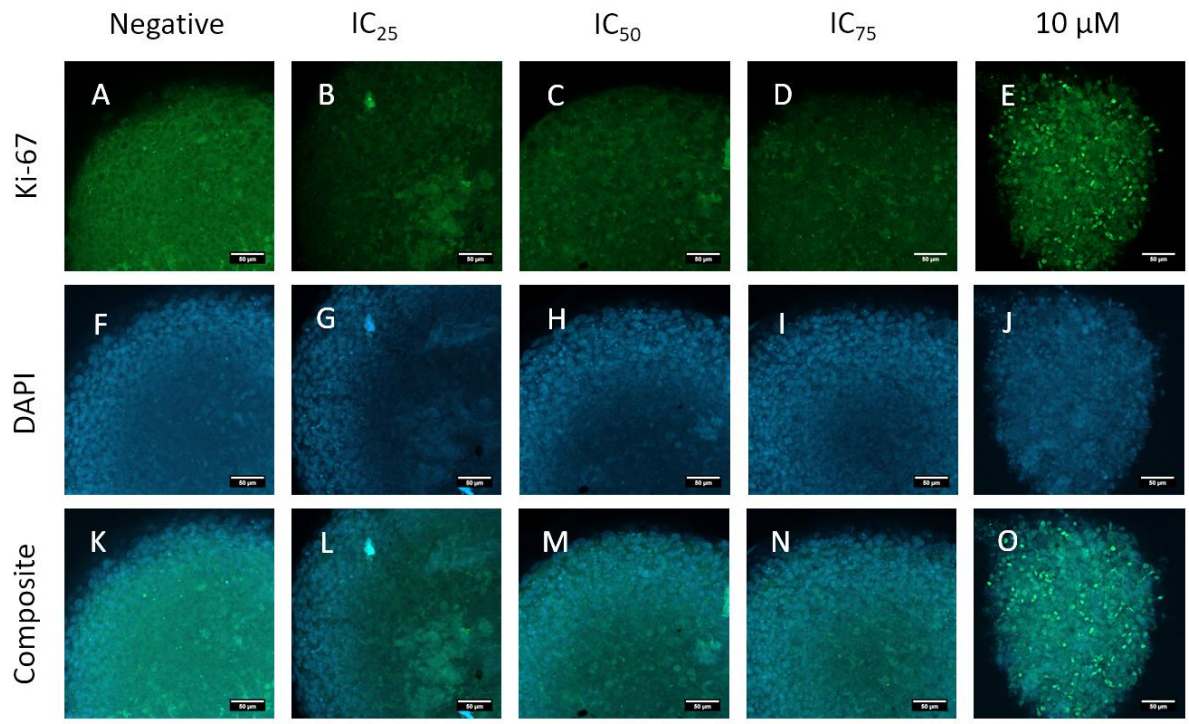

Figure 3.26 *Representative confocal microscopy images of spheroids treated with various concentrations of doxorubicin for 72 h and stained with the Alexa Fluor® 488-conjugated anti-Ki 67 mAB(A-E), DAPI (F-J) and a composite thereof (J-M). Image captured using a 20X air objective lens. Scale bar = 50 µm.*

Though the results presented here are still preliminary, the Clear^{T2} clearing protocol allowed for in-depth imaging of cells within the multicellular spheroids, without the need to conduct laborious, and potentially structurally disruptive techniques. Similar to previously reports,[184] antigens were preserved after clearing and, therefore, the clearing protocol is an ideal platform for the imaging of multicellular spheroids as it maintains the original morphology of the sample. Use of the technique in future could aid in the further characterisation of the spatial phenotypic features, and elucidation of the aspects that contribute to the increased chemoresistance of the BT-20 triple-negative breast cancer spheroid model.

Chapter 4: Conclusions and recommendations

4.1 Conclusions

Patients with TNBC have poor clinical outcomes compared to those with other breast cancer subtypes, and this is attributed to the inherent aggressiveness and lack of optimally-characterized molecular aberrations associated with this cancer type. The aggressiveness, survival, and chemoresistance of cancer cells can largely be attributed to various molecular cues within the tumuoral niche, and characterisation of such cues could aid in the identification of new compounds for the effective treatment of cancers demonstrating poor prognostic outcomes such as TNBC. Multicellular spheroids can be used as a physiologically relevant platform for the characterisation of biological traits of the tumour microenvironment, as the model circumvents some of the limitations associated with the traditional monolayer cell culture and animal models. The aim of the current study was, therefore, to grow then characterize the spatial morphometric features, and to determine the chemosensitivity of a TNBC spheroid model using the BT-20 cell line.

The hanging drop and liquid overlay techniques were compared to select a platform for the reproducible generation of spheroids. Only loose, irregularly-shaped aggregates formed with the hanging drop technique, while reproducibly circular and dense spheroids formed with the liquid overlay method. The liquid overlay technique was therefore chosen for the further characterisation of the spheroid model.

The accuracy of automated spheroid size analysis software programs in comparison to manual measurements was done to validate methods for high-throughput automatic measurement of spheroid diameter and volume. There was no significant difference in the spheroid volume measured using either the SpheroidSizer or an ImageJ macro compared to manual measurements, thus reinforcing the validity of both programs in the measurement of spheroid volume. The spheroids significantly decreased in size over the growth period, suggesting continuing compaction. The protein content increased, and this confirmed that the decrease in spheroid size was mainly due to compaction rather than cell death. However, the fold-change in protein content was lower than what would be expected if the cells maintained the growth rates demonstrated by monolayer cultures, suggesting the reduction of proliferative potential when the cells are propagated as multicellular spheroids.

Investigation of the viability of intact spheroids suggested that the outer spheroid regions consisted of metabolically active cells, while membrane-compromised cells were confined to the inner regions. This observation corroborated with histological analysis of paraffin-embedded spheroid sections, which revealed an outer spheroid rim consisting of large cells, and a central core with seemingly necrotic cells. The spatial heterogeneity of the morphology of spheroids can be a consequence of the alteration of varying physiological parameters within spheroids, with hypoxia a chief-mediator of such differentiation. Staining for hypoxia using a fluorescent probe indicated the inherent induction of hypoxic regions within multicellular spheroids, while hypoxia was not detected in monolayer cultures.

Cancer cells can adapt to hypoxic conditions to promote the emergence of a population with a more aggressive and potentially chemoresistant phenotype. The *in vitro* efficacy of doxorubicin, a clinically approved cytotoxic compound was compared using monolayer and spheroid cultures. The monolayers were sensitive to doxorubicin at widely reported concentration ranges. Within these concentrations, doxorubicin significantly reduced the cell density, viability, and acid phosphatase activity, while the volume and acid phosphatase activity were not significantly affected in spheroids. The volume, structural integrity and enzymatic activity of spheroids were only altered at high concentrations of doxorubicin, indicating increased chemoresistance of the spheroid model compared to the monolayer counterpart.

Many mechanisms can contribute to the resistance of multicellular spheroids to cytotoxic compounds, however, methods to investigate the alteration of physiological parameters within the 3D structures are currently limited. Many analytical methods that were originally designed to meet the requirements for monolayer culture evaluation fail to reveal the original biology of multicellular spheroids. As proof of concept, optical clearing was, therefore, used to make doxorubicin-treated spheroids transparent, prior to confocal microscopic imaging of cadherins and the Ki-67 antigens.

Optical clearing of treated and untreated spheroids allowed for the visualization of the internal spatial distribution of the cadherin and Ki-67 proteins. High concentrations of doxorubicin (compared to the monolayer IC_{50}) led to a reduction in cadherin staining, indicating that doxorubicin resulted in alteration of intercellular adhesive properties at these high doxorubicin concentrations. The Ki-67 staining was not profound,

suggesting a reduction of cell cycle progression when BT-20 cells are propagated as spheroids. At high concentrations of doxorubicin, many mitotic cells were identified, suggesting that the drug induced a G2/M phase cell cycle arrest in the spheroids.

In summary, the BT-20 spheroid model presented here exhibits reduced chemosensitivity to doxorubicin compared to the monolayer counterpart. This attenuated response to a commonly used chemotherapeutic compound could be linked to the spatial heterogeneity of cytoarchitecture and biochemical features such as hypoxia and viability within the BT-20 spheroids. The *in vivo* tumour micromilieu is heterogeneous with respect to cellular morphology, and O_2 and nutrient gradients, and spheroids are generally considered as a robust platform for the *in vitro* recapitulation such microenvironmental cues. Compared to monolayers, BT-20 spheroids could, therefore, potentially be adopted as a more relevant model for screening new drugs against TNBC. However, further investigation of the dynamics of spheroid formation, mechanisms underlying chemoresistance, and the therapeutic sensitivity to a wider panel of antineoplastic drugs is required to further characterise the model.

4.2 Limitations and recommendations

In the current study, only the epithelial BT-20 cell line was used to generate spheroids. However, various cell types such as fibroblasts and immune cells exist within the tumuoral niche. Co-culturing cancer cells with different cell types in future can aid in enhancing the *in vitro* recapitulation of the TME and could reveal the dynamics of intricate interactions of different cellular types within tumour spheroids.[263] Additionally, despite the focus of the study on the TNBC subtype, the behaviour of spheroids grown from other subtypes could be quite distinct. It would be of great interest, therefore, to grow spheroids of other hormone dependant breast cancer cell lines in parallel with BT-20 cells, in order to elucidate the biochemical and chemosensitivity attributes that are unique to the TNBC subtype.

Stationary platforms for the generation of multicellular spheroids such as the liquid overlay method are associated with some limitations. These limitations are primarily due to a more diffusion-limited environment relative to dynamic platforms such as bioreactors.[187] This diffusion limitation affects the nutrient supply, pathological attributes, and drug distribution in spheroids. Dynamic rotary cell culture systems circumvent these limitations, and they allow for adequate perfusion and long-term culturing. An additional advantage of the dynamic spheroid generation methods such as clinostat bioreactors is that they allow for the reproducible generation of uniform spheroids, which are equally exposed to very low shear forces.[264] Future work will, therefore, focus on adopting such dynamic cell culture systems in the further characterisation of BT-20 spheroids.

The cell density used in the study is higher than what is typically used in the hanging-drop technique, which introduces bias when comparing the assay to the liquid overlay method. Replenishment of medium within the hanging drop technique within the first four days after initial seeding could have accounted for this disparity. Additionally, it would have been more appropriate to investigate different titrations of cell numbers in order to actually see the power and capability of each assay to form spheroids. The titration of seeding densities can also allow for the investigation of the minimal diameter at which the development of attributes such as hypoxia and centralised necrosis are initiated.

Alteration of proliferative rates in spheroids, compared to monolayers was speculated, however, not conclusively demonstrated. Measurement of protein content on the day of seeding can allow for the investigation of the kinetics of cell division occurring prior to compaction and reduction of the doubling time. Additionally, imaging the spheroids at earlier time-points (i.e., within the first three days from initial seeding), would allow for the investigation of the dynamics of spheroid formation.

In comparing the cytotoxicity of doxorubicin in monolayers to spheroids, it would be ideal to expose the drug to an equal number of cells, to ensure that any differential drug response is ascribed to the culture format rather than unequal cell numbers. Monolayers were only allowed to attach for 24 h, while spheroids were grown for four days before drug exposure. The inherent difficulty in quantifying cell numbers in spheroids makes it difficult to determine whether there was a notable difference in drug exposure per cell in spheroids compared to monolayers, as cell numbers in spheroids could have increased by Day 4. In future, it might be beneficial to measure the “Day 0” protein content of cells before propagation as spheroids (essentially monolayers at that point), as this will allow for elucidation of the extent of change in the amount of cells by the time of drug exposure by Day 4, and ensuring that both models are exposed to relatively the same amount of drug per cell.

Though the chemosensitivity of the BT-20 spheroids was investigated in this study, only one drug was used, which is not sufficient to provide a basis for predicting the therapeutic response to new chemical entities. In order for the model to be confidently used in predicting such responses, validation studies that entail investigating the sensitivity of various clinically-established drugs with different mechanisms of action would need to be conducted. Not only will this render a platform for investigating the efficacy of novel compounds with various postulated mechanisms of action, but comparison with the clinical response could also be done.

The optical clearing and confocal images presented here are still preliminary and not conclusive, however, further optimisation of the protocol is currently underway at the University of Pretoria’s Centre for Neuroendocrinology. Once fully optimised, this will potentially allow for the investigation of the spatial differences in additional components of the cells such as the ECM and cytoskeleton across the spheroid. Investigation of the alteration of other markers such as caspase-3 using confocal

microscopy could also allow for the investigation of other mechanisms underlying the chemoresistance of the spheroids.

Finally, confocal microscopy and other imaging modalities used in the current study rely on the detection of labelled moieties, which hampers the discovery of any molecular alterations in an unbiased fashion. Though associated with many sample preparation challenges, MALDI and laser ablation inductively coupled plasma MSI[265] methods could be adopted in the future, to spatially resolve any molecular alterations that could be implicated in the observed attributes of the BT-20 spheroids.

References

1. Shaltiel IA, Krenning L, Bruinsma W, Medema RH. The same, only different–DNA damage checkpoints and their reversal throughout the cell cycle. Journal of Cell Science. 2015;128(4):607-20.

2. O'Connor MJ. Targeting the DNA damage response in cancer. Molecular Cell. 2015;60(4):547-60.

3. Jackson SP, Bartek J. The DNA-damage response in human biology and disease. Nature. 2009;461(7267):1071.

4. Hanahan D, Weinberg RA. The hallmarks of cancer. Cell. 2000;100(1):57-70.

5. Bray F, Ferlay J, Soerjomataram I, Siegel RL, Torre LA, Jemal A. Global cancer statistics 2018: GLOBOCAN estimates of incidence and mortality worldwide for 36 cancers in 185 countries. CA: a Cancer Journal for Clinicians. 2018;68(6):394-424.

6. Torre LA, Bray F, Siegel RL, Ferlay J, Lortet-Tieulent J, Jemal A. Global cancer statistics, 2012. CA: a Cancer Journal for Clinicians. 2015;65(2):87-108.

7. Zheng Y, Walsh T, Gulsuner S, Casadei S, Lee MK, Ogundiran TO, Ademola A, Falusi AG, Adebamowo CA, Oluwasola AO. Inherited breast cancer in Nigerian women. Journal of Clinical Oncology. 2018;36(28):2820-5.

8. Montazeri Z, Nyiraneza C, El-Katerji H, Little J. Waterpipe smoking and cancer: systematic review and meta-analysis. Tobacco Control. 2017;26(1):92-7.

9. Brown JC, Winters-Stone K, Lee A, Schmitz KH. Cancer, physical activity, and exercise. Comprehensive Physiology. 2012;2(4):2775-809.

10. Adlercreutz H. Western diet and Western diseases: some hormonal and biochemical mechanisms and associations. Scandinavian Journal of Clinical and Laboratory Investigation. 1990;50(sup201):3-23.

11. Wu S, Zhu W, Thompson P, Hannun YA. Evaluating intrinsic and non-intrinsic cancer risk factors. Nature Communications. 2018;9(1):3490.

12. Ferlay J, Shin HR, Bray F, Forman D, Mathers C, Parkin DM. Estimates of worldwide burden of cancer in 2008: GLOBOCAN 2008. International Journal of Cancer. 2010;127(12):2893-917.

13. Hanahan D, Weinberg RA. Hallmarks of cancer: the next generation. Cell. 2011;144(5):646-74.

14. Cheng N, Chytil A, Shyr Y, Joly A, Moses HL. Transforming growth factor-β signaling–deficient fibroblasts enhance hepatocyte growth factor signaling in

mammary carcinoma cells to promote scattering and invasion. Molecular Cancer Research. 2008;6(10):1521-33.
15. Iqbal N, Iqbal N. Human epidermal growth factor receptor 2 (HER2) in cancers: overexpression and therapeutic implications. Molecular Biology International. 2014;2014.
16. Feitelson MA, Arzumanyan A, Kulathinal RJ, Blain SW, Holcombe RF, Mahajna J, Marino M, Martinez-Chantar ML, Nawroth R, Sanchez-Garcia I, editors. Sustained proliferation in cancer: Mechanisms and novel therapeutic targets. Seminars in Cancer Biology; 2015.S25-S54.
17. Burkhart DL, Sage J. Cellular mechanisms of tumour suppression by the retinoblastoma gene. Nature Reviews Cancer. 2008;8(9):671.
18. Vélez-Cruz R, Johnson DG. The retinoblastoma (RB) tumor suppressor: pushing back against genome instability on multiple fronts. International Journal of Molecular Sciences. 2017;18(8):1776.
19. Bieging KT, Mello SS, Attardi LD. Unravelling mechanisms of p53-mediated tumour suppression. Nature Reviews Cancer. 2014;14(5):359.
20. Evan GI, Vousden KH. Proliferation, cell cycle and apoptosis in cancer. Nature. 2001;411(6835):342.
21. Mohammad RM, Muqbil I, Lowe L, Yedjou C, Hsu H-Y, Lin L-T, Siegelin MD, Fimognari C, Kumar NB, Dou QP, editors. Broad targeting of resistance to apoptosis in cancer. Seminars in Cancer Biology; 2015.S78-S103.
22. Fernald K, Kurokawa M. Evading apoptosis in cancer. Trends in Cell Biology. 2013;23(12):620-33.
23. Fulda S. Tumor resistance to apoptosis. International Journal of Cancer. 2009;124(3):511-5.
24. Wuilleme-Toumi S, Robillard N, Gomez P, Moreau P, Le Gouill S, Avet-Loiseau H, Harousseau J, Amiot M, Bataille R. Mcl-1 is overexpressed in multiple myeloma and associated with relapse and shorter survival. Leukemia. 2005;19(7):1248.
25. Matsuura K, Huang N, Cocce K, Zhang L, Kornbluth S. Downregulation of the proapoptotic protein MOAP-1 by the UBR5 ubiquitin ligase and its role in ovarian cancer resistance to cisplatin. Oncogene. 2017;36(12):1698.
26. Jafri MA, Ansari SA, Alqahtani MH, Shay JW. Roles of telomeres and telomerase in cancer, and advances in telomerase-targeted therapies. Genome Medicine. 2016;8(1):69.

27. Harley CB, Futcher AB, Greider CW. Telomeres shorten during ageing of human fibroblasts. Nature. 1990;345(6274):458.
28. Muñoz-Espín D, Serrano M. Cellular senescence: from physiology to pathology. Nature Reviews Molecular Cell Biology. 2014;15(7):482.
29. McHugh D, Gil J. Senescence and aging: Causes, consequences, and therapeutic avenues. Journal of Cell Biology. 2018;217(1):65-77.
30. Hayashi MT, Cesare AJ, Rivera T, Karlseder J. Cell death during crisis is mediated by mitotic telomere deprotection. Nature. 2015;522(7557):492.
31. Fouad YA, Aanei C. Revisiting the hallmarks of cancer. American Journal of Cancer Research. 2017;7(5):1016.
32. Folkman J. Tumor angiogenesis: therapeutic implications. New England Journal of Medicine. 1971;285(21):1182-6.
33. De Palma M, Biziato D, Petrova TV. Microenvironmental regulation of tumour angiogenesis. Nature Reviews Cancer. 2017;17(8):457.
34. Manalo DJ, Rowan A, Lavoie T, Natarajan L, Kelly BD, Shui QY, Garcia JG, Semenza GL. Transcriptional regulation of vascular endothelial cell responses to hypoxia by HIF-1. Blood. 2005;105(2):659-69.
35. Kieran MW, Kalluri R, Cho Y-J. The VEGF pathway in cancer and disease: responses, resistance, and the path forward. Cold Spring Harbor Perspectives in Medicine. 2012:a006593.
36. Seyfried TN, Huysentruyt LC. On the origin of cancer metastasis. Critical Reviews in Oncogenesis. 2013;18(1-2):43.
37. Stuelten CH, Parent CA, Montell DJ. Cell motility in cancer invasion and metastasis: Insights from simple model organisms. Nature Reviews Cancer. 2018.
38. Onder TT, Gupta PB, Mani SA, Yang J, Lander ES, Weinberg RA. Loss of E-cadherin promotes metastasis via multiple downstream transcriptional pathways. Cancer Research. 2008;68(10):3645-54.
39. Qian X, Anzovino A, Kim S, Suyama K, Yao J, Hulit J, Agiostratidou G, Chandiramani N, McDaid H, Nagi C. N-cadherin/FGFR promotes metastasis through epithelial-to-mesenchymal transition and stem/progenitor cell-like properties. Oncogene. 2014;33(26):3411.
40. Karlsson MC, Gonzalez SF, Welin J, Fuxe J. Epithelial-mesenchymal transition in cancer metastasis through the lymphatic system. Molecular Oncology. 2017;11(7):781-91.

41. Yao Y, Dai W. Genomic instability and cancer. Journal of Carcinogenesis & Mutagenesis. 2014;5.
42. Coussens LM, Werb Z. Inflammation and cancer. Nature. 2002;420(6917):860.
43. Vinay DS, Ryan EP, Pawelec G, Talib WH, Stagg J, Elkord E, Lichtor T, Decker WK, Whelan RL, Kumara HS, editors. Immune evasion in cancer: Mechanistic basis and therapeutic strategies. Seminars in Cancer Biology; 2015.S185-S98.
44. Jeon S-M, Hay N. Expanding the concepts of cancer metabolism. Nature Publishing Group; 2018.
45. Ferlay J, Soerjomataram I, Dikshit R, Eser S, Mathers C, Rebelo M, Parkin DM, Forman D, Bray F. Cancer incidence and mortality worldwide: sources, methods and major patterns in GLOBOCAN 2012. International Journal of Cancer. 2015;136(5).
46. Kamińska M, Ciszewski T, Łopacka-Szatan K, Miotła P, Starosławska E. Breast cancer risk factors. Menopause Review. 2015;14(3):196.
47. Gnerlich JL, Deshpande AD, Jeffe DB, Seelam S, Kimbuende E, Margenthaler JA. Poorer survival outcomes for male breast cancer compared with female breast cancer may be attributable to in-stage migration. Annals of Surgical Oncology. 2011;18(7):1837-44.
48. Siegel RL, Miller KD, Jemal A. Cancer statistics, 2017. CA: a Cancer Journal for Clinicians. 2017;67(1):7-30.
49. Sun Y-S, Zhao Z, Yang Z-N, Xu F, Lu H-J, Zhu Z-Y, Shi W, Jiang J, Yao P-P, Zhu H-P. Risk factors and preventions of breast cancer. International Journal of Biological Sciences. 2017;13(11):1387.
50. Iqbal J, Ginsburg O, Rochon PA, Sun P, Narod SA. Differences in breast cancer stage at diagnosis and cancer-specific survival by race and ethnicity in the United States. Jama. 2015;313(2):165-73.
51. Ban KA, Godellas CV. Epidemiology of breast cancer. Surgical Oncology Clinics of North America. 2014;23(3):409-22.
52. Kuchenbaecker KB, Hopper JL, Barnes DR, Phillips K-A, Mooij TM, Roos-Blom M-J, Jervis S, Van Leeuwen FE, Milne RL, Andrieu N. Risks of breast, ovarian, and contralateral breast cancer for BRCA1 and BRCA2 mutation carriers. Journal of the American Medical Association. 2017;317(23):2402-16.
53. Scully R, Livingston DM. In search of the tumour-suppressor functions of BRCA1 and BRCA2. Nature. 2000;408(6811):429.

54. Cancer CGoHFiB. Menarche, menopause, and breast cancer risk: individual participant meta-analysis, including 118 964 women with breast cancer from 117 epidemiological studies. The Lancet Oncology. 2012;13(11):1141-51.
55. Libson S, Lippman M. A review of clinical aspects of breast cancer. International Review of Psychiatry. 2014;26(1):4-15.
56. Mørch LS, Skovlund CW, Hannaford PC, Iversen L, Fielding S, Lidegaard Ø. Contemporary hormonal contraception and the risk of breast cancer. New England Journal of Medicine. 2017;377(23):2228-39.
57. Collaborators MWS. Breast cancer and hormone-replacement therapy in the Million Women Study. The Lancet. 2003;362(9382):419-27.
58. Chlebowski RT, Kuller LH, Prentice RL, Stefanick ML, Manson JE, Gass M, Aragaki AK, Ockene JK, Lane DS, Sarto GE. Breast cancer after use of estrogen plus progestin in postmenopausal women. New England Journal of Medicine. 2009;360(6):573-87.
59. Mobarakeh ZS, Mirzaei K, Hatmi N, Ebrahimi M, Dabiran S, Sotoudeh G. Dietary habits contributing to breast cancer risk among Iranian women. Asian Pacific Journal of Cancer Prevention. 2014;15(21):9543-7.
60. Picon-Ruiz M, Morata-Tarifa C, Valle-Goffin JJ, Friedman ER, Slingerland JM. Obesity and adverse breast cancer risk and outcome: mechanistic insights and strategies for intervention. CA: a Cancer Journal for Clinicians. 2017;67(5):378-97.
61. Bagnardi V, Rota M, Botteri E, Tramacere I, Islami F, Fedirko V, Scotti L, Jenab M, Turati F, Pasquali E. Light alcohol drinking and cancer: a meta-analysis. Annals of Oncology. 2012;24(2):301-8.
62. Bauer SR, Hankinson SE, Bertone-Johnson ER, Ding EL. Plasma vitamin D levels, menopause, and risk of breast cancer: dose-response meta-analysis of prospective studies. Medicine. 2013;92(3):123.
63. Milioli HH, Vimieiro R, Riveros C, Tishchenko I, Berretta R, Moscato P. The discovery of novel biomarkers improves breast cancer intrinsic subtype prediction and reconciles the labels in the metabric data set. PloS One. 2015;10(7):e0129711.
64. Reis-Filho JS, Pusztai L. Gene expression profiling in breast cancer: classification, prognostication, and prediction. The Lancet. 2011;378(9805):1812-23.
65. Yersal O, Barutca S. Biological subtypes of breast cancer: Prognostic and therapeutic implications. World Journal of Clinical Oncology. 2014;5(3):412.

66. Dai X, Li T, Bai Z, Yang Y, Liu X, Zhan J, Shi B. Breast cancer intrinsic subtype classification, clinical use and future trends. American Journal of Cancer Research. 2015;5(10):2929.
67. Rouzier R, Perou CM, Symmans WF, Ibrahim N, Cristofanilli M, Anderson K, Hess KR, Stec J, Ayers M, Wagner P. Breast cancer molecular subtypes respond differently to preoperative chemotherapy. Clinical Cancer Research. 2005;11(16):5678-85.
68. Li J, Chen Z, Su K, Zeng J. Clinicopathological classification and traditional prognostic indicators of breast cancer. International Journal of Clinical and Experimental Pathology. 2015;8(7):8500.
69. Bauer KR, Brown M, Cress RD, Parise CA, Caggiano V. Descriptive analysis of estrogen receptor (ER)-negative, progesterone receptor (PR)-negative, and HER2-negative invasive breast cancer, the so-called triple-negative phenotype. Cancer. 2007;109(9):1721-8.
70. Harvey JM, Clark GM, Osborne CK, Allred DC. Estrogen receptor status by immunohistochemistry is superior to the ligand-binding assay for predicting response to adjuvant endocrine therapy in breast cancer. Journal of Clinical Oncology. 1999;17(5):1474-81.
71. Rakha EA, Green AR. Molecular classification of breast cancer: what the pathologist needs to know. Pathology. 2017;49(2):111-9.
72. Kelsey JL, Gammon MD, John EM. Reproductive factors and breast cancer. Epidemiologic Reviews. 1993;15(1):36.
73. Yaşar P, Ayaz G, User SD, Güpür G, Muyan M. Molecular mechanism of estrogen–estrogen receptor signaling. Reproductive Medicine and Biology. 2017;16(1):4-20.
74. Deroo BJ, Korach KS. Estrogen receptors and human disease. The Journal of Clinical Investigation. 2006;116(3):561-70.
75. Hilton HN, Clarke CL, Graham JD. Estrogen and progesterone signalling in the normal breast and its implications for cancer development. Molecular and Cellular Endocrinology. 2017;466:2-14.
76. Ellmann S, Sticht H, Thiel F, Beckmann MW, Strick R, Strissel PL. Estrogen and progesterone receptors: from molecular structures to clinical targets. Cellular and Molecular Life Sciences. 2009;66(15):2405-26.
77. Conneely OM, Mulac-Jericevic B, Lydon JP. Progesterone-dependent regulation of female reproductive activity by two distinct progesterone receptor isoforms. Steroids. 2003;68(10-13):771-8.

78. Lange CA, Yee D. Progesterone and breast cancer. Women's Health. 2008;4(2):151-62.
79. Poole AJ, Li Y, Kim Y, Lin S-CJ, Lee W-H, Eva Y-HL. Prevention of Brca1-mediated mammary tumorigenesis in mice by a progesterone antagonist. Science. 2006;314(5804):1467-70.
80. Robertson J, Willsher P, Winterbottom L, Blamey R, Thorpe S. Onapristone, a progesterone receptor antagonist, as first-line therapy in primary breast cancer. European Journal of Cancer. 1999;35(2):214-8.
81. Davaadelger B, Murphy AR, Clare SE, Lee O, Khan SA, Kim JJ. Mechanism of telapristone acetate (CDB4124) on progesterone receptor action in breast cancer cells. Endocrinology. 2018;159(10):3581-95.
82. Burstein HJ. The distinctive nature of HER2-positive breast cancers. New England Journal of Medicine. 2005;353(16):1652-4.
83. Kallioniemi O-P, Kallioniemi A, Kurisu W, Thor A, Chen L-C, Smith HS, Waldman FM, Pinkel D, Gray JW. ERBB2 amplification in breast cancer analyzed by fluorescence in situ hybridization. Proceedings of the National Academy of Sciences. 1992;89(12):5321-5.
84. Nitta H, Kelly BD, Allred C, Jewell S, Banks P, Dennis E, Grogan TM. The assessment of HER2 status in breast cancer: the past, the present, and the future. Pathology International. 2016;66(6):313-24.
85. Schmadeka R, Harmon BE, Singh M. Triple-negative breast carcinoma. American Journal of Clinical Pathology. 2014;141(4):462-77.
86. Dunnwald LK, Rossing MA, Li CI. Hormone receptor status, tumor characteristics, and prognosis: a prospective cohort of breast cancer patients. Breast Cancer Research. 2007;9(1):R6.
87. Eliyatkın N, Yalçın E, Zengel B, Aktaş S, Vardar E. Molecular classification of breast carcinoma: from traditional, old-fashioned way to a new age, and a new way. The Journal of Breast Health. 2015;11(2):59.
88. Network CGA. Comprehensive molecular portraits of human breast tumours. Nature. 2012;490(7418):61.
89. Hon JDC, Singh B, Sahin A, Du G, Wang J, Wang VY, Deng F-M, Zhang DY, Monaco ME, Lee P. Breast cancer molecular subtypes: from TNBC to QNBC. American Journal of Cancer Research. 2016;6(9):1864.

90. Livasy CA, Karaca G, Nanda R, Tretiakova MS, Olopade OI, Moore DT, Perou CM. Phenotypic evaluation of the basal-like subtype of invasive breast carcinoma. Modern Pathology. 2006;19(2):264.
91. Kreike B, van Kouwenhove M, Horlings H, Weigelt B, Peterse H, Bartelink H, van de Vijver MJ. Gene expression profiling and histopathological characterization of triple-negative/basal-like breast carcinomas. Breast Cancer Research. 2007;9(5):R65.
92. Dent R, Trudeau M, Pritchard KI, Hanna WM, Kahn HK, Sawka CA, Lickley LA, Rawlinson E, Sun P, Narod SA. Triple-negative breast cancer: clinical features and patterns of recurrence. Clinical Cancer Research. 2007;13(15):4429-34.
93. Newman LA, Kaljee LM. Health disparities and triple-negative breast cancer in African American women: a review. Journal of the American Medical Association Surgery. 2017;152(5):485-93.
94. Schmadeka R, Harmon BE, Singh M. Triple-negative breast carcinoma: current and emerging concepts. American Journal of Clinical Pathology. 2014;141(4):462-77.
95. O'Reilly EA, Gubbins L, Sharma S, Tully R, Guang MHZ, Weiner-Gorzel K, McCaffrey J, Harrison M, Furlong F, Kell M. The fate of chemoresistance in triple negative breast cancer (TNBC). Biochimica et Biophysica Acta Clinical. 2015;3:257-75.
96. Lehmann BD, Bauer JA, Chen X, Sanders ME, Chakravarthy AB, Shyr Y, Pietenpol JA. Identification of human triple-negative breast cancer subtypes and preclinical models for selection of targeted therapies. The Journal of Clinical Investigation. 2011;121(7):2750-67.
97. Marmé F, Schneeweiss A. Targeted therapies in triple-negative breast cancer. Breast care. 2015;10(3):159-66.
98. Sharma P. Update on the treatment of early-stage triple-negative breast cancer. Current Treatment Options in Oncology. 2018;19(5):22.
99. Lebert J, Lester R, Powell E, Seal M, McCarthy J. Advances in the systemic treatment of triple-negative breast cancer. Current Oncology. 2018;25(Suppl 1):S142-S50.
100. de Weger VA, Beijnen JH, Schellens JH. Cellular and clinical pharmacology of the taxanes docetaxel and paclitaxel–a review. Anti-Cancer Drugs. 2014;25(5):488-94.
101. Emadi A, Jones RJ, Brodsky RA. Cyclophosphamide and cancer: golden anniversary. Nature Reviews Clinical Oncology. 2009;6(11):638-47.

102. Tacar O, Sriamornsak P, Dass CR. Doxorubicin: an update on anticancer molecular action, toxicity and novel drug delivery systems. Journal of Pharmacy and Pharmacology. 2013;65(2):157-70.
103. Bhattacharjee J, Verma G, Aswal V, Hassan P. Small angle neutron scattering study of doxorubicin-surfactant complexes encapsulated in block copolymer micelles. Pramana. 2008;71(5):991-5.
104. Untch M, Schneeweiss A, Salat C, Rezai M, Zahm DM, Klare P, Blohmer JU, Tesch H, Khandan F, Fasching P. 163PDLong-term survival analysis of the randomized phase II trial investigating the addition of carboplatin to neoadjuvant therapy for triple-negative (TNBC) and HER2-positive early breast cancer (GeparSixto). Annals of Oncology. 2017;28(suppl_5).
105. Denkert C, Liedtke C, Tutt A, von Minckwitz G. Molecular alterations in triple-negative breast cancer—the road to new treatment strategies. The Lancet. 2017;389(10087):2430-42.
106. Carey LA, Dees EC, Sawyer L, Gatti L, Moore DT, Collichio F, Ollila DW, Sartor CI, Graham ML, Perou CM. The triple negative paradox: primary tumor chemosensitivity of breast cancer subtypes. Clinical Cancer Research. 2007;13(8):2329-34.
107. Hutchinson L, Kirk R. High drug attrition rates—where are we going wrong? Nature Reviews Clinical Oncology. 2011;8:189-90.
108. Begley CG, Ellis LM. Drug development: Raise standards for preclinical cancer research. Nature. 2012;483(7391):531-3.
109. Lombardino JG, Lowe III JA. A guide to drug discovery: the role of the medicinal chemist in drug discovery—then and now. Nature Reviews Drug Discovery. 2004;3(10):853.
110. Nixon NA, Khan OF, Imam H, Tang PA, Monzon J, Li H, Sun G, Ezeife D, Parimi S, Dowden S. Drug development for breast, colorectal, and non–small cell lung cancers from 1979 to 2014. Cancer. 2017;123(23):4672-9.
111. Yildirim O, Gottwald M, Schüler P, Michel MC. Opportunities and challenges for drug development: public–private partnerships, adaptive designs and big data. Frontiers in Pharmacology. 2016;7:461.
112. Balkwill FR, Capasso M, Hagemann T. The tumor microenvironment at a glance. Journal of Cell Science. 2012;155:5591-6.

113. Wang M, Zhao J, Zhang L, Wei F, Lian Y, Wu Y, Gong Z, Zhang S, Zhou J, Cao K. Role of tumor microenvironment in tumorigenesis. Journal of Cancer. 2017;8(5):761.
114. Belli C, Trapani D, Viale G, D'Amico P, Duso BA, Della Vigna P, Orsi F, Curigliano G. Targeting the microenvironment in solid tumors. Cancer Treatment Reviews. 2018.
115. Petrova V, Annicchiarico-Petruzzelli M, Melino G, Amelio I. The hypoxic tumour microenvironment. Oncogenesis. 2018;7(1):10.
116. Eales K, Hollinshead K, Tennant D. Hypoxia and metabolic adaptation of cancer cells. Oncogenesis. 2016;5(1):e190.
117. Breslin S, O'Driscoll L. Three-dimensional cell culture: the missing link in drug discovery. Drug Discovery Today. 2013;18(5):240-9.
118. Lamichhane SP, Arya N, Kohler E, Xiang S, Christensen J, Shastri VP. Recapitulating epithelial tumor microenvironment *in vitro* using three dimensional tri-culture of human epithelial, endothelial, and mesenchymal cells. BioMed Central Cancer. 2016;16(1):581.
119. Alemany-Ribes M, Semino CE. Bioengineering 3D environments for cancer models. Advanced Drug Delivery Reviews. 2014;79:40-9.
120. Smalley KS, Lioni M, Herlyn M. Life ins't flat: Taking cancer biology to the next dimension. *In Vitro* Cellular & Developmental Biology-Animal. 2006;42(8-9):242-7.
121. Delarue M, Montel F, Vignjevic D, Prost J, Joanny J-F, Cappello G. Compressive stress inhibits proliferation in tumor spheroids through a volume limitation. Biophysical Journal. 2014;107(8):1821-8.
122. Kim JB, Stein R, O'Hare MJ. Three-dimensional *in vitro* tissue culture models of breast cancer—a review. Breast Cancer Research and Treatment. 2004;85(3):281-91.
123. Subarsky P, Hill RP. The hypoxic tumour microenvironment and metastatic progression. Clinical & Experimental Metastasis. 2003;20(3):237-50.
124. Asghar W, El Assal R, Shafiee H, Pitteri S, Paulmurugan R, Demirci U. Engineering cancer microenvironments for *in vitro* 3-D tumor models. Materials Today. 2015;18(10):539-53.
125. Wenzel C, Riefke B, Gründemann S, Krebs A, Christian S, Prinz F, Osterland M, Golfier S, Räse S, Ansari N, Esner M, Bickle M, Pampaloni F, Mattheyer C, Stelzer EH, Parczyk K, Prechtl S, Steigemann P. 3D high-content screening for the

identification of compounds that target cells in dormant tumor spheroid regions. Experimental Cell Research. 2014;323(1):131-43.
126. Freires IA, Sardi JdCO, de Castro RD, Rosalen PL. Alternative animal and non-animal models for drug discovery and development: bonus or burden? Pharmaceutical research. 2017;34(4):681-6.
127. Pampaloni F, Reynaud EG, Stelzer EH. The third dimension bridges the gap between cell culture and live tissue. Nature Reviews Molecular Cell Biology. 2007;8(10):839-45.
128. Friedrich J, Seidel C, Ebner R, Kunz-Schughart LA. Spheroid-based drug screen: considerations and practical approach. Nature Protocols. 2009;4(3):309-24.
129. Ivanov DP, Parker TL, Walker DA, Alexander C, Ashford MB, Gellert PR, Garnett MC. Multiplexing spheroid volume, resazurin and acid phosphatase viability assays for high-throughput screening of tumour spheroids and stem cell neurospheres. PloS One. 2014;9(8):e103817.
130. Ritter CA, Perez-Torres M, Rinehart C, Guix M, Dugger T, Engelman JA, Arteaga CL. Human breast cancer cells selected for resistance to trastuzumab in vivo overexpress epidermal growth factor receptor and ErbB ligands and remain dependent on the ErbB receptor network. Clinical Cancer Research. 2007;13(16):4909-19.
131. Nath S, Devi GR. Three-dimensional culture systems in cancer research: Focus on tumor spheroid model. Pharmacology & Therapeutics. 2016;163:94-108.
132. Esch EW, Bahinski A, Huh D. Organs-on-chips at the frontiers of drug discovery. Nature reviews Drug Discovery. 2015;14(4):248.
133. Albanese A, Lam AK, Sykes EA, Rocheleau JV, Chan WC. Tumour-on-a-chip provides an optical window into nanoparticle tissue transport. Nature Communications. 2013;4:2718.
134. Tsai H-F, Trubelja A, Shen AQ, Bao G. Tumour-on-a-chip: microfluidic models of tumour morphology, growth and microenvironment. Journal of the Royal Society Interface. 2017;14(131):20170137.
135. Yamada KM, Cukierman E. Modeling tissue morphogenesis and cancer in 3D. Cell. 2007;130(4):601-10.
136. Tibbitt MW, Anseth KS. Hydrogels as extracellular matrix mimics for 3D cell culture. Biotechnology and Bioengineering. 2009;103(4):655-63.

137. Nunes AS, Barros AS, Costa EC, Moreira AF, Correia IJ. 3D tumor spheroids as in vitro models to mimic in vivo human solid tumors resistance to therapeutic drugs. Biotechnology and Bioengineering. 2019;116(1):206-26.
138. Herrmann D, Conway JR, Vennin C, Magenau A, Hughes WG, Timpson P. Three-dimensional cancer models mimic cell-matrix interactions in the tumour microenvironment. Carcinogenesis. 2014;35(8):1671-9.
139. Mehta G, Hsiao AY, Ingram M, Luker GD, Takayama S. Opportunities and challenges for use of tumor spheroids as models to test drug delivery and efficacy. Journal of Controlled Release. 2012;164(2):192-204.
140. Kumar HR, Zhong X, Hoelz DJ, Rescorla FJ, Hickey RJ, Malkas LH, Sandoval JA. Three-dimensional neuroblastoma cell culture: proteomic analysis between monolayer and multicellular tumor spheroids. Pediatric Surgery International. 2008;24(11):1229.
141. Vaupel P, Kallinowski F, Okunieff P. Blood flow, oxygen and nutrient supply, and metabolic microenvironment of human tumors: a review. Cancer Research. 1989;49(23):6449-65.
142. Sutherland RM. Cell and environment interactions in tumor microregions: the multicell spheroid model. Science. 1988;240(4849):177.
143. Sutherland RM, McCredie JA, Inch WR. Growth of multicell spheroids in tissue culture as a model of nodular carcinomas. Journal of the National Cancer Institute. 1971;46(1):113-20.
144. Millard M, Yakavets I, Zorin V, Kulmukhamedova A, Marchal S, Bezdetnaya L. Drug delivery to solid tumors: the predictive value of the multicellular tumor spheroid model for nanomedicine screening. International Journal of Nanomedicine. 2017;12:7993-8007.
145. Anada T, Fukuda J, Sai Y, Suzuki O. An oxygen-permeable spheroid culture system for the prevention of central hypoxia and necrosis of spheroids. Biomaterials. 2012;33(33):8430-41.
146. Trédan O, Galmarini CM, Patel K, Tannock IF. Drug resistance and the solid tumor microenvironment. Journal of the National Cancer Institute. 2007;99(19):1441-54.
147. Swietach P, Hulikova A, Patiar S, Vaughan-Jones RD, Harris AL. Importance of intracellular pH in determining the uptake and efficacy of the weakly basic chemotherapeutic drug, doxorubicin. PloS One. 2012;7(4):e35949.

148. Saggar JK, Yu M, Tan Q, Tannock IF. The tumor microenvironment and strategies to improve drug distribution. Ways to Improve Tumor Uptake and Penetration of Drugs into Solid Tumors. 20148:8.
149. Aguirre-Ghiso JA. Models, mechanisms and clinical evidence for cancer dormancy. Nature Reviews Cancer. 2007;7(11):834-46.
150. Sosa MS, Bragado P, Aguirre-Ghiso JA. Mechanisms of disseminated cancer cell dormancy: an awakening field. Nature Reviews Cancer. 2014;14(9):611-22.
151. Lacroix M. Significance, detection and markers of disseminated breast cancer cells. Endocrine-Related Cancer. 2006;13(4):1033-67.
152. Meng S, Tripathy D, Frenkel EP, Shete S, Naftalis EZ, Huth JF, Beitsch PD, Leitch M, Hoover S, Euhus D. Circulating tumor cells in patients with breast cancer dormancy. Clinical Cancer Research. 2004;10(24):8152-62.
153. Ranganathan AC, Zhang L, Adam AP, Aguirre-Ghiso JA. Functional coupling of p38-induced up-regulation of BiP and activation of RNA-dependent protein kinase–like endoplasmic reticulum kinase to drug resistance of dormant carcinoma cells. Cancer Research. 2006;66(3):1702-11.
154. Cuenda A, Rousseau S. p38 MAP-kinases pathway regulation, function and role in human diseases. Biochimica et Biophysica Acta Molecular Cell Research. 2007;1773(8):1358-75.
155. Mellor HR, Ferguson DJP, Callaghan R. A model of quiescent tumour microregions for evaluating multicellular resistance to chemotherapeutic drugs. British Journal of Cancer. 2005;93(3):302-9.
156. Naumov GN, Townson JL, MacDonald IC, Wilson SM, Bramwell VH, Groom AC, Chambers AF. Ineffectiveness of doxorubicin treatment on solitary dormant mammary carcinoma cells or late-developing metastases. Breast Cancer Research and Treatment. 2003;82(3):199-206.
157. Muller PA, Vousden KH. p53 mutations in cancer. Nature Cell Biology. 2013;15(1):2-8.
158. Wilcken R, Wang G, Boeckler FM, Fersht AR. Kinetic mechanism of p53 oncogenic mutant aggregation and its inhibition. Proceedings of the National Academy of Sciences. 2012;109(34):13584-9.
159. Wheatcraft DRA, Liu X, Hummon AB. Sample preparation strategies for mass spectrometry imaging of 3D cell culture models. Journal of Visualized Experiments. 2014e52313(94):e52313.

160. Dubessy C, Merlin J-L, Marchal C, Guillemin F. Spheroids in radiobiology and photodynamic therapy. Critical Reviews in Oncology/Hematology. 2000;36(2):179-92.
161. Friedrich J, Eder W, Castaneda J, Doss M, Huber E, Ebner R, Kunz-Schughart LA. A reliable tool to determine cell viability in complex 3-D culture: the acid phosphatase assay. Journal of Biomolecular Screening. 2007;12(7):925-37.
162. Kunz-Schughart L, Freyer J. Adaptation of an automated selective dissociation procedure to two novel spheroid types. *In Vitro* Cellular & Developmental Biology-Animal. 1997;33(2):73-6.
163. Sutherland RM, Eddy HA, Bareham B, Reich K, Vanantwerp D. Resistance to adriamycin in multicellular spheroids. International Journal of Radiation Oncology, Biology, Physics. 1979;5(8):1225-30.
164. Ivanov DP, Grabowska AM, Garnett MC. High-Throughput spheroid screens using volume, resazurin reduction, and acid phosphatase activity. Cell Viability Assays: Methods and Protocols. 2017:43-59.
165. Chen W, Wong C, Vosburgh E, Levine AJ, Foran DJ, Xu EY. High-throughput image analysis of tumor spheroids: a user-friendly software application to measure the size of spheroids automatically and accurately. Journal of Visualized Experiments. 2014e51639(89):e51639.
166. Deckers T, Lambrechts T, Viazzi S, Hall GN, Papantoniou I, Bloemen V, Aerts J-M. High-throughput image-based monitoring of cell aggregation and microspheroid formation. PloS One. 2018;13(6):e0199092.
167. Hoque MT, Windus LC, Lovitt CJ, Avery VM. PCaAnalyser: A 2D-image analysis based module for effective determination of prostate cancer progression in 3D culture. PloS One. 2013;8(11):e79865.
168. Hou Y, Konen J, Brat DJ, Marcus AI, Cooper LA. TASI: A software tool for spatial-temporal quantification of tumor spheroid dynamics. Scientific Reports. 2018;8(1):7248.
169. Schindelin J, Arganda-Carreras I, Frise E, Kaynig V, Longair M, Pietzsch T, Preibisch S, Rueden C, Saalfeld S, Schmid B. Fiji: an open-source platform for biological-image analysis. Nature Methods. 2012;9(7):676-82.
170. Silva FS, Starostina IG, Ivanova VV, Rizvanov AA, Oliveira PJ, Pereira SP. Determination of metabolic viability and cell mass using a tandem resazurin/sulforhodamine B assay. Current Protocols in Toxicology. 2016;68(1):2.24. 1-2.. 15.

171. Chan GKY, Kleinheinz TL, Peterson D, Moffat JG. A simple high-content cell cycle assay reveals frequent discrepancies between cell number and ATP and MTS proliferation assays. PloS One. 2013;8(5):e63583.
172. Yang T-T, Sinai P, Kain SR. An acid phosphatase assay for quantifying the growth of adherent and nonadherent cells. Analytical Biochemistry. 1996;241(1):103-8.
173. Varghese AJ, Gulyas S, Mohindra JK. Hypoxia-dependent reduction of 1-(2-nitro-1-imidazolyl)-3-methoxy-2-propanol by Chinese hamster ovary cells and KHT tumor cells in vitro and in vivo. Cancer Research. 1976;36(10):3761-5.
174. Jamieson L, Harrison DJ, Campbell C. Chemical analysis of multicellular tumour spheroids. Analyst. 2015;140(12):3910-20.
175. Nichols AJ, Roussakis E, Klein OJ, Evans CL. Click-Assembled, Oxygen-Sensing Nanoconjugates for Depth-Resolved, Near-Infrared Imaging in a 3 D Cancer Model. Angewandte Chemie. 2014;126(14):3745-8.
176. Dmitriev RI, Kondrashina AV, Koren K, Klimant I, Zhdanov AV, Pakan JM, McDermott KW, Papkovsky DB. Small molecule phosphorescent probes for O 2 imaging in 3D tissue models. Biomaterials Science. 2014;2(6):853-66.
177. Zhang S, Hosaka M, Yoshihara T, Negishi K, Iida Y, Tobita S, Takeuchi T. Phosphorescent light–emitting iridium complexes serve as a hypoxia-sensing probe for tumor imaging in living animals. Cancer Research. 2010;70(11):4490-8.
178. Ivanov DP, Grabowska AM. Spheroid arrays for high-throughput single-cell analysis of spatial patterns and biomarker expression in 3D. Scientific Reports. 2017;7:41160.
179. Jaros J, Petrov M, Tesarova M, Hampl A. Revealing 3D Ultrastructure and Morphology of Stem Cell Spheroids by Electron Microscopy. 3D Cell Culture: Springer; 2017. p. 417-31.
180. Nederman T, Norling B, Glimelius B, Carlsson J, Brunk U. Demonstration of an extracellular matrix in multicellular tumor spheroids. Cancer Research. 1984;44(7):3090-7.
181. Le Roux L, Volgin A, Maxwell D, Ishihara K, Gelovani J, Schellingerhout D. Optimizing imaging of three-dimensional multicellular tumor spheroids with fluorescent reporter proteins using confocal microscopy. Molecular Imaging. 2008;7(5):214-21.
182. Richardson DS, Lichtman JW. Clarifying tissue clearing. Cell. 2015;162(2):246-57.

183. Kuwajima T, Sitko AA, Bhansali P, Jurgens C, Guido W, Mason C. ClearT: a detergent-and solvent-free clearing method for neuronal and non-neuronal tissue. Development. 2013;140(6):1364-8.
184. Boutin ME, Hoffman-Kim D. Application and assessment of optical clearing methods for imaging of tissue-engineered neural stem cell spheres. Tissue Engineering Part C: Methods. 2014;21(3):292-302.
185. Costa EC, Moreira AF, de Melo-Diogo D, Correia IJ. Polyethylene glycol molecular weight influences the Clear T2 optical clearing method for spheroids imaging by confocal laser scanning microscopy. Journal of Biomedical Optics. 2018;23(5):1-11.
186. Liu X, Hummon AB. Mass spectrometry imaging of therapeutics from animal models to three-dimensional cell cultures. Analytical Chemistry. 2015;87(19):9508-19.
187. Weaver EM, Hummon AB, Keithley RB. Chemometric analysis of MALDI mass spectrometric images of three-dimensional cell culture systems. Analytical Methods. 2015;7(17):7208-19.
188. Nilsson A, Goodwin RJ, Shariatgorji M, Vallianatou T, Webborn PJ, Andrén PE. Mass spectrometry imaging in drug development. Analytical Chemistry. 2015;87(3):1437-55.
189. Rodrigo MAM, Zitka O, Krizkova S, Moulick A, Adam V, Kizek R. MALDI-TOF MS as evolving cancer diagnostic tool: a review. Journal of Pharmaceutical and Biomedical Analysis. 2014;95:245-55.
190. Liu X, Weaver EM, Hummon AB. Evaluation of therapeutics in three-dimensional cell culture systems by MALDI imaging mass spectrometry. Analytical Chemistry. 2013;85(13):6295-302.
191. Li H, Hummon AB. Imaging mass spectrometry of three-dimensional cell culture systems. Analytical Chemistry. 2011;83(22):8794-801.
192. Tao Z, Shi A, Lu C, Song T, Zhang Z, Zhao J. Breast cancer: epidemiology and etiology. Cell Biochemistry and Biophysics. 2015;72(2):333-8.
193. Timmins NE, Nielsen LK. Generation of multicellular tumor spheroids by the hanging-drop method. Tissue Engineering. 2007:141-51.
194. Tung Y-C, Hsiao AY, Allen SG, Torisawa Y-s, Ho M, Takayama S. High-throughput 3D spheroid culture and drug testing using a 384 hanging drop array. Analyst. 2011;136(3):473-8.

195. Ivascu A, Kubbies M. Rapid generation of single-tumor spheroids for high-throughput cell function and toxicity analysis. Journal of Biomolecular Screening. 2006;11(8):922-32.
196. Zernike F. How I discovered phase contrast. Science. 1955;121(3141):345-9.
197. Chan TF, Vese LA. Active contours without edges. Institute of Electrical and Electronics Engineers Transactions on Image Processing. 2001;10(2):266-77.
198. Ayers GD, McKinley ET, Zhao P, Fritz JM, Metry RE, Deal BC, Adlerz KM, Coffey RJ, Manning HC. Volume of preclinical xenograft tumors is more accurately assessed by ultrasound imaging than manual caliper measurements. Journal of Ultrasound in Medicine. 2010;29(6):891-901.
199. Smith PK, Krohn RI, Hermanson G, Mallia A, Gartner F, Provenzano M, Fujimoto E, Goeke N, Olson B, Klenk D. Measurement of protein using bicinchoninic acid. Analytical Biochemistry. 1985;150(1):76-85.
200. Jones KH, Senft JA. An improved method to determine cell viability by simultaneous staining with fluorescein diacetate-propidium iodide. Journal of Histochemistry & Cytochemistry. 1985;33(1):77-9.
201. Fischer AH, Jacobson KA, Rose J, Zeller R. Hematoxylin and eosin staining of tissue and cell sections. Cold Spring Harbor Protocols. 2008;2008(5):pdb. prot4986.
202. Vichai V, Kirtikara K. Sulforhodamine B colorimetric assay for cytotoxicity screening. Nature Protocols. 2006;1(3):1112-6.
203. Keepers YP, Pizao PE, Peters GJ, van Ark-Otte J, Winograd B, Pinedo HM. Comparison of the sulforhodamine B protein and tetrazolium (MTT) assays for *in vitro* chemosensitivity testing. European Journal of Cancer and Clinical Oncology. 1991;27(7):897-900.
204. Sobecki M, Mrouj K, Colinge J, Gerbe F, Jay P, Krasinska L, Dulic V, Fisher D. Cell-cycle regulation accounts for variability in Ki-67 expression levels. Cancer Research. 2017;77(10):2722-34.
205. Lin R-Z, Chou L-F, Chien C-CM, Chang H-Y. Dynamic analysis of hepatoma spheroid formation: roles of E-cadherin and β1-integrin. Cell and Tissue Research. 2006;324(3):411-22.
206. Kapuscinski J. DAPI: a DNA-specific fluorescent probe. Biotechnic & Histochemistry. 1995;70(5):220-33.

207. Motulsky HJ, Brown RE. Detecting outliers when fitting data with nonlinear regression–a new method based on robust nonlinear regression and the false discovery rate. BioMed Central Bioinformatics. 2006;7(1):123.
208. Hurrell T, Ellero AA, Masso ZF, Cromarty AD. Characterization and reproducibility of HepG2 hanging drop spheroids toxicology *in vitro*. Toxicology *in Vitro*. 2018;50:86-94.
209. Raghavan S, Mehta P, Horst EN, Ward MR, Rowley KR, Mehta G. Comparative analysis of tumor spheroid generation techniques for differential in vitro drug toxicity. Oncotarget. 2016;7(13):16948-61.
210. Ryan J, Sharf B, Cristofalo V. The influence of culture medium volume on cell density and lifespan of human diploid fibroblasts. Experimental Cell Research. 1975;91(2):389-92.
211. Gaskell H, Sharma P, Colley HE, Murdoch C, Williams DP, Webb SD. Characterization of a functional C3A liver spheroid model. Toxicology Research. 2016;5(4):1053-65.
212. Hirschhaeuser F, Menne H, Dittfeld C, West J, Mueller-Klieser W, Kunz-Schughart LA. Multicellular tumor spheroids: an underestimated tool is catching up again. Journal of Biotechnology. 2010;148(1):3-15.
213. Kenny PA, Lee GY, Myers CA, Neve RM, Semeiks JR, Spellman PT, Lorenz K, Lee EH, Barcellos-Hoff MH, Petersen OW. The morphologies of breast cancer cell lines in three-dimensional assays correlate with their profiles of gene expression. Molecular Oncology. 2007;1(1):84-96.
214. Imamura Y, Mukohara T, Shimono Y, Funakoshi Y, Chayahara N, Toyoda M, Kiyota N, Takao S, Kono S, Nakatsura T. Comparison of 2D-and 3D-culture models as drug-testing platforms in breast cancer. Oncology Reports. 2015;33(4):1837-43.
215. Stadler M, Scherzer M, Walter S, Holzner S, Pudelko K, Riedl A, Unger C, Kramer N, Weil B, Neesen J. Exclusion from spheroid formation identifies loss of essential cell-cell adhesion molecules in colon cancer cells. Scientific Reports. 2018;8(1):1151.
216. Enmon Jr RM, O'Connor KC, Lacks DJ, Schwartz DK, Dotson RS. Dynamics of spheroid self-assembly in liquid-overlay culture of DU 145 human prostate cancer cells. Biotechnology and Bioengineering. 2001;72(6):579-91.
217. Kyffin JA, Sharma P, Leedale J, Colley HE, Murdoch C, Harding AL, Mistry P, Webb SD. Characterisation of a functional rat hepatocyte spheroid model. Toxicology in Vitro. 2019;55:160-72.

218. Cui X, Hartanto Y, Zhang H. Advances in multicellular spheroids formation. Journal of The Royal Society Interface. 2017;14(127):20160877.
219. Casciari J, Sotirchos S, Sutherland R. Mathematical modelling of microenvironment and growth in EMT6/Ro multicellular tumour spheroids. Cell Proliferation. 1992;25(1):1-22.
220. Sant S, Johnston PA. The production of 3D tumor spheroids for cancer drug discovery. Drug Discovery Today: Technologies. 2017;23:27-36.
221. Li Y-J, Wei Z-M, Meng Y-X, Ji X-R. β-catenin up-regulates the expression of cyclinD1, c-myc and MMP-7 in human pancreatic cancer: Relationships with carcinogenesis and metastasis. World Journal of Gastroenterology. 2005;11(14):2117-23.
222. Reddel RR, Murphy LC, Hall RE, Sutherland RL. Differential sensitivity of human breast cancer cell lines to the growth-inhibitory effects of tamoxifen. Cancer Research. 1985;45(4):1525-31.
223. Wrzesinski K, Fey S. Metabolic reprogramming and the recovery of physiological functionality in 3D cultures in micro-bioreactors. Bioengineering. 2018;5(1):22.
224. Laurent J, Frongia C, Cazales M, Mondesert O, Ducommun B, Lobjois V. Multicellular tumor spheroid models to explore cell cycle checkpoints in 3D. BioMed Central Cancer. 2013;13(1):73.
225. Rotman B, Papermaster BW. Membrane properties of living mammalian cells as studied by enzymatic hydrolysis of fluorogenic esters. Proceedings of the National Academy of Sciences. 1966;55(1):134-41.
226. Zhang Y, Chen X, Gueydan C, Han J. Plasma membrane changes during programmed cell deaths. Cell Research. 2018;28(1):9-21.
227. Boyd V, Cholewa OM, Papas KK. Limitations in the use of fluorescein diacetate/propidium iodide (FDA/PI) and cell permeable nucleic acid stains for viability measurements of isolated islets of Langerhans. Current Trends in Biotechnology and Pharmacy. 2008;2(2):66-84.
228. Accart N, Sergi F, Rooke R. Revisiting fixation and embedding techniques for optimal detection of dendritic cell subsets in tissues. Journal of Histochemistry & Cytochemistry. 2014;62(9):661-71.
229. Olsen TR, Mattix B, Casco M, Herbst A, Williams C, Tarasidis A, Evans G, Jenkins L, McMahan CL, Simionescu D. Processing cellular spheroids for histological examination. Journal of Histotechnology. 2014;37(4):138-42.

230. Ferguson R, Subramanian V. Embryoid body arrays: Parallel cryosectioning of spheroid/embryoid body samples for medium through-put analysis. Stem Cell Research. 2018;28:125-30.
231. Groebe K, Mueller-Klieser W. On the relation between size of necrosis and diameter of tumor spheroids. International Journal of Radiation Oncology, Biology, Physics. 1996;34(2):395-401.
232. Bertuzzi A, Fasano A, Gandolfi A, Sinisgalli C. Necrotic core in EMT6/Ro tumour spheroids: Is it caused by an ATP deficit? Journal of Theoretical Biology. 2010;262(1):142-50.
233. Hlatky L, Sachs RK, Alpen EL. Joint oxygen-glucose deprivation as the cause of necrosis in a tumor analog. Journal of Cellular Physiology. 1988;134(2):167-78.
234. Freyer JP, Schor PL, Saponara AG. Partial purification of a protein growth inhibitor from multicellular spheroids. Biochemical and Biophysical Research Communications. 1988;152(1):463-8.
235. Karsch-Bluman A, Feiglin A, Arbib E, Stern T, Shoval H, Schwob O, Berger M, Benny O. Tissue necrosis and its role in cancer progression. Oncogene. 2018;38(11):1920-35.
236. Proskuryakov SY, Gabai VL. Mechanisms of tumor cell necrosis. Current Pharmaceutical Design. 2010;16(1):56-68.
237. Riffle S, Pandey RN, Albert M, Hegde RS. Linking hypoxia, DNA damage and proliferation in multicellular tumor spheroids. BioMed Central Cancer. 2017;17(1):338.
238. Rao SS, Kondapaneni RV, Narkhede AA. Bioengineered models to study tumor dormancy. Journal of Biological Engineering. 2019;13(1):3.
239. Hammond E, Asselin M-C, Forster D, O'Connor JP, Senra J, Williams K. The meaning, measurement and modification of hypoxia in the laboratory and the clinic. Clinical Oncology. 2014;26(5):277-88.
240. Riffle S, Hegde RS. Modeling tumor cell adaptations to hypoxia in multicellular tumor spheroids. Journal of Experimental & Clinical Cancer Research. 2017;36(1):102.
241. Bloch K, Smith H, van Hamel Parsons V, Gavaghan D, Kelly C, Fletcher A, Maini P, Callaghan R. Metabolic alterations during the growth of tumour spheroids. Cell Biochemistry and Biophysics. 2014;68(3):615-28.
242. Däster S, Amatruda N, Calabrese D, Ivanek R, Turrini E, Droeser RA, Zajac P, Fimognari C, Spagnoli GC, Iezzi G. Induction of hypoxia and necrosis in multicellular

tumor spheroids is associated with resistance to chemotherapy treatment. Oncotarget. 2017;8(1):1725-36.
243. Van Tonder A, Joubert AM, Cromarty AD. Limitations of the 3-(4, 5-dimethylthiazol-2-yl)-2, 5-diphenyl-2H-tetrazolium bromide (MTT) assay when compared to three commonly used cell enumeration assays. BioMed Central Research Notes. 2015;8(1):47.
244. Campiglio M, Somenzi G, Olgiati C, Beretta G, Balsari A, Zaffaroni N, Valagussa P, Ménard S. Role of proliferation in HER2 status predicted response to doxorubicin. International Journal of Cancer. 2003;105(4):568-73.
245. Yang F, Teves SS, Kemp CJ, Henikoff S. Doxorubicin, DNA torsion, and chromatin dynamics. Biochimica et Biophysica Acta Reviews on Cancer. 2014;1845(1):84-9.
246. Gewirtz D. A critical evaluation of the mechanisms of action proposed for the antitumor effects of the anthracycline antibiotics adriamycin and daunorubicin. Biochemical Pharmacology. 1999;57(7):727-41.
247. Doroshow JH, Synold TW, Somlo G, Akman SA, Gajewski E. Oxidative DNA base modifications in peripheral blood mononuclear cells of patients treated with high-dose infusional doxorubicin. Blood. 2001;97(9):2839-45.
248. Coldwell KE, Cutts SM, Ognibene TJ, Henderson PT, Phillips DR. Detection of Adriamycin–DNA adducts by accelerator mass spectrometry at clinically relevant Adriamycin concentrations. Nucleic Acids Research. 2008;36(16):e100.
249. Ling Y-H, El-Naggar AK, Priebe W, Perez-Soler R. Cell cycle-dependent cytotoxicity, G2/M phase arrest, and disruption of p34cdc2/cyclin B1 activity induced by doxorubicin in synchronized P388 cells. Molecular Pharmacology. 1996;49(5):832-41.
250. Freres P, Jerusalem G, Moonen M. Chapter 2 - Categories of Anticancer Treatments. In: Lancellotti P, Zamorano Gómez JL, Galderisi M, editors. Anti-Cancer Treatments and Cardiotoxicity. Boston: Academic Press; 2017. p. 7-11.
251. Das S, Tripathi N, Siddharth S, Nayak A, Nayak D, Sethy C, Bharatam PV, Kundu CN. Etoposide and doxorubicin enhance the sensitivity of triple negative breast cancers through modulation of TRAIL-DR5 axis. Apoptosis. 2017;22(10):1205-24.
252. Berlin V, Haseltine W. Reduction of adriamycin to a semiquinone-free radical by NADPH cytochrome P-450 reductase produces DNA cleavage in a reaction mediated by molecular oxygen. Journal of Biological Chemistry. 1981;256(10):4747-56.

253. Lovitt CJ, Shelper TB, Avery VM. Doxorubicin resistance in breast cancer cells is mediated by extracellular matrix proteins. BioMed Central Cancer. 2018;18(1):41.
254. Alves AC, Magarkar A, Horta M, Lima JL, Bunker A, Nunes C, Reis S. Influence of doxorubicin on model cell membrane properties: insights from in vitro and in silico studies. Scientific Reports. 2017;7(1):6343.
255. Yay A, Ozdamar S, Balcioglu E, Baran M, Akkus D, Sonmez M. The effects of adriamycin on E-cadherin mediated cell-cell adhesion and apoptosis during early kidney development. Biotechnic & Histochemistry. 2015;90(5):375-83.
256. Fey SJ, Wrzesinski K. Determination of drug toxicity using 3D spheroids constructed from an immortal human hepatocyte cell line. Toxicological Sciences. 2012;127(2):403-11.
257. Chougule MB, Patel AR, Jackson T, Singh M. Antitumor activity of Noscapine in combination with Doxorubicin in triple negative breast cancer. PloS One. 2011;6(3):e17733.
258. Reagan-Shaw S, Nihal M, Ahmad N. Dose translation from animal to human studies revisited. The FASEB Journal. 2008;22(3):659-61.
259. Kohno N, Ohnuma T, Truog P. Effects of hyaluronidase on doxorubicin penetration into squamous carcinoma multicellular tumor spheroids and its cell lethality. Journal of Cancer Research and Clinical Oncology. 1994;120(5):293-7.
260. Doublier S, Belisario DC, Polimeni M, Annaratone L, Riganti C, Allia E, Ghigo D, Bosia A, Sapino A. HIF-1 activation induces doxorubicin resistance in MCF7 3-D spheroids via P-glycoprotein expression: a potential model of the chemo-resistance of invasive micropapillary carcinoma of the breast. BioMed Central Cancer. 2012;12(1):4.
261. Chandrasekaran S, Marshall JR, Messing JA, Hsu J-W, King MR. TRAIL-mediated apoptosis in breast cancer cells cultured as 3D spheroids. PloS One. 2014;9(10):e111487.
262. Li Y, Liang Y, Sang Y, Song X, Zhang H, Liu Y, Jiang L, Yang Q. MiR-770 suppresses the chemo-resistance and metastasis of triple negative breast cancer via direct targeting of STMN1. Cell death & Disease. 2018;9(1):14.
263. Yuan T, Gao D, Li S, Jiang Y. Co-culture of tumor spheroids and monocytes in a collagen matrix-embedded microfluidic device to study the migration of breast cancer cells. Chinese Chemical Letters. 2019;30(2):331-6.

264. Wrzesinski K, Fey SJ. Metabolic Reprogramming and the Recovery of Physiological Functionality in 3D Cultures in Micro-Bioreactors. Bioengineering. 2018;5(1):E22.
265. Theiner S, Van Malderen SJ, Van Acker T, Legin A, Keppler BK, Vanhaecke F, Koellensperger G. Fast high-resolution laser ablation-inductively coupled plasma mass spectrometry imaging of the distribution of platinum-based anticancer compounds in multicellular tumor spheroids. Analytical Chemistry. 2017;89(23):12641-5.

Appendix I: Ethical approval for the study

The Research Ethics Committee, Faculty Health Sciences, University of Pretoria complies with ICH-GCP guidelines and has US Federal wide Assurance.
- FWA 00002567, Approved dd 22 May 2002 and Expires 03/20/2022.
- IRB 0000 2235 IORG0001762 Approved dd 22/04/2014 and Expires 03/14/2020.

UNIVERSITEIT VAN PRETORIA
UNIVERSITY OF PRETORIA
YUNIBESITHI YA PRETORIA

Faculty of Health Sciences Research Ethics Committee

31/08/2017

Approval Certificate
New Application

Ethics Reference No: 338/2017

Title: Spatial characterization of the BT-20 triple negative breast cancer spheroidal model

Dear Keith Ncube

The **New Application** as supported by documents specified in your cover letter dated 28/07/2017 for your research received on the 28/07/2017, was approved by the Faculty of Health Sciences Research Ethics Committee on its quorate meeting of 30/08/2017.

Please note the following about your ethics approval:
- Ethics Approval is valid for 2 years
- Please remember to use your protocol number (**338/2017**) on any documents or correspondence with the Research Ethics Committee regarding your research.
- Please note that the Research Ethics Committee may ask further questions, seek additional information, require further modification, or monitor the conduct of your research.

Ethics approval is subject to the following:
- The ethics approval is conditional on the receipt of **6 monthly written Progress Reports**, and
- The ethics approval is conditional on the research being conducted as stipulated by the details of all documents submitted to the Committee. In the event that a further need arises to change who the investigators are, the methods or any other aspect, such changes must be submitted as an Amendment for approval by the Committee.

We wish you the best with your research.

Yours sincerely

*** Kindly collect your original signed approval certificate from our offices, Faculty of Health Sciences, Research Ethics Committee, Tswelopele Building, Level 4-60*

Dr R Sommers; MBChB; MMed (Int); MPharMed,PhD
Deputy Chairperson of the Faculty of Health Sciences Research Ethics Committee, University of Pretoria

The Faculty of Health Sciences Research Ethics Committee complies with the SA National Act 61 of 2003 as it pertains to health research and the United States Code of Federal Regulations Title 45 and 46. This committee abides by the ethical norms and principles for research, established by the Declaration of Helsinki, the South African Medical Research Council Guidelines as well as the Guidelines for Ethical Research: Principles Structures and Processes, Second Edition 2015 (Department of Health).

☎ 012 356 3084 fhsethics@up.ac.za http://www.up.ac.za/healthethics
✉ Private Bag X323, Arcadia, 0007 - Tswelopele Building, Level 4, Room 60, Gezina, Pretoria

Appendix II: Reagent preparation

Acetic acid

A 1% (v/v) solution of acetic acid was prepared by diluting 1 mL of glacial acetic acid (Merck Chemicals, South Africa) with distilled water to a final volume of 100 mL. The solution was stored at room temperature.

Anti-Ki-67 antibody

The anti-Ki67 antibody [KI67] (Alexa Fluor® 488) ab206633 (Abcam, Cambridge, UK) was stored in 10 µL aliquots and stored at 4°C in the dark until use. The antibody was then diluted to a working dilution of 1 µg/mL in B-PBT.

Anti-pan cadherin antibody

The anti-pan Cadherin antibody (ab6529) was purchased from Abcam (Cambridge, UK), and stored as 10 µL aliquots at -80°C until use. The antibody was diluted in B-PBT in a ratio of 1:1000.

APH assay buffer

The APH assay buffer was prepared by dissolving para-nitrophenylphosphate (100 mg), and Triton X-100 (50 µL) in citrate buffer to make a total volume of 50 mL. The prepared buffer was adjusted to a pH of 4.8 and stored at 4°C.

Agarose

Agarose powder (2 g) was purchased from Sigma Aldrich (St Louis, USA) and dissolved in 200 mL of DMEM: F12 (1:1), and heated in a microwave, until all agarose went into solution. After the heated solution solidified, it was autoclaved for 30 min at 120°C, 2 bar. The autoclaved agarose was transferred to sterile 100 mL bottles and stored at 4°C.

BCA assay reagent A

The BCA disodium hydrate salt (1 g) and 0.95 g of sodium bicarbonate were purchased from Sigma Aldrich (St Louis, USA), and dissolved with sodium carbonate (2 g), sodium hydroxide (0.4 g) and 0.16 g of sodium tartrate (all salts from Merck & Co. New Jersey, USA) to a final volume 100 mL in distilled water. The pH of this solution was adjusted to 11.25 and stored at 4°C.

BCA assay reagent B

Reagent B of the BCA assay was prepared by dissolving 0.4 g of copper II sulphate pentahydrate (Sigma Aldrich, St Louis, USA) to a final volume of 10 mL in distilled water, the solution was covered with foil for protection from light and stored at 4°C.

B-PBT

The B-PBT buffer was prepared by dissolving 1 mL Triton X-100, 10 mL normal goat serum, and 4 g BSA (all from Sigma Aldrich, St Louis, USA) in PBS, to make a final volume of 100 mL, which was stored at 4°C.

Citrate buffer

The sodium citrate dehydrate salt (Sigma Aldrich, St Louis, USA), and the citrate buffer was prepared by dissolving 7.35 g of the salt into 250 mL distilled water (18 Ω). The prepared solution was stored at room temperature.

DAPI

A 10 mg/mL stock solution of DAPI (Thermo Fischer Scientific, Massachusetts, United States) was prepared by adding 1 mL of distilled water to 100 mg of the powder and the solution was stored at 20°C. An intermediate solution (100 µg/mL) was prepared by dissolving 10 µL of the DAPI stock solution in 990 µL of PBS. The working solution was prepared by adding 10 µL of the intermediate solution to 990 µL of PBT and used immediately.

Doxorubicin hydrochloride

Doxorubicin hydrochloride (10 mg) was purchased from Sigma Aldrich (St Louis, USA) and diluted in 736 µL of DMSO, to make up a 25 mM stock solution, which was stored as 5 µL aliquots at -80°C. The stock solution was dissolved in culture medium to the desired concentration for respective experiments prior to use.

Eosin

The eosin stain was prepared by dissolving 2 g of yellow eosin powder in distilled water to a final volume of 200 mL and stored at room temperature.

Formaldehyde

To prepare 4% (w/v) formaldehyde, 40 g of the paraformaldehyde powder (Sigma Aldrich, St Louis, USA) was dissolved in PBS to a final volume of 1 L. The pH was adjusted 7.0 using sodium hydroxide.

Gelatin

Gelatin powder (52.5 g) was obtained from Sigma Aldrich (St Louis, USA) and dissolved in high purity water (300 mL, 18Ω) through vigorous mixing, until all the powder went into solution. The solution was stored at 4°C.

Gentian violet

A 2% gentian violet solution was obtained from the local pharmacy and diluted to 0.5% by adding 250 µL of gentian violet to 750 µL of PBS. The solution was stored at room temperature.

Fluorescein diacetate

Fluorescein diacetate powder was diluted to a stock concentration of 5 mg/mL in acetone and protected from light by covering with aluminium foil. The prepared solution was stored at -20°C.

Haematoxylin

The haematoxylin stain was prepared by dissolving aluminium potassium sulphate (50 g), citric acid (1 g), chloral hydrate (50 g), haematoxylin (1 g), sodium iodate (0.2 g) in distilled water, to make a final volume of 1L, and the solution was stored at room temperature. All powders were purchased from Sigma Aldrich (St Louis, USA).

Image-iT® hypoxia probe

The Image-iT™ red hypoxia reagent lyophilised powder (1 mg) was dissolved in 1.4 mL of DMSO, to make a 1 mM stock solution, which was stored at -20°C.

PBS

The PBS buffer was made by dissolving 9.23 g of the FTA haemagglutinin powder (BD Bioscience, New Jersey, USA) in distilled water, to make a final volume of 1L. The buffer was then sterilised by autoclaving for 30 min at 120°C, and 2 bar. The buffer was then stored at 4°C.

PBT

The PBT solution was made by diluting 200 µL of Triton X-100 in PBS to make a final volume of 100 mL. This solution was stored at 4°C.

Propidium iodide

Propidium iodide powder (Sigma Aldrich, St Louis, USA) was diluted to a stock concentration of 2 mg/mL in PBS, protected from light with foil, and stored at 4°C until use. The prepared solution was used within six months.

RIPA buffer

The radioimmunoprecipitation assay (RIPA) buffer was prepared by dissolving cOmplete® protease inhibitor cocktail (20 mg), sodium hydroxide (877 mg), sodium deoxycholate (500 mg), sodium dodecyl sulphate (100 mg), triton X-100 (1 mL), and tris-OH (606 mg) in a final volume of 100 mL distilled water. The buffer was stored in 100 µL aliquots at -80°C.

SRB dye

The SRB dye was prepared by dissolving 57 mg of the SRB powder (Sigma Aldrich, St louis, USA) in 100 mL of 1% (v/v) acetic acid in distilled water and stored at 4°C.

Trypan blue

Trypan blue (100 mg) from Sigma Aldrich was dissolved in 10 mL PBS (stock solution). A 1 in 10 dilution of the stock solution was done to prepare a working dilution of trypan blue and stored in the dark at room temperature.

Sodium hydroxide

Sodium hydroxide pellets was obtained from Sigma Aldrich, and 200 mg was dissolved in 5 mL distilled water (18 Ω). The prepared 1 M solution was stored in room temperature.

Saponin

Saponin powder was obtained from Sigma Aldrich (St Louis, USA) and stored at room temperature. To make-up the 1% w/v positive control solution, 2 mg of the saponin powder was dissolved in 2 mL culture medium, vortexed to allow for optimum dissolution, and filter sterilised with a 0.2 µm filter.

TCA

A 50% (w/v) solution of TCA was prepared by dissolving 50 g of TCA crystals (Sigma Aldrich, St Louis, USA) in distilled water, to make a final solution of 100 mL, which was stored at 4°C.

Tris-buffer

A 10 mM solution of the tris buffer was made by dissolving 121.1 mg of tris(hydroxymethyl) aminomethane (Tris) in 100 mL distilled water. The pH of the solution was adjusted to 10.5 using sodium hydroxide, and the buffer was stored at 4°C.